受入
87-8-412
高工研図書室

CERN-TH.4773/87
CPT-87/PE2018
PM/87-34

SUPERSYMMETRY AND COMPOSITENESS AT LINEAR COLLIDERS

P. Chiappetta
CERN - Geneva

P. Méry*)
Centre de Physique Théorique+), CNRS, Marseille

M. Perrottet
Centre de Physique Théorique+), CNRS, Marseille
and
CERN - Geneva

and

F.M. Renard
Laboratoire de Physique Mathématique")
USTL, 34060 Montpellier Cedex

A B S T R A C T

We discuss the search for supersymmetric partners of leptons, quarks and gauge bosons as well as for compositeness effects in the leptonic and bosonic sectors of the reactions $e^+e^- \to W^+W^-$, ZZ, γZ, $\gamma\gamma$ at future e^+e^- linear colliders in the TeV range. Electron beam longitudinal polarization effects are included. Limits of observability on masses of supersymmetric partners and on compositeness scales are given.

---

*) Also at Faculté des Sciences, Luminy, Marseille.
+) Laboratoire propre du CNRS.
") Unité associée au CNRS N° 040768.

CERN-TH.4773/87
CPT-87/PE2018
PM/87-34
June 1987

1. - INTRODUCTION

The purpose of this report is to study the capabilities of future high energy e^+e^- linear colliders with respect to the search of two specific types of new phenomena beyond the standard model predictions, namely supersymmetry and compositeness.

Motivations for the existence of such phenomena will not be recalled as they have recently been restated in many places, see e.g. Refs. 1) and 2). We just want to mention that in many theorists' opinion, the occurrence of new physics in the TeV range is a must, so that either e^+e^- collisions in this range of energy as well as pp or ep collisions in the tens of TeV (in order to ensure a few TeV at the parton level) should be very fruitful. The relative merits of these three kinds of machines can be compared on the basis of the existing reviews and study group reports[3]. It seems to appear that these machines are in fact complementary with an advantage to e^+e^- colliders for electroweak phenomena[2].

Our contribution precisely concerns the production of pairs of supersymmetric particles (mainly non-strongly interacting ones) and the occurrence of compositeness effects in the two-boson channels $e^+e^- \to W^+W^-$, ZZ, γZ and $\gamma\gamma$.

We will discuss especially the following cases: E_{cm} = 0.6, 1 and 2 TeV but we will also give the energy dependence of the production cross-sections from 200 GeV to 2 TeV in order to make contact with the second phase of LEP and to appreciate the possibilities of such an e^+e^- collider for any choice of the centre-of-mass energy.

Bounds on supersymmetric particle masses and on compositeness scales will be established assuming a luminosity of 10^{33} cm^{-2} sec^{-1} in each case (and possibly 10^{34} cm^{-2} sec^{-1} for the cases of 1 or 2 TeV). For supersymmetric particle production consequently assuming an integrated luminosity of 10^{40} (10^{41}) cm^{-2} sec^{-1} for one physical year of running and requiring at least 10 events, limits the observable cross-section to 1 (0.1) fb. For the search of compositeness effects the criterion is different as all four e^+e^- annihilation processes studied here already get observable cross-sections (larger than the above numbers) from the standard contribution. In agreement with a procedure previously used in the case of LEP II[4] we will then require a 5% departure from the standard prediction to the integrated cross-sections due to compositeness effects. More refined bounds could certainly be established by looking at other

properties of the reactions like angular distributions, but taking into account detection efficiencies, background contaminations, etc. We will not discuss these effects here but in order to give a feeling on these possibilities we will show examples of angular distributions and of polarization effects. Spectacular polarization effects associated to new physics had been shown to appear in the SLC/LEP energy range[5] in either cases of transversally or longitudinally polarized $e^{\pm}$ beams. In this report we will stick to the case of a single (e^-) longitudinally polarized beam because this seems at the moment to be the most realistic possibility and we will show predictions for the left-right polarization asymmetry $A_{\parallel}$.

The first part of this study concerning supersymmetric particle production is developped in Section 2 with the treatment of e^+e^- annihilation into slepton, squark, wino and zino pairs as well as photino + Zino. The search for compositeness effects in $e^+e^- \to W^+W^-$, ZZ, γZ and $\gamma\gamma$ is done in Section 3 by considering the occurrence of excited state exchanges, anomalous couplings or residual interactions in either the leptonic or the bosonic sector. A final summary including a discussion of the perspectives offered by specific choices of energy and luminosity will be given in Section 4.

2. - SUPERSYMMETRIC PARTICLE PRODUCTION

2a - Sleptons and squarks

Amplitudes and cross-sections including polarization effects have been given in Ref. 6). The production process goes through γ and Z formation and in the case of $\tilde{e}^+\tilde{e}^-$ (and also $\tilde{\nu}_e\bar{\tilde{\nu}}_e$) also through $\tilde{\gamma}$ and $\tilde{Z}$ exchanges. Coupling constants are totally determined in terms of standard electroweak parameters, separately for L-type or R-type of sleptons and squarks. The only unknowns are then masses of produced (and exchanged) supersymmetric particles. In the following illustrations, we have chosen two kinds of models[7]:

i) the minimal supersymmetric model (hereafter denoted MSSM) which corresponds to N = 1 supersymmetry which predict the corresponding mass formulae

$$m^2(\tilde{d}_L) = m_0^2 + 0.43\, r\, m_{Z^0}^2 + 30.2\, m_{\tilde{\gamma}}^2$$
$$m^2(\tilde{d}_R) = m_0^2 + 0.07\, r\, m_{Z^0}^2 + 28.4\, m_{\tilde{\gamma}}^2$$
$$m^2(\tilde{u}_L) = m_0^2 - 0.36\, r\, m_{Z^0}^2 + 30.2\, m_{\tilde{\gamma}}^2$$
$$m^2(\tilde{u}_R) = m_0^2 - 0.14\, r\, m_{Z^0}^2 + 28.4\, m_{\tilde{\gamma}}^2$$

$$m^2(\tilde{\ell}_L) = m_0^2 + 0.28\, r\, m_{Z^0}^2 + 2.2\, m_{\tilde{\gamma}}^2$$
$$m^2(\tilde{\ell}_R) = m_0^2 + 0.22\, r\, m_{Z^0}^2 + 0.6\, m_{\tilde{\gamma}}^2$$

$$m^2(\tilde{\nu}) = m_0^2 - 0.50\, r\, m_{Z^0}^2 + 2.2\, m_{\tilde{\gamma}}^2$$

where

$$r = \frac{v^2 - \bar{v}^2}{v^2 + \bar{v}^2} \quad \text{with } v = \langle 0|H|0\rangle \text{ and } \bar{v} = \langle 0|\bar{H}|0\rangle,$$

and m_0 sets the scale of the mass spectrum and will be varied in the range allowed by the energy of the machine; the other parameters will be taken in order to illustrate typical situations like degenerate or non-degenerate L and R states;

ii) the minimal superstring inspired model (hereafter denoted MSIM) in which there is an $SU(3)_C \times SU(2)_L \times U(1)_Y \times U(1)$ gauge group and the only bare soft supersymmetric breaking mass parameter is a universal gaugino mass $m_{\frac{1}{2}}$

$$m^2(\tilde{d}_L) = m_0^2 + 3.8\, m_{1/2}^2 + \frac{1}{30} F m_W^2$$
$$m^2(\tilde{d}_R) = m_0^2 + 3.5\, m_{1/2}^2 - \frac{1}{60} F m_W^2$$
$$m^2(\tilde{u}_L) = m_0^2 + 3.8\, m_{1/2}^2 + \frac{1}{30} F m_W^2$$
$$m^2(\tilde{u}_R) = m_0^2 + 3.5\, m_{1/2}^2 + \frac{1}{30} F m_W^2$$

$$m^2(\tilde{\ell}_L) = m_0^2 + 0.5\, m_{1/2}^2 - \frac{1}{60} F m_W^2$$
$$m^2(\tilde{\ell}_R) = m_0^2 + 0.14\, m_{1/2}^2 + \frac{1}{30} F m_W^2$$
$$m^2(\tilde{\nu}) = m_0^2 + 0.5\, m_{1/2}^2 - \frac{1}{60} F m_W^2$$

where

$$F = \frac{10}{3} \cdot \frac{\tan^2\theta_W}{v^2 + \bar{v}^2} (5x^2 - 4v^2 - \bar{v}^2)$$

(x being the vacuum expectation value of the third Higgs). $m_{\frac{1}{2}}$ is related to $m_{\tilde{\gamma}}$ by

$$m_{1/2} = \frac{m_{\tilde{\gamma}}}{0.16} \quad .$$

Let us first consider the scalar muon pair production $e^+e^- \to \tilde{\mu}^+\tilde{\mu}^- \to \mu^+\mu^-\tilde{\gamma}\,\tilde{\gamma}$. In Fig. 1 we show the total cross-section versus m_0 for three characteristic mass spectra: MSIM with $m_{\tilde{\gamma}} = 10$ GeV leading to a small mass difference between $\tilde{\mu}_L$ and $\tilde{\mu}_R$, MSIM with $m_{\tilde{\gamma}} = 100$ GeV in which $\tilde{\mu}_L$ is much heavier than $\tilde{\mu}_R$ and finally MSSM with $m_{\tilde{\gamma}} = 100$ GeV. The prediction from MSSM with $m_{\tilde{\gamma}} = 10$ GeV has not been quoted here since it is very similar to the MSIM case with $m_{\tilde{\mu}} = 10$ GeV. With expected luminosities, one can reach the mass values allowed by phase space. For $\sqrt{s} = 2$ TeV, a luminosity of $\mathcal{L} = 10^{34}$ cm^{-2} sec^{-1} is needed to reach $m_0 \simeq 980$ GeV whereas a $\mathcal{L} = 10^{33}$ cm^{-2} sec^{-1} one reaches $m_0 = 900$ GeV. We give in Fig. 2 the total cross-section versus $\sqrt{s}$ between 200 GeV (LEP II energy) and 2 TeV (CLIC project) for three specific m_0 masses (60, 200, 600 GeV). The usefulness of a longitudinally polarized electron beam is shown in Fig. 3 for the left-right asymmetry $A_{\parallel}$. Since the asymmetries for $\tilde{\mu}_L$ and $\tilde{\mu}_R$ are large and of opposite sign we expect very small values for $A_{\parallel}$ when $\tilde{\mu}_L$ and $\tilde{\mu}_R$ are quite degenerate in mass: for MSIM with $m_{\tilde{\gamma}} \simeq 10$ GeV and MSSM with $m_{\tilde{\gamma}} = 0$, 10 GeV we get $A_{\parallel} \simeq -10\%$. This is no more the case when $m_{\tilde{\gamma}} = 100$ GeV since $\tilde{\mu}_R$ is lighter than $\tilde{\mu}_L$: $A_{\parallel}$ is large and positive near threshold and decreases with $\sqrt{s}$ since the channel for $\tilde{\mu}_L$ production is open. Angular distributions for typical choices of m_0 and $m_{\tilde{\gamma}}$ are plotted in Fig. 4 for $\sqrt{s} = 600$ GeV. There is no forward-backward asymmetry. For small $\tilde{\mu}$ masses, $d\sigma/d\cos\theta$ is maximal at $\theta = \pi/2$ which is a reminiscence of the $\sin^2\theta$ behaviour for $\tilde{\mu}$ production before $\tilde{\mu}$ decay whereas for high masses the angular distribution is quite flat.

Let us now move to selectron pair production including the decay $\tilde{e} \to e\tilde{\gamma}$. Total cross-sections as a function of m_0 for the three energies $\sqrt{s} = 0.6, 1, 2$ TeV are depicted in Fig. 5. The zino mass has been fixed to $m_{\tilde{Z}} = m_{\tilde{\gamma}} + 100$. The bounds on m_0 are those allowed by the phase space when the luminosity reaches 10^{34} cm^{-2} sec^{-1} for $\sqrt{s} = 1, 2$ TeV. The longitudinal asymmetry is given in Table I. The

values are sensitive to the photino mass since when $m_{\tilde{\gamma}} = 100$ GeV, $m_{\tilde{e}_R} \ll m_{\tilde{e}_L}$ especially for the MSIM leading to a change of sign of $A_{\parallel}$ compared with $m_{\tilde{\gamma}} = 10$ GeV. The angular dependence for several choices of m_0 and $m_{\tilde{\gamma}}$ are plotted in Fig. 6 for $\sqrt{s} = 600$ GeV. For m_0 fixed a light photino gives the largest cross-section which is peaked at $\theta = 0°$. When m_0 increases the angular dependence becomes flatter.

We will end with scalar quark production without any decay mechanism. Total cross-sections for u squark pair production are given in Fig. 7 as a function of m_0 for the MSSM. The asymmetry $A_{\parallel}$ is quite constant: $A_{\parallel} \simeq -0.85$. Total cross-sections for d squark pair production are plotted in Fig. 8. The longitudinal asymmetry is also quite constant $A_{\parallel} \simeq 0.13$.

2b - Gaugino pairs $\tilde{W}^+\tilde{W}^-$, $\tilde{Z}\tilde{Z}$, $\tilde{\gamma}\tilde{Z}$

The situation is here slightly less constrained because of the various possibilities of gaugino-Higgsino mixing separately in the charged and in the neutral sector. We will again consider extreme cases defined in 8) where the formulae for polarized cross-sections are also given. We will now directly choose the gaugino masses as free parameters inside the available energy range. Let us first consider wino pair production for four wino-Higgsino mixing cases whose couplings are depicted in Table II. The total cross-sections without any decay consideration are depicted in Figs. 9a, 9b and 9c as a function of $\sqrt{s}$ for three values of the wino mass: $M_{\tilde{W}} = 80$, 200 and 500 GeV with two choices for the $\tilde{\nu}$ mass: $M_{\tilde{\nu}} = 50$ GeV and $M_{\tilde{\nu}} = 200$ GeV. The pure wino case (Model I) gives the highest cross-section. Model III gives similar production rates. Model II gives the lowest cross-section whereas the cross-section for Model IV lies in between. Note that there is no $\tilde{\nu}$ exchange for Model IV. The angular distribution $d\sigma/d\cos\theta_{\tilde{W}}$ is depicted in Fig. 10 for $M_{\tilde{W}} = 100$ GeV at $\sqrt{s} = 0.6$ TeV. In all cases, $d\sigma/d\cos\theta_{\tilde{W}}$ is maximal in the forward direction. Model I gives the most important decreasing with $\theta_{\tilde{W}}$ whereas the angular distribution for Model IV is rather flat. Therefore the integrated forward asymmetry A_{FB} is a relevant quantity to discriminate Model IV from other wino-Higgsino mixing models as shown in Table III. We give in Figs. 11a and 11b the longitudinal asymmetry $A_{\parallel}$ for $M_{\tilde{W}} = 200$ and 500 GeV as a function of $\sqrt{s}$. Away from the production threshold the cross-section is dominated by $\tilde{\nu}$ exchange leading therefore to a large negative asymmetry $A_{\parallel} \simeq -1$. Near threshold we are sensitive to the $\tilde{\nu}$ mass. As shown in Fig. 11a for $M_{\tilde{W}} = 200$ GeV just above $\sqrt{s} = 2M_{\tilde{W}}$ $A_{\parallel}$ is smaller for $m_{\tilde{\nu}} = 200$ GeV. This effect is more pronounced for $M_{\tilde{W}} = 500$ GeV since $A_{\parallel}$ can be positive just above 1 TeV. This reflects a

dominance of the annihilation contribution in this kinematical domain, which is difficult in general to isolate due to the smallness of its cross-section with respect to the $\tilde{\nu}$ contribution.

Let us consider zino pair production without decay. We will only give results for the pure zino case. The total cross-sections are depicted in Fig. 12 as a function of the zino mass. Since the best signal for detection will certainly be one leptonic mode for one zino and one hadronic mode for the other one, giving a product of the branching ratios of about 6.5%, the mass limit for $\sqrt{s}$ = 2 TeV is $M_{\tilde{Z}} \simeq 850$ GeV. The longitudinal asymmetry is given in Table IV. Since the reaction is due to selectron exchange, $A_{\parallel}$ is sensitive to their mass degeneracy for $m_{\tilde{\gamma}}$ = 10 GeV. $A_{\parallel}$ is negative and about -1/3 whereas in the MSIM with $m_{\tilde{\gamma}}$ = 100 GeV, $A_{\parallel}$ is much smaller in magnitude and even can be positive for high masses at $\sqrt{s}$ = 0.6 and 1 TeV since $\tilde{e}_R$ is lighter than $\tilde{e}_L$. The energy dependence of the total cross-section is shown in Figs. 13a, 13b and 13c for $M_{\tilde{Z}}$ = 60, 200, 500 GeV. For $m_{\tilde{\gamma}}$ = 10 GeV predictions from MSSM are very close from the MSIM results. For $m_{\tilde{\gamma}}$ = 100 GeV the rates are smaller for the MSIM since the mass spectrum of selectrons is larger. The longitudinal asymmetry $A_{\parallel}$ is plotted in Fig. 14 as a function of $\sqrt{s}$ showing the sensitivity to selectron mass degeneracy.

The shape of the angular distribution depends on the zino and photino masses. At $\sqrt{s}$ = 600 GeV for $m_{\tilde{Z}}$ = 100 GeV and $m_{\tilde{\gamma}}$ = 10 GeV $d\sigma/d\cos\theta_{\tilde{Z}}$ is maximal at $\theta = 90°$ and smaller by roughly two orders of magnitude at $\theta = 0°$. For heavier zino masses the cross-section is quite flat with a maximum at $\theta = 0°$. For $m_{\tilde{\gamma}}$ = 100 GeV in the MSIM $d\sigma/d\cos\theta_{\tilde{Z}}$ is minimal at $\theta = 0°$ and increases up to $\theta = 90°$.

Let us finally give our prediction for the reaction $e^+e^- \to \tilde{\gamma}\tilde{Z}$ without zino decay and for the pure zino case. The total cross-section is plotted in Fig. 15a (resp. 15b) as a function of the zino mass for $\sqrt{s}$ = 0.6 and 1 TeV (resp. 2 TeV). This reaction is well suited for zino search since one can reach $M_{\tilde{Z}} \simeq 980$ GeV with $m_{\tilde{\gamma}}$ = 10 GeV and $M_{\tilde{Z}}$ = 880 GeV with $m_{\tilde{\gamma}}$ = 100 GeV at $\sqrt{s}$ = 1 TeV. Like for zino pair production it can be seen from inspection of Table V that $A_{\parallel}$ deviates strongly from the value -19% expected when selectron masses are quite degenerate ($m_{\tilde{\gamma}}$=10 GeV) (see the MSIM prediction with $m_{\tilde{\gamma}}$=100 GeV). Total cross-sections are depicted in Figs. 16a and 16b for $M_{\tilde{Z}}$ = 60, 200 and 500 GeV as a function of $\sqrt{s}$. The energy dependence of $A_{\parallel}$ is shown in Fig. 17. For small zino masses the angular distribution $d\sigma/d\cos\theta_{\tilde{Z}}$ is minimal at $\theta = 0°$ and rather flat between 35° and 90°. For heavier zinos some structure appears in the $\theta_{\tilde{Z}}$ dependence. The shape of $d\sigma/d\cos\theta_{\tilde{Z}}$ depends weakly on the photino mass.

3. - COMPOSITENESS EFFECTS IN $e^+e^- \to W^+W^-$, ZZ, γZ AND $\gamma\gamma$

We now discuss the effects of anomalous terms in these four reactions. The standard contribution (ν,γ,Z exchange in W^+W^- and e exchange in the three neutral channels) gives a strong forward peaking. In the case of $e^+e^- \to \gamma Z$ and $\gamma\gamma$ we introduce an angular cut $\theta_\gamma > 5°$ in order to avoid the forward divergence. As a consequence of this forward peaking, anomalous effects should be searched essentially in the backward region for $e^+e^- \to W^+W^-$ and in the central region ($\theta \simeq 90°$) for $e^+e^- \to ZZ$, γZ and $\gamma\gamma$ (which have symmetrical angular distributions).

Following the analysis done in Ref. 4), we characterize each anomalous term by an effective scale Λ. We will show the Λ dependence of integrated cross-sections at $\sqrt{s}$ = 0.6, 1 and 2 TeV in Figs. 18 to 21a,b,c and for fixed Λ the energy dependences of these cross-sections in Figs. 22a,b,c,d. Angular distributions are plotted for typical cases at $\sqrt{s}$ = 0.6 TeV in Figs. 23a,b,c,d.

Finally, we want to insist on the interest in longitudinal e^- polarization in order to disentangle the various possible sources of departures to standard predictions. The standard longitudinal polarization asymmetry is about -1, -0.35, -0.17, 0 in $e^+e^- \to W^+W^-$, ZZ, γZ and $\gamma\gamma$ respectively. Figures 24a,b illustrate the large sensitivity of $A_\parallel$ to the chiral structure of the anomalous terms.

3a - Leptonic sector

We assume here that $W^\pm$, Z (and γ) are true gauge bosons and consider the possibility of anomalous terms having their source in the leptonic sector. One classical example is the existence of excited lepton states ν^* and e^* coupled to lepton and gauge boson through a magnetic type of coupling. Such states would lead to additional exchange diagrams in the two-boson production processes[4]. We choose to entirely fix the strength of the e^* coupling through the scale $\Lambda = m_{e^*}$, so that we have only one single free parameter to vary. This coupling may be defined with a chirality factor $c-d\gamma^5$ (normalized to $c^2+d^2=1$). We often choose (for reasons of brevity) to illustrate only the "vector" case (c=1, d=0). From a 5% effect on the integrated cross-sections one can reach Λ values of the order of

2.7, 4.5, 8 TeV for ν^* in $e^+e^- \to W^+W^-$ at $\sqrt{s}$ = 0.6, 1, 2 TeV and values about 1.5 to 2 times larger for e^* in the neutral channels (see Table VII).

We then consider residual e^+e^-VV' interactions described by chiral contact terms respecting gauge invariance for each of the vector bosons V and V'. Such terms can represent any kind of substructure phenomenon in an effective way. The strength of the residual interaction is controlled by an effective scale Λ. In Ref. 4) it was shown that the invariant form denoted R^2_{TT} led to the largest interference effects with the standard amplitudes. So we will make our illustrations with this peculiar term choosing a given chirality factor $c-d\gamma^5$ specified in each figure. The resulting effective scales Λ which should be observable appear to be comparable (slightly lower) to those mentioned above in the case of excited leptons (see Table VII).

3b - Bosonic sector

We now release the constraint of gauge invariance for the $W^\pm$, Z couplings. Three types of anomalous effects have been previously considered[4]: anomalous three-boson couplings among $W^\pm$, Z and γ, formation of an excited vector boson state (Z*) or isoscalar partner (Y), residual e^+e^-VV' interactions involving longitudinal vector boson component. We will successively treat these three possibilities.

Among all possible CP conserving three-boson couplings (three in the W^+W^- case, five in the neutral ZZ and γZ cases) we have chosen to illustrate only the following cases which appeared[4] to be most typical. A $W^\pm$ quadrupole coupling λ_γ defined in terms of an effective scale as $e\lambda_\gamma = \sqrt{4\pi}(M_W^2/\Lambda^2)$ can be felt up to Λ = 1.2, 2, 3.5 TeV in $e^+e^- \to W^+W^-$ at 0.6, 1, 2 TeV. In $e^+e^- \to ZZ$ one can feel a neutral γZZ anomalous coupling $e\xi_2 = \sqrt{4\pi}(M_Z^2/\Lambda^2)$ up to Λ = 5.8, 12, 33 TeV and in $e^+e^- \to \gamma Z$ one is sensitive to a neutral $\gamma\gamma Z$ anomalous coupling $e^2\xi_4 = \sqrt{4\pi}(M_Z^2/\Lambda^2)$ up to Λ = 3, 8 and 24 TeV.

Let us then call X any new vector boson (Z* or Y). We will only consider the situation where $m_X \equiv \Lambda$ is higher than the available e^+e^- energy. Otherwise the occurrence of a peak in the cross-section is an obvious signal it is needless to be discussed further here. We also choose the strong coupling normalization $g^2/4\pi = 1$ leaving Λ as the only free parameter and we take for illustration the

chirality factor leading to the largest interference with the standard amplitude, i.e., "right" $(1+\gamma^5)$ for W^+W^- and ZZ and "axial" (γ^5) for γZ. The corresponding values of Λ are rather high (see Table VII) especially in ZZ where one reaches 9.5, 19 and 48 TeV.

Finally we examine the effects of residual e^+e^-VV' contact terms with longitudinal $W^\pm$ or Z components. Among the various possibilities presented in Ref. 4) we now restrict our discussion to the form denoted R_{LL} for $e^+e^- \to W_L^+W_L^-$ and $e^+e^- \to Z_L Z_L$ and the one denoted R^3_{TL} for $e^+e^- \to \gamma Z_L$. We again keep the strong coupling normalization with the effective scale Λ and choose the most favourable chirality factor, i.e., the "vector" one. The corresponding bounds are now of the order of 3, 6 and 15 TeV (see Table VII).

4. - CONCLUSIONS

As far as supersymmetric particle search is concerned, bounds on masses are roughly controlled by the beam energy when their branching ratio to the channel used for identification is large. This is the case for sleptons (and also probably for squarks). In the gaugino cases $(\tilde{W},\tilde{Z})$ if one relies on leptonic branching ratios of the order of a few per cent the highest luminosity is welcome in order to really reach these bounds. Typical numbers are collected in Table VI. Notice the improvement with respect to present bounds and to those accepted with LEP II and HERA (roughly 80÷90 GeV[9]).

In order to clearly distinguish supersymmetric particle production from background and even more to recognize the nature of the particle produced and its couplings, asymmetries and especially longitudinal polarization asymmetry $A_\parallel$ will be very powerful. We have illustrated the spectacular properties of non-degenerate sleptons (as compared to degenerate ones) and the sensitivity to the various models of wino-Higgsino mixing. The sign of $A_\parallel$ very often appears to provide a decisive information about the type of particle produced.

A 0.6 TeV machine should be able to check if there exist supersymmetric particles closely connected to W, Z masses and a 2 TeV machine should probably definitely conclude whether supersymmetry exists in the TeV range and has something to do with the electroweak interaction scale.

Concerning the search for compositeness effects, Table VII collects the resulting limiting values on effective scales which can be found for each type of

anomalous term. At $\sqrt{s}$ = 0.6, 1, 2 TeV, they are roughly 3, 6, 12 times larger than the corresponding ones expected to be obtained with LEP 200[4),9)]. We insist on the fact that these bounds are obtained from the only requirement of a 5% departure from the standard value, but could certainly be improved by a high statistics measurement in the backward (or central) region. Angular distributions at $\sqrt{s}$ = 0.6 TeV were plotted in various typical cases for this purpose. From the size of the effects around 180° in W^+W^- or 90° in the neutral channels one can expect to be able to improve these bounds by a factor 2 to 3. The highest luminosity is here essential because of the low cross-sections in these angular regions.

It appears that in any case one will largely enter in the TeV range with a 0.6 TeV machine and in the tens of TeV range with a 1÷2 TeV machine. If the observation of a departure to standard prediction were made it would not be immediately obvious to identify its source (i.e., which type of anomalous term) even by looking at s- or θ-dependence of the effect. For this reason, longitudinal polarization will again be powerful. On the one hand it gives an independent information allowing a better amplitude analysis and on the other hand it is especially sensitive to the chiral structure of the anomalous effect and can then help for its characterization (see Figs. 24a,b).

In the leptonic sector, the information brought up by these two-boson channels will be complementary to those obtained from the four-fermion interaction. Although the bounds expected from the latter are much higher (i.e., Λ values in the range of 100 TeV with a 2 TeV e^+e^- machine[2)]), the two-boson channels test the occurrence of high mass e*, ν* or other intermediate state exchange where the effective Λ value has not necessarily the same physical meaning. One must also notice that the idea of compositeness in the leptonic sector is not associated with a precise range of Λ values.

The situation is different in the bosonic sector. On the one hand there is up to now practically no limitation on a possible W, Z substructure and LEP 200 will just approach the TeV range. On the other hand there are many theoretical reasons[1),2)] to expect new phenomena in this sector in the TeV range.

So for both supersymmetry and compositeness we eagerly wait for the realization of such projects of high energy e^+e^- colliders.

$\sqrt{s}$ (TeV)	$m_{\tilde{\gamma}}$ (GeV) / m_0 (GeV)	10		100	
		MSIM	MSSM	MSIM	MSSM
0.6	100	-0.13	-0.04	0.93	0.04
	200	-0.15	-0.055	-	0.1
	250	-0.2	-0.05	-	0,17
1	100	-0.083	-0.04	0.45	-0.02
	200	-0.09	-0.06	0.55	-0.005
	300	-0.1	-0.07	0.6	0.01
	450	-0.16	-0.07	-	0.12
2	100	-0.06	-0.05	0.04	-0.05
	200	-0.07	-0.06	0.06	-0.05
	300	-0.08	-0.07	0.07	-0.04
	450	-0.09	-0.08	0.10	-0.04
	600	-0.09	-0.08	0.14	-0.04
	750	-0.09	-0.08	0.23	-0.04
	900	-0.10	-0.08	0.64	-0.008

Table I- Longitudinal asymmetry $A_{\parallel}$ for selectron pair production as a function of m_0 and $m_{\tilde{\gamma}}$ in the MSIM and MSSM for $\sqrt{s}$ = 0.6, 1, 2 TeV.

Coupling	C_L	$a^{\gamma}_{\tilde{W}}$	$b^{\gamma}_{\tilde{W}}$	$a^{Z}_{\tilde{W}}$	$b^{Z}_{\tilde{W}}$
Model I	$-\frac{1}{\sqrt{2}\ \sin\theta_W}$	-1	0	$-\ \mathrm{cotg}\ \theta_W$	0
Model II	$-\frac{1}{2\ \sin\theta_W}$	-1	0	$-\frac{(3-4\ \sin^2\theta_W)}{2\ \sin 2\theta_W}$	0
Model III	$-\frac{1}{\sqrt{2}\ \sin\theta_W}$	-1	0	$-\frac{(3.4\ \sin^2\theta_W)}{2\ \sin 2\theta_W}$	$\frac{1}{2\ \sin 2\theta_W}$
Model IV	0	-1	0	$-\frac{(3-4\ \sin^2\theta_W)}{2\ \sin 2\theta_W}$	$-\frac{1}{2\ \sin 2\theta_W}$

Table II - $e^+e^- \to \tilde{W}^+\tilde{W}^-$ couplings. C_L is the $e\tilde{\nu}\tilde{W}$ coupling, $a^{X}_{\tilde{W}}$ (resp. $b^{X}_{\tilde{W}}$) is the vector (resp. axial) X coupling to $\tilde{W}^+\tilde{W}^-$ pairs ($X \equiv \gamma, Z$).

		MOD I		MOD II		MOD III		MOD IV	
$\sqrt{s}$	$M_{\tilde{W}}$ \ $M_{\tilde{\nu}}$	50	200	50	200	50	200	50	200
600 GeV	100	0.87	0.78	0.65	0.54	0.85	0.53	0.35	0.35
	200	0.93	0.61	0.87	0.52	0.92	0.45	0.26	0.26
1 TeV	100	0.87	0.79	0.69	0.62	0.83	0.62	0.37	0.37
	200	0.96	0.74	0.87	0.52	0.96	0.61	0.33	0.33
	300	0.96	0.76	0.88	0.4	0.95	0.73	0.28	0.28
	400	0.91	0.78	0.81	0.36	0.89	0.76	0.2	0.2
2 TeV	100	0.86	0.82	0.71	0.68	0.8	0.68	0.37	0.37
	200	0.96	0.80	0.87	0.64	0.95	0.69	0.37	0.37
	300	0.98	0.82	0.94	0.61	0.98	0.76	0.35	0.35
	400	0.98	0.87	0.94	0.64	0.98	0.85	0.33	0.33
	500	0.98	0.91	0.93	0.70	0.98	0.90	0.31	0.31
	600	0.97	0.92	0.91	0.75	0.96	0.91	0.28	0.28
	800	0.91	0.88	0.85	0.73	0.89	0.86	0.19	0.19
	950	0.66	0.64	0.71	0.63	0.62	0.60	0.1	0.1

Table III - Integrated forward backward asymmetry A_{FB} for wino pair production as a function of $M_{\tilde{W}}$ and $M_{\tilde{\nu}}$ at $\sqrt{s}$ = 0.6, 1, 2 TeV for four wino-Higgsino mixing models.

$\sqrt{s}$	$M_{\tilde{Z}}$ \ $M_{\tilde{\gamma}}$	10 MSIM	10 MSSM	100 MSIM	100 MSSM
600 GeV	100	-0.33	-0.32	+0.07	-0.24
	200	-0.34	-0.32	+0.1	-0.17
	260	-0.34	-0.32	+0.16	-0.12
1 TeV	100	-0.33	-0.32	-0.11	-0.28
	200	-0.33	-0.32	-0.1	-0.26
	300	-0.34	-0.32	-0.05	-0.21
	400	-0.33	-0.32	+0.04	-0.2
	460	-0.33	-0.32	+0.12	-0.21
2 TeV	100	-0.33	-0.32	-0.24	-0.31
	200	-0.34	-0.32	-0.24	-0.31
	300	-0.33	-0.32	-0.23	-0.29
	400	-0.33	-0.32	-0.21	-0.26
	500	-0.33	-0.32	-0.17	-0.25
	600	-0.33	-0.32	-0.13	-0.25
	700	-0.33	-0.32	-0.1	-0.27
	800	-0.33	-0.32	-0.09	-0.28
	900	-0.33	-0.32	-0.1	-0.29
	970	-0.33	-0.32	-0.1	-0.29

Table IV - Longitudinal asymmetry for zino pair production at $\sqrt{s}$ = 0.6, 1, 2 TeV as a function of zino and photino masses in the MSIM and in the MSSM.

$\sqrt{s}$	Model / $M_{\tilde{Z}}$	MSIM $m_{\tilde{\gamma}}$ = 10 GeV	MSIM $m_{\tilde{\gamma}}$ = 100 GeV	MSSM $m_{\tilde{\gamma}}$ = 100 GeV
600 GeV	100	-0.17	+0.24	-0.07
	200	-0.18	0.26	-0.05
	300	-0.18	0.3	-0.01
	400	-0.18	0.36	+0.04
	500	-0.19	-	-
1 TeV	100	-0.17	+0.056	-0.12
	200	-0.17	0.06	-0.11
	300	-0.17	0.08	-0.10
	400	-0.17	0.1	-0.08
	500	-0.18	0.13	-0.06
	600	-0.18	0.17	-0.04
	700	-0.18	0.22	-0.02
	800	-0.18	0.29	-0.
	900	-0.19	-	-
2 TeV	100	-0.17	-0.08	-0.15
	300	-0.17	-0.08	-0.15
	500	-0.17	-0.06	-0.13
	700	-0.17	-0.04	-0.12
	900	-0.17	-0.01	-0.10
	1100	-0.17	+0.01	-0.09
	1300	-0.18	+0.05	-0.08
	1500	-0.18	+0.09	-0.07
	1700	-0.18	+0.15	-0.06
	1900	-0.18	-	-

Table V - Longitudinal asymmetry for $e^+e^- \to \tilde{\gamma}\tilde{Z}$ at $\sqrt{s}$ = 0.6, 1, 2 TeV as a function of zino mass in the MSIM and the MSSM.

$\sqrt{s}$ (TeV)	$m_{\tilde{\mu}}$	$m_{\tilde{e}}$	$m_{\tilde{q}}$	$M_{\tilde{W}}$	$M_{\tilde{Z}}$
0.6	280	280	260	290	550
1.0	480 (490)	460 (485)	460 (480)	480 (490)	970 (975)
2.0	900 (980)	900 (960)	850 (920)	920 (985)	1970 (1975)

Table VI - Limiting values for supersymmetric particle masses assuming an e^+e^- luminosity of 10^{33} (10^{34}) cm^{-2} sec^{-1} and $m_{\tilde{\gamma}}$ = 10 GeV.

WW	$\sqrt{s}$ (TeV)	$\Lambda_{\nu\nu^*,A}$	Λ_{TT2_L}	Λ_{λ_γ}	Λ_{Y_R}	Λ_{LL_V}
	0.6	2.7	2.0	1.2	5.3	3.0
	1.0	4.5	3.0	2.0	11.0	6.5
	2.0	8.0	5.5	3.5	29.0	17.0
ZZ	$\sqrt{s}$ (TeV)	$\Lambda_{e\nu^*}$	Λ_{TT2_L}	Λ_{ξ_2}	Λ_{X_R}	Λ_{TL2_V}
	0.6	4.8	2.8	5.8	9.5	3.3
	1.0	8.0	4.0	12.0	19.0	6.0
	2.0	15.0	8.0	33.0	48.0	13.0
γZ	$\sqrt{s}$ (TeV)	$\Lambda_{e\nu^*}$	Λ_{TT2_A}	Λ_{ξ_4}	Λ_{X_A}	Λ_{TL3_V}
	0.6	4.0	1.8	3.0	2.0	2.0
	1.0	6.0	3.0	8.0	5.0	4.5
	2.0	12.0	7.0	24.0	13.0	10.0
$\gamma\gamma$	$\sqrt{s}$ (TeV)	$\Lambda_{e\nu^*,A}$	$\Lambda_{e^*_{L,R}}$	Λ_{TT2_V}	$\Lambda_{TT2_{L,R}}$	Λ_{TT2_A}
	0.6	3.5	2.5	2.2	2.0	1.3
	1.0	6.0	4.2	3.7	3.1	2.4
	2.0	12.0	8.5	7.0	6.0	4.5

Table VII - Limiting values for Λ (TeV) (obtained by a 5% departure on integrated cross-sections).

REFERENCES

1) H. Harari - SLAC-PUB-4223 (presented at SLAC Summer Institute, 1986);
M.E. Peskin - Proceedings of the International Symposium on Lepton and Photon Interactions at High Energies, Kyoto, 1985, eds. M. Konuma and K. Takahashi (Kyoto University, 1985);
J. Ellis - ibid.

2) V. Angelopoulos et al. - CERN Preprint TH. 4682 (1987) (Reported presented by J. Ellis and F. Pauss at the Workshop on Physics at Future Accelerators, La Thuile and CERN, January 1987).

3) Proceedings of the ECFA-CERN Workshop on a L.H.C. in the LEP Tunnel, Lausanne and CERN, 1984, ed. M. Jacob (ECFA 84/85, CERN 84-10);
Proceedings of the 1986 Summer Study on the Physics of the SSC, Snowmass, Colorado, 1986, eds. R. Donaldson and J. Marx;
Proceedings of the Workshop on Physics at Future Accelerators, La Thuile and CERN, January 1987.

4) P. Méry, M. Perrottet and F.M. Renard - CPT-86/P.1919 (1986) to appear in Z.Phys. C, Particles and Fields; and CERN Preprint TH. 4741 (1987).

5) F.M. Renard - Proceedings of the Conference "Tests of Electroweak Theories", Trieste, June 1985, eds. B.W. Lynn and C. Verzegnassi, World Scientific Publ., Singapore.

6) P. Chiappetta, F.M. Renard, J. Soffer, P. Sorba and P. Taxil - Nucl.Phys. B259 (1985) 365.

7) MSSM: H. Baer et al. - CERN Report 86-02, Vol. I, p. 297;
MSIM: J. Ellis, K. Enqvist, D.V. Nanopoulos and F. Zwirner - Mod.Phys.Lett. A1 (1986) 57; Nucl.Phys. B276 (1986) 14.

8) P. Chiappetta, F.M. Renard, J. Soffer, P. Sorba and P. Taxil - Nucl.Phys. B262 (1985) 495; Erratum, Nucl.Phys. B279 (1987) 824.

9) A. Blondel et al. - CERN-EP/87-50 (Report presented by D. Treille at LEP 200 ECFA Workshop, Aachen, 1986);
F. Bianchi et al. - CERN-EP/87-24 (Report presented by C. Dionisi at LEP 200 ECFA Workshop, Aachen, 1986).

FIGURE CAPTIONS

Fig. 1 Total cross-section for $e^+e^- \to \tilde{\mu}^+\tilde{\mu}^- \to \mu^+\mu^-\tilde{\gamma}\tilde{\gamma}$ versus m_0 for $\sqrt{s}$ = 0.6, 1, 2 TeV. Full curves: MSIM; dashed curves: MSSM. Points correspond to $m_{\tilde{\gamma}}$ = 10 GeV and triangles to $m_{\tilde{\gamma}}$ = 100 GeV.

Fig. 2 Total cross-section for $e^+e^- \to \tilde{\mu}^+\tilde{\mu}^- \to \mu^+\mu^-\tilde{\gamma}\tilde{\gamma}$ as a function of $\sqrt{s}$ for three values of m_0. Points correspond to m_0 = 60 GeV, crosses to m_0 = 200 GeV and triangles to m_0 = 600 GeV. Full curves: MSIM with $m_{\tilde{\gamma}}$ = 10 GeV; dashed curves: $m_{\tilde{\gamma}}$ = 100 GeV; double-dot-dashed curves: MSSM with $m_{\tilde{\gamma}}$ = 0.

Fig. 3 Longitudinal asymmetry $A_{\parallel}$ for $e^+e^- \to \tilde{\mu}^+\tilde{\mu}^- \to \mu^+\mu^-\tilde{\gamma}\tilde{\gamma}$ as a function of $\sqrt{s}$. Same caption as for Fig. 2.

Fig. 4 Angular distribution $d\sigma/d\cos\theta_\mu$ for different values of m_0 and $m_{\tilde{\gamma}}$ in the MSIM and in the MSSM at $\sqrt{s}$ = 600 GeV.

Fig. 5 Total cross-section for $e^+e^- \to \tilde{e}^+\tilde{e}^- \to e^+e^-\tilde{\gamma}\tilde{\gamma}$ as a function of m_0 for $\sqrt{s}$ = 0.6, 1, 2 TeV in the MSIM. The points correspond to $m_{\tilde{\gamma}}$ = 10 GeV and triangles to $m_{\tilde{\gamma}}$ = 100 GeV.

Fig. 6 Angular distribution $d\sigma/d\cos\theta_e$ for selectron pair production at $\sqrt{s}$ = 600 GeV for several values of m_0 and $m_{\tilde{\gamma}}$ in the MSIM and in the MSSM.

Fig. 7 Total cross-section for scalar u quark pair production without decay as a function of m_0 for $m_{\tilde{\gamma}}$ = 10 GeV (full curve) and $m_{\tilde{\gamma}}$ = 100 GeV (dashed curve) in the MSSM.

Fig. 8 Total cross-section for scalar d quark pair production without decay. Same caption as for Fig. 7.

Fig. 9 Total cross-section for wino pair production without decay as a function of $\sqrt{s}$ for four wino-Higgsino mixing models. Points correspond to $M_{\tilde{\nu}}$ = 50 GeV and triangles to $M_{\tilde{\nu}}$ = 200 GeV.
9a: $M_{\tilde{W}}$ = 60 GeV; 9b: $M_{\tilde{W}}$ = 200 GeV; 9c: $M_{\tilde{W}}$ = 500 GeV.

Fig. 10 Angular distribution $d\sigma/d\cos\theta_{\tilde{W}}$ at $\sqrt{s}$ = 600 GeV for $M_{\tilde{W}}$ = 100 GeV. Full curves: $M_{\tilde{\nu}}$ = 50 GeV; dashed curves: $M_{\tilde{\nu}}$ = 200 GeV.

Fig. 11 Longitudinal asymmetry $A_{\parallel}$ as a function of $\sqrt{s}$.
11a: $M_{\tilde{W}}$ = 200 GeV; 11b: $M_{\tilde{W}}$ = 500 GeV.

Fig. 12 Total cross-section for zino pair production without decay as a function of the zino mass. Full curves: MSIM with $m_{\tilde{\gamma}}$ = 10 GeV; dashed curves: MSIM with $m_{\tilde{\gamma}}$ = 100 GeV; double-dot-dashed curves: MSSM with $m_{\tilde{\gamma}}$ = 100 GeV. The points correspond to $\sqrt{s}$ = 600 GeV, triangles to $\sqrt{s}$ = 1 TeV and crosses to $\sqrt{s}$ = 2 TeV.

Fig. 13 Energy dependence of the total cross-section for zino pair production. Full curves: $M_{\tilde{Z}}$ = 200 GeV; dashed curves: $M_{\tilde{Z}}$ = 500 GeV. The points correspond to MSIM with $m_{\tilde{\gamma}}$ = 10 GeV, the triangles to MSIM with $m_{\tilde{\gamma}}$ = 100 GeV and the crosses to MSSM with $m_{\tilde{\gamma}}$ = 100 GeV.

Fig. 14 Energy dependence of the longitudinal asymmetry $A_{\parallel}$ for zino pair production. Same caption as for Fig. 13. Curves starting at $\sqrt{s}$ = 200 GeV correspond to $M_{\tilde{Z}}$ = 80 GeV.

Fig. 15 Total cross-sections for the reaction $e^+e^- \to \tilde{\gamma}\tilde{Z}$ as a function of $m_{\tilde{Z}}$. The points correspond to MSIM with $m_{\tilde{\gamma}}$ = 10 GeV, the triangles to MSIM with $m_{\tilde{\gamma}}$ = 100 GeV and the crosses to MSSM with $m_{\tilde{\gamma}}$ = 100 GeV.
15a: full curves correspond to $\sqrt{s}$ = 0.6 TeV and the dashed curves to $\sqrt{s}$ = 1 TeV; 15b: $\sqrt{s}$ = 2 TeV.

Fig. 16 Energy dependence of the total cross-section for $e^+e^- \to \tilde{\gamma}\tilde{Z}$ without decay as a function of $\sqrt{s}$. The points correspond to MSSIM with $m_{\tilde{\gamma}}$ = 10 GeV, the triangles to MSIM with $m_{\tilde{\gamma}}$ = 100 GeV and the crosses to MSSM with $m_{\tilde{\gamma}}$ = 100 GeV.
16a: full curves correspond to $M_{\tilde{Z}}$ = 60 GeV and the dashed curves to $M_{\tilde{Z}}$ = 200 GeV; 16b: $M_{\tilde{Z}}$ = 500 GeV.

Fig. 17 Energy dependence of the longitudinal asymmetry $A_{\parallel}$ for $e^+e^- \to \tilde{\gamma}\tilde{Z}$. Same caption as for Fig. 16. The curves starting at $\sqrt{s}$ = 650 GeV correspond to $M_{\tilde{Z}}$ = 600 GeV.

Fig. 18 Integrated cross-sections of $e^+e^- \to W^+W^-$ versus the effective scale Λ for various types of anomalous terms. Full curve: $\nu^*_{V,A}$; dashed: $TT2_L$; dot-dashed: λ_γ; double-dot-dashed: X_R; triple-dot-dashed: LL_V.
18a: $\sqrt{s}$ = 600 GeV; 18b: $\sqrt{s}$ = 1 TeV; 18c: $\sqrt{s}$ = 2 TeV.

Fig. 19 Integrated cross-sections of $e^+e^- \to ZZ$ versus the effective scale Λ for various types of anomalous terms. Full curves: e^*_V (upper curve) or $TT2_A$ (lower curve); dashed curve; X_R; dot-dashed curve; $TL2_V$; double-dot-dashed: ξ_2.
19a: $\sqrt{s}$ = 600 GeV; 19b: $\sqrt{s}$ = 1 TeV; 19c: $\sqrt{s}$ = 2 TeV.

Fig. 20 Integrated cross-sections of $e^+e^- \to \gamma Z$ versus the effective scale Λ for various types of anomalous terms. Full curves: e^*_V (upper curve) or $TT2_A$ (lower curve); dashed: X_A; dotted-dashed: $TL3_V$; double-dot-dashed: ξ_2.
20a: $\sqrt{s}$ = 600 GeV; 20b: $\sqrt{s}$ = 1 TeV; 20c: $\sqrt{s}$ = 2 TeV.

Fig. 21 Integrated cross-sections of $e^+e^- \to \gamma\gamma$ versus the effective scale Λ for various types of anomalous terms. Full curves: $e^*_{V,A}$ (upper curve) or $e^*_{L.R}$ (lower curve). Dashed: $TT2_V$; dot-dashed: $TT2_A$; double-dot-dashed: $TT2_{L,R}$.
21a: $\sqrt{s}$ = 600 GeV; 21b: $\sqrt{s}$ = 1 TeV; 21c: $\sqrt{s}$ = 2 TeV.

Fig. 22 Integrated cross-sections versus the centre-of-mass energy for given effective scales and various types of anomalous terms.
22a: $e^+e^- \to W^+W^-$ (same captions as Fig. 18);
22b: $e^+e^- \to ZZ$ (same captions as Fig. 19);
22c: $e^+e^- \to \gamma Z$ (same captions as Fig. 20);
22d: $e^+e^- \to \gamma\gamma$ (same captions as Fig. 21).

Fig. 23 Angular distributions at $\sqrt{s}$ = 600 GeV for various types of anomalous terms with given effective scales.
23a: $e^+e^- \to W^+W^-$ (same captions as Fig. 18), Λ = 2.5 TeV except for λ_γ (Λ=1 TeV);
23b: $e^+e^- \to ZZ$ (same captions as Fig. 19), Λ = 3 TeV;
23c: $e^+e^- \to \gamma Z$ (same captions as Fig. 20), Λ = 2.5 TeV;
23d: $e^+e^- \to \gamma\gamma$ (same captions as Fig. 21), Λ = 2.2 TeV.

Fig. 24 Longitudinal polarization asymmetry as $\sqrt{s}$ = 600 GeV versus effective scale Λ.

24a: $e^+e^- \to W^+W^-$ including TT2 with several chirality factors;

24b: $e^+e^- \to \gamma Z$ including e* with several chirality factors.

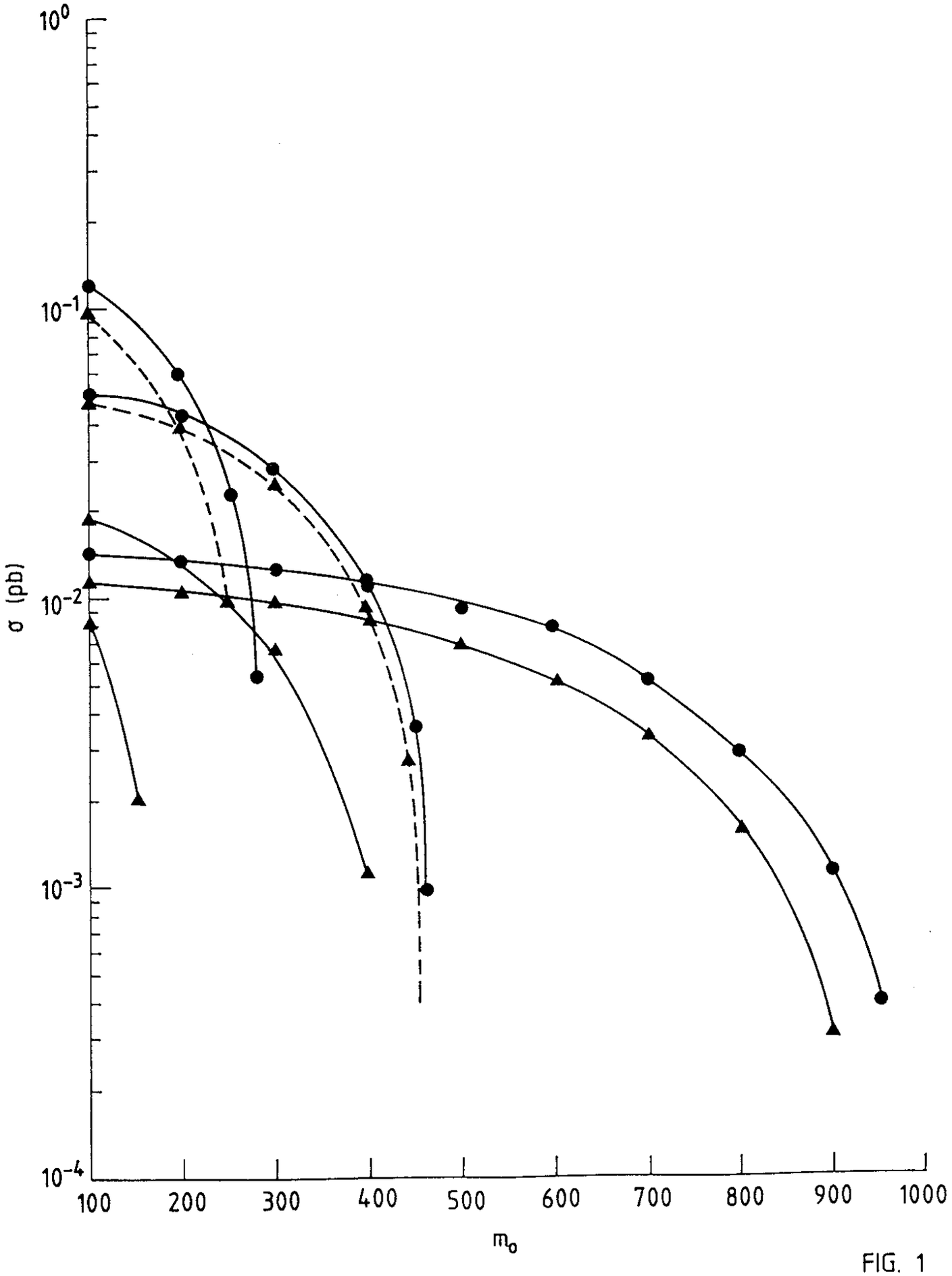
10^0
10^{-1}
10^{-2}
10^{-3}
10^{-4}
σ (pb)
100
200
300
400
500
600
700
800
900
1000
m_0

FIG. 1

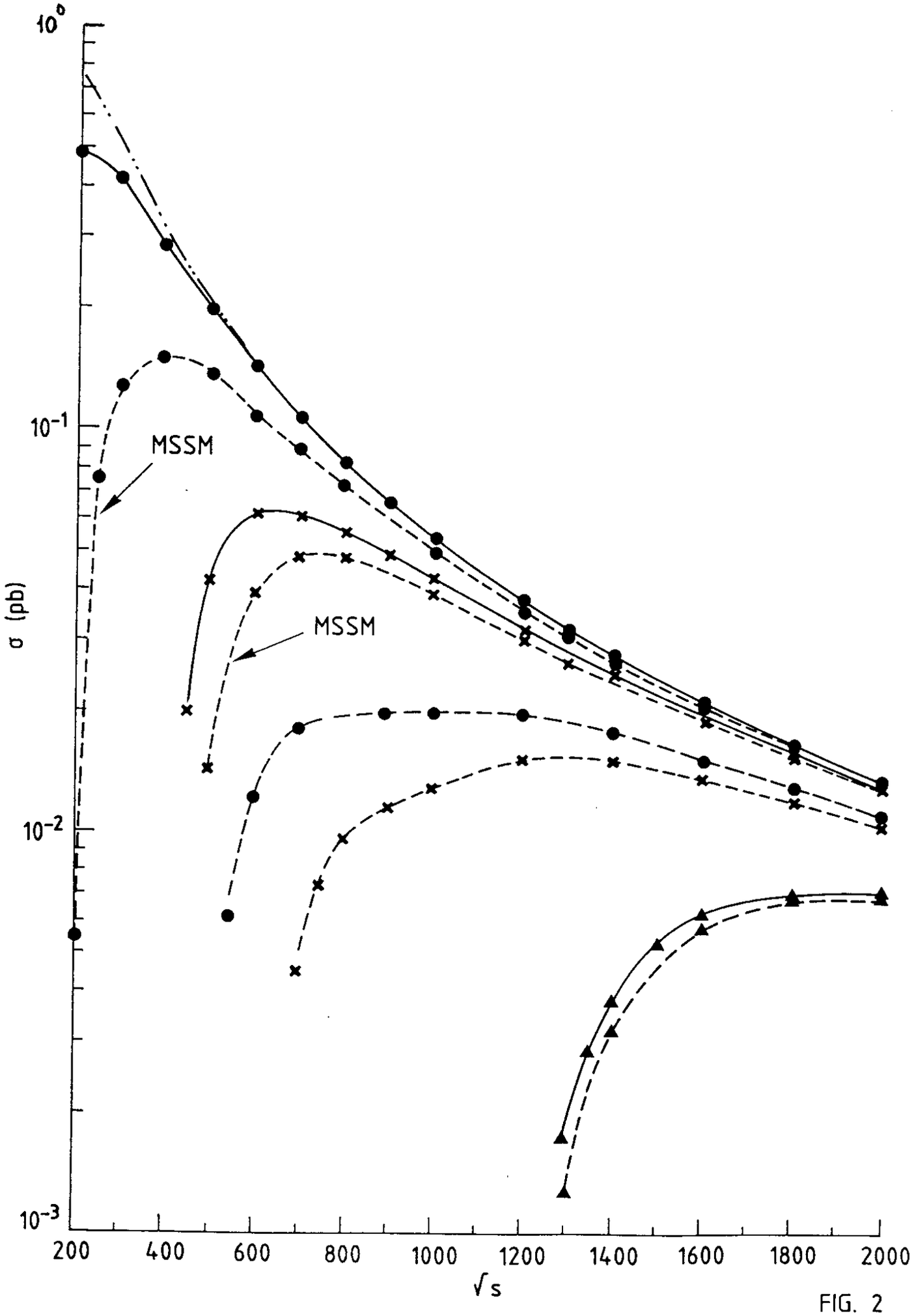
10^0
10^-1
10^-2
10^-3
σ (pb)
MSSM
MSSM
200
400
600
800
1000
1200
1400
1600
1800
2000
√s

FIG. 2

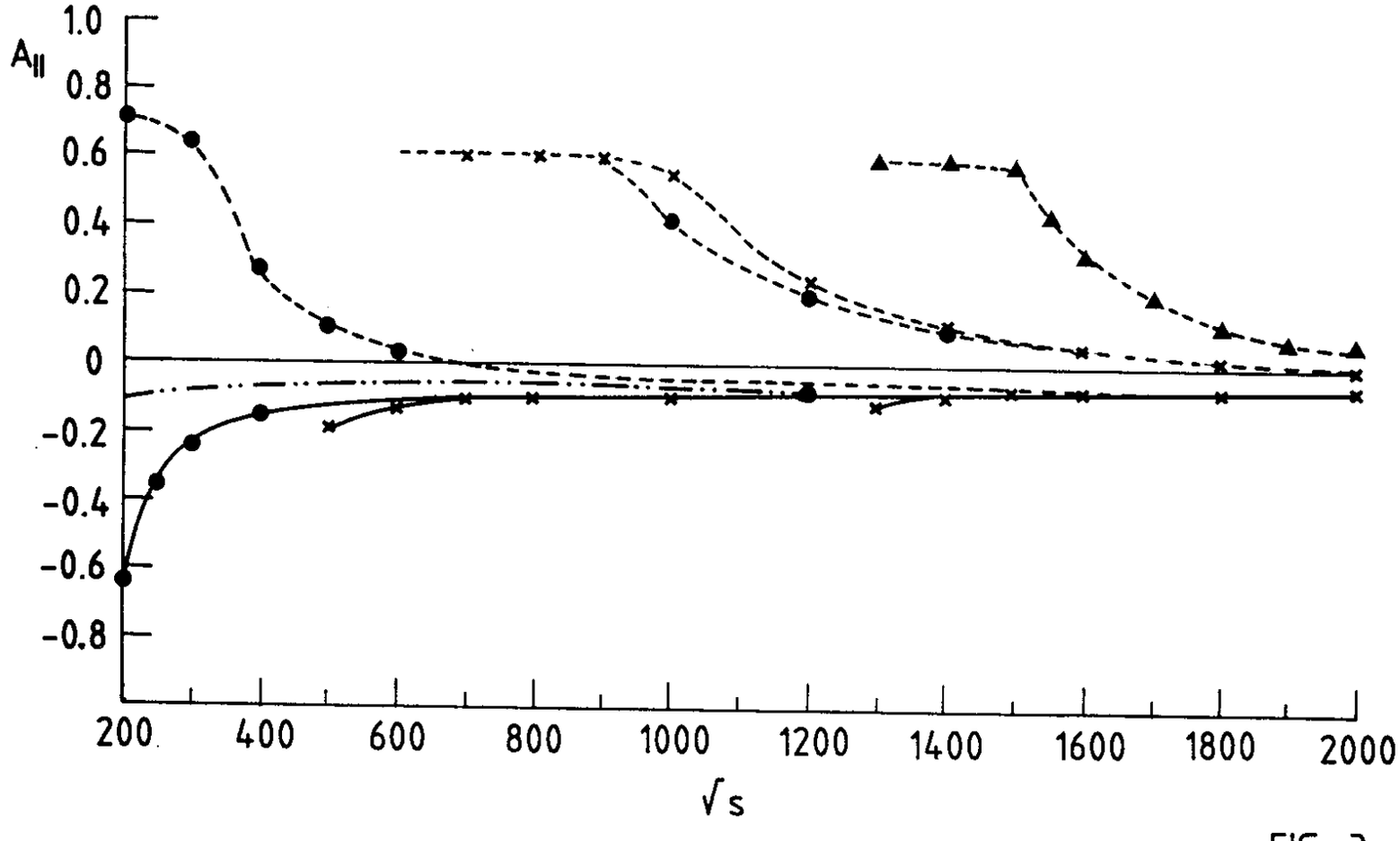
A_{II}
1.0
0.8
0.6
0.4
0.2
0
-0.2
-0.4
-0.6
-0.8
200
400
600
800
1000
1200
1400
1600
1800
2000
$\sqrt{s}$

FIG. 3

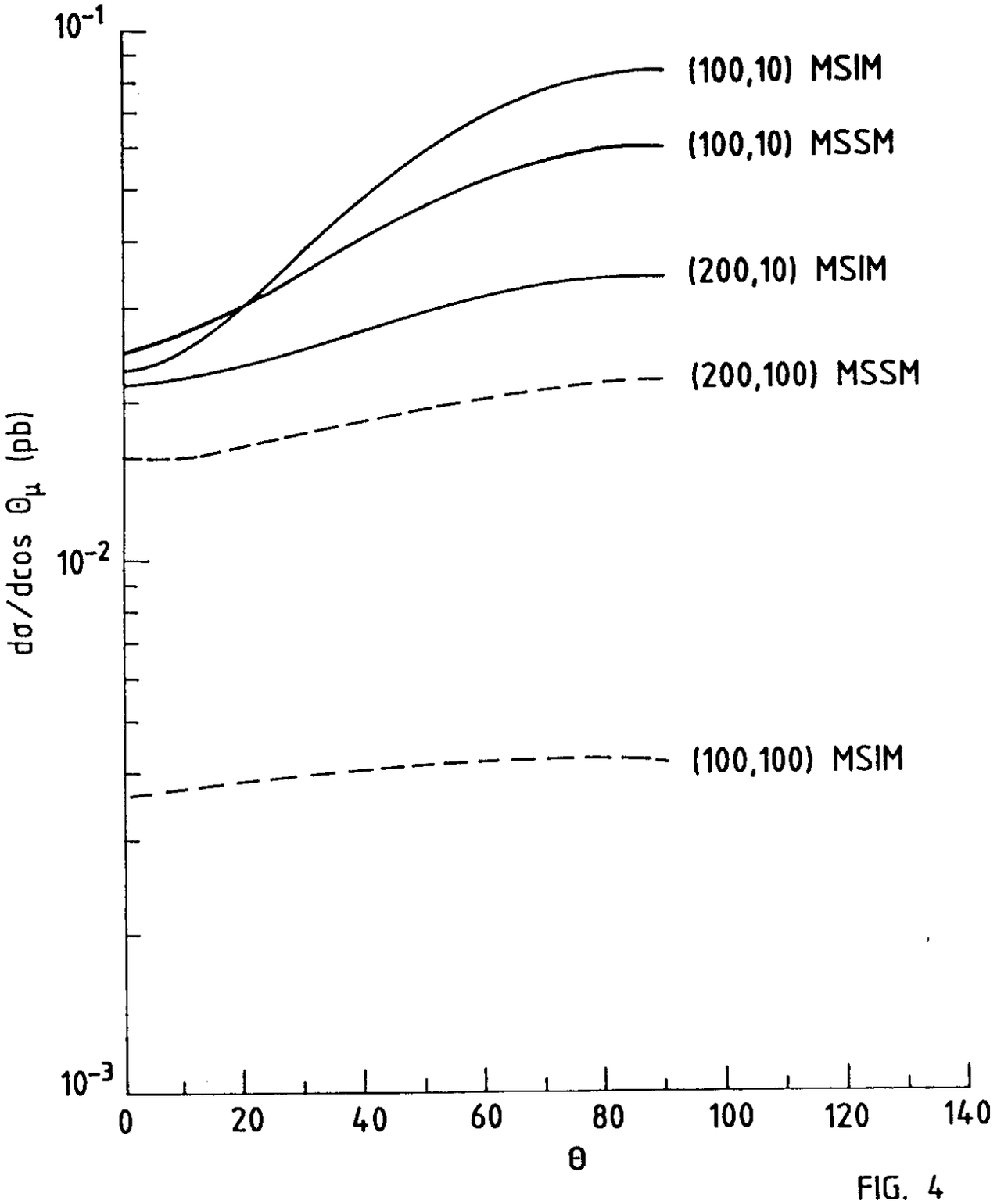
10^{-1}
10^{-2}
10^{-3}
$d\sigma/d\cos\Theta_\mu$ (pb)
(100,10) MSIM
(100,10) MSSM
(200,10) MSIM
(200,100) MSSM
(100,100) MSIM
0
20
40
60
80
100
120
140
Θ

FIG. 4

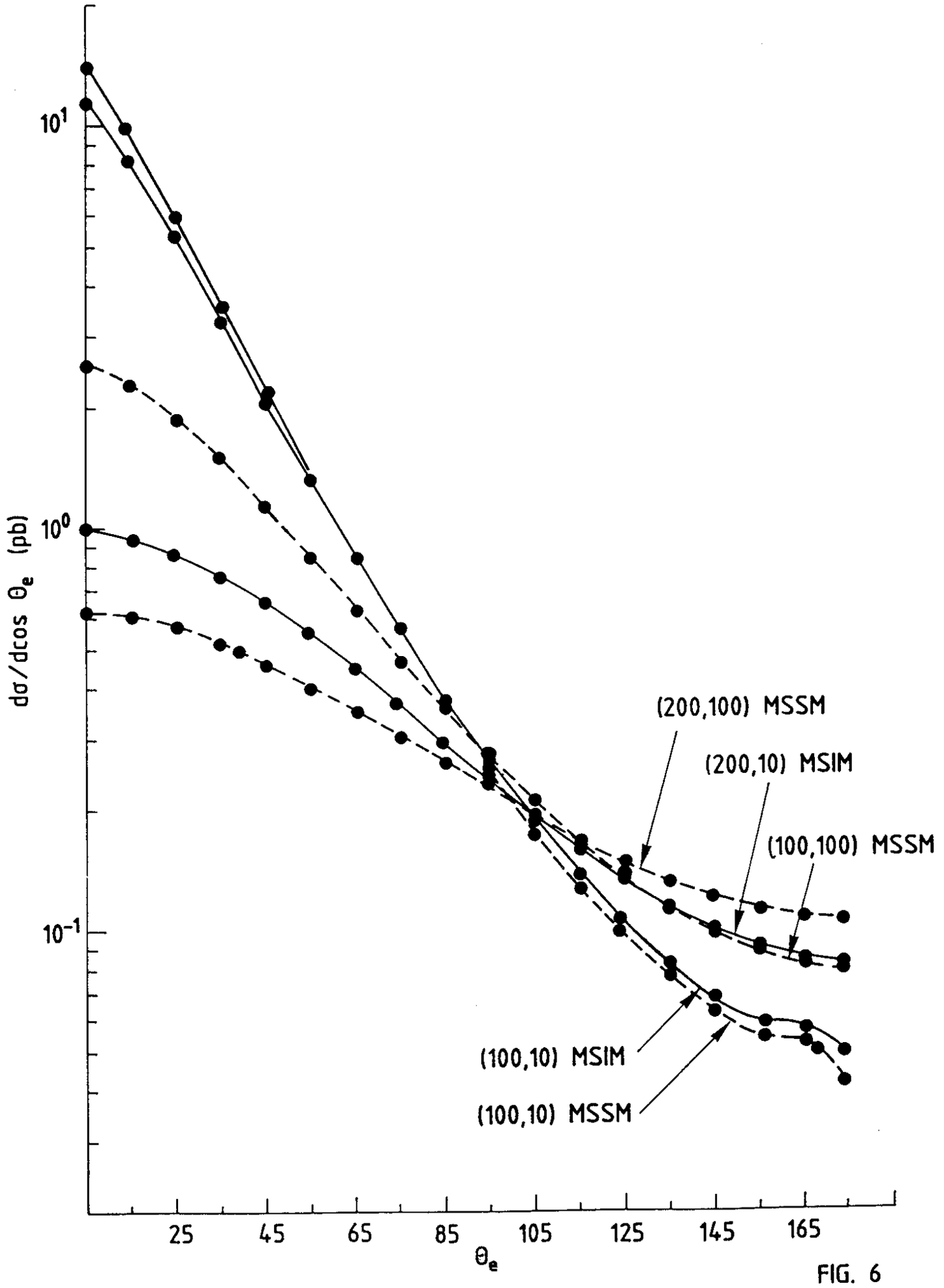
10^1
10^0
10^{-1}
$d\sigma/d\cos\theta_e$ (pb)
25
45
65
85
105
125
145
165
θ_e
(200,100) MSSM
(200,10) MSIM
(100,100) MSSM
(100,10) MSIM
(100,10) MSSM

FIG. 6

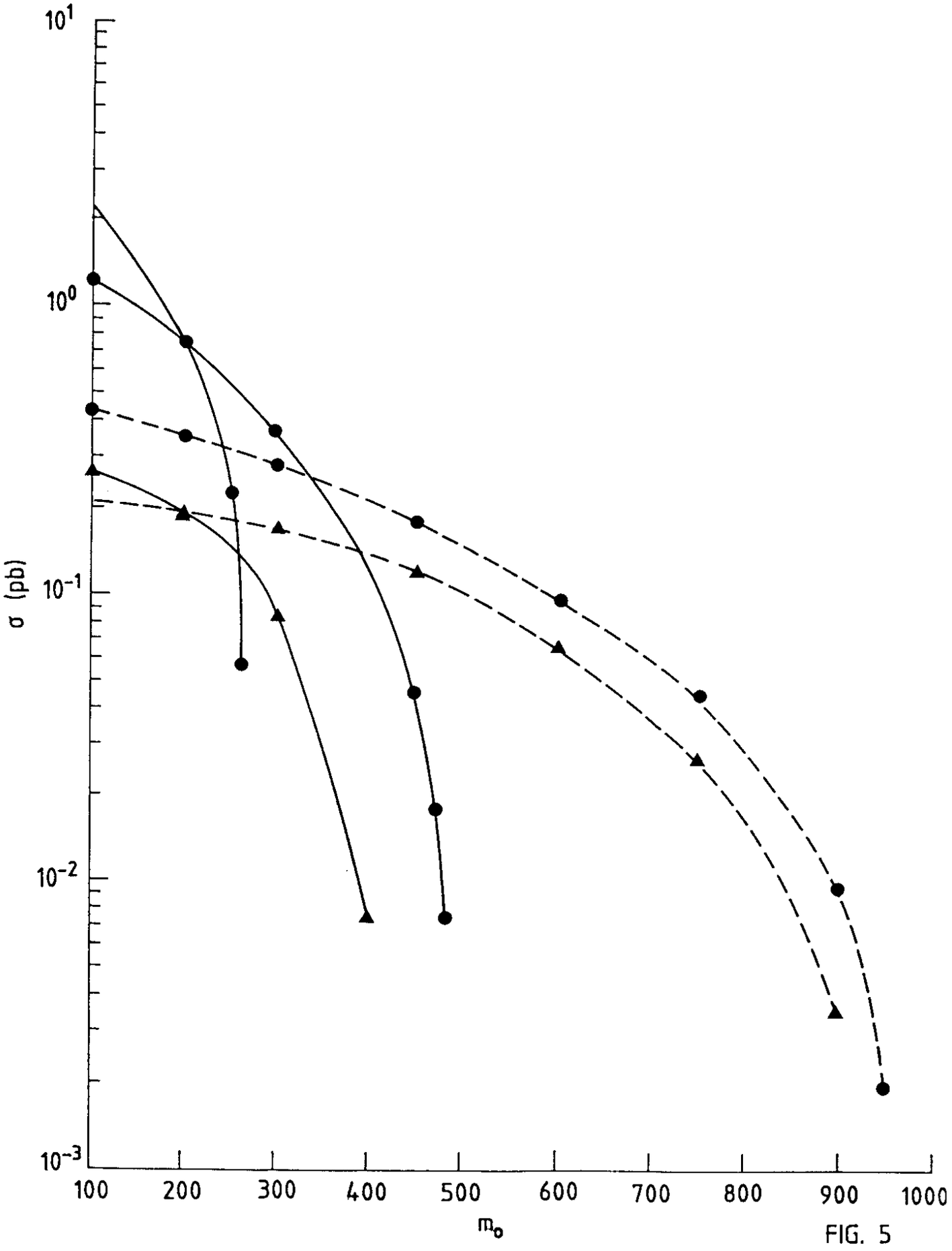
10^1
10^0
10^{-1}
10^{-2}
10^{-3}
σ (pb)
100
200
300
400
500
600
700
800
900
1000
m_o

FIG. 5

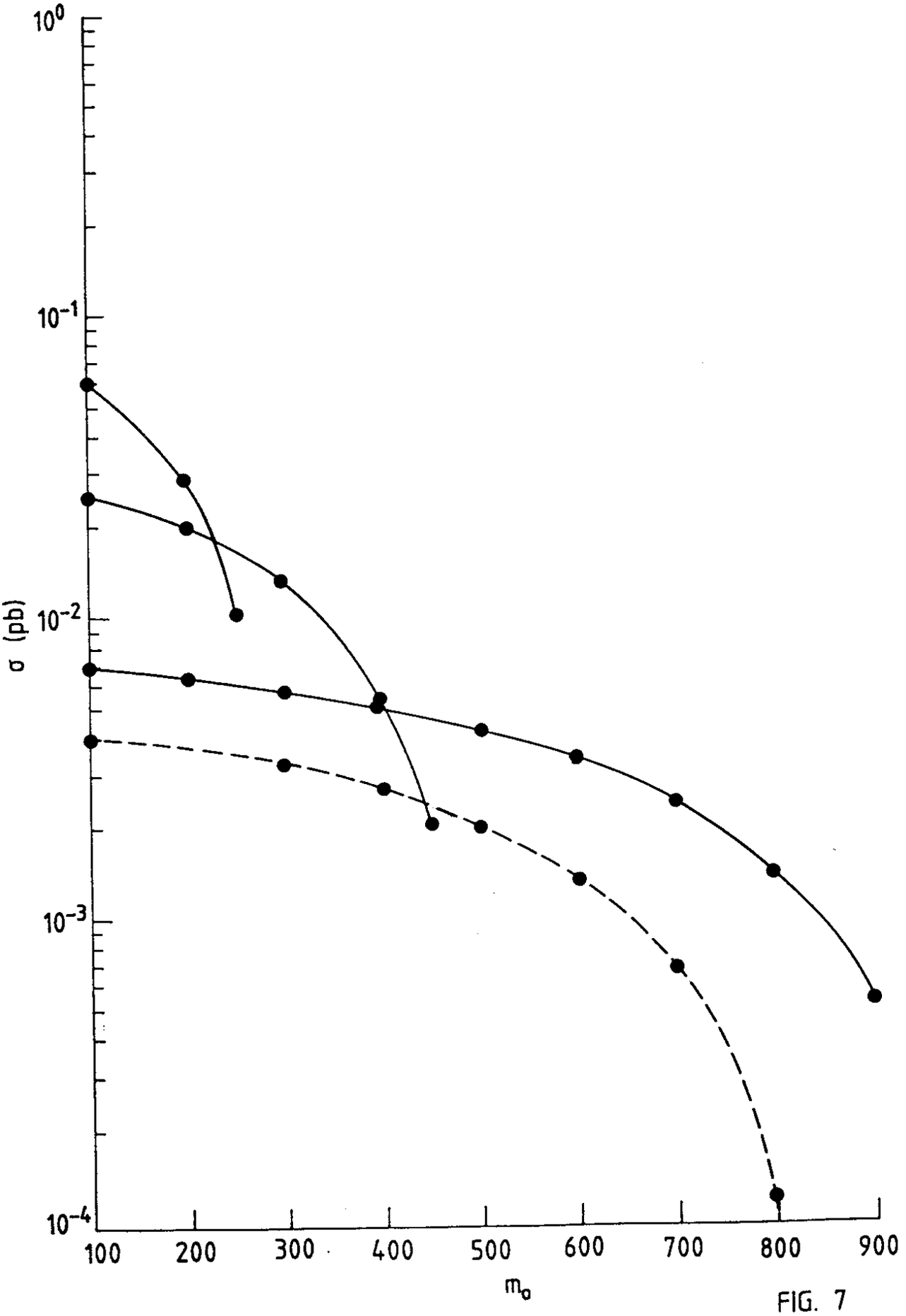

FIG. 7

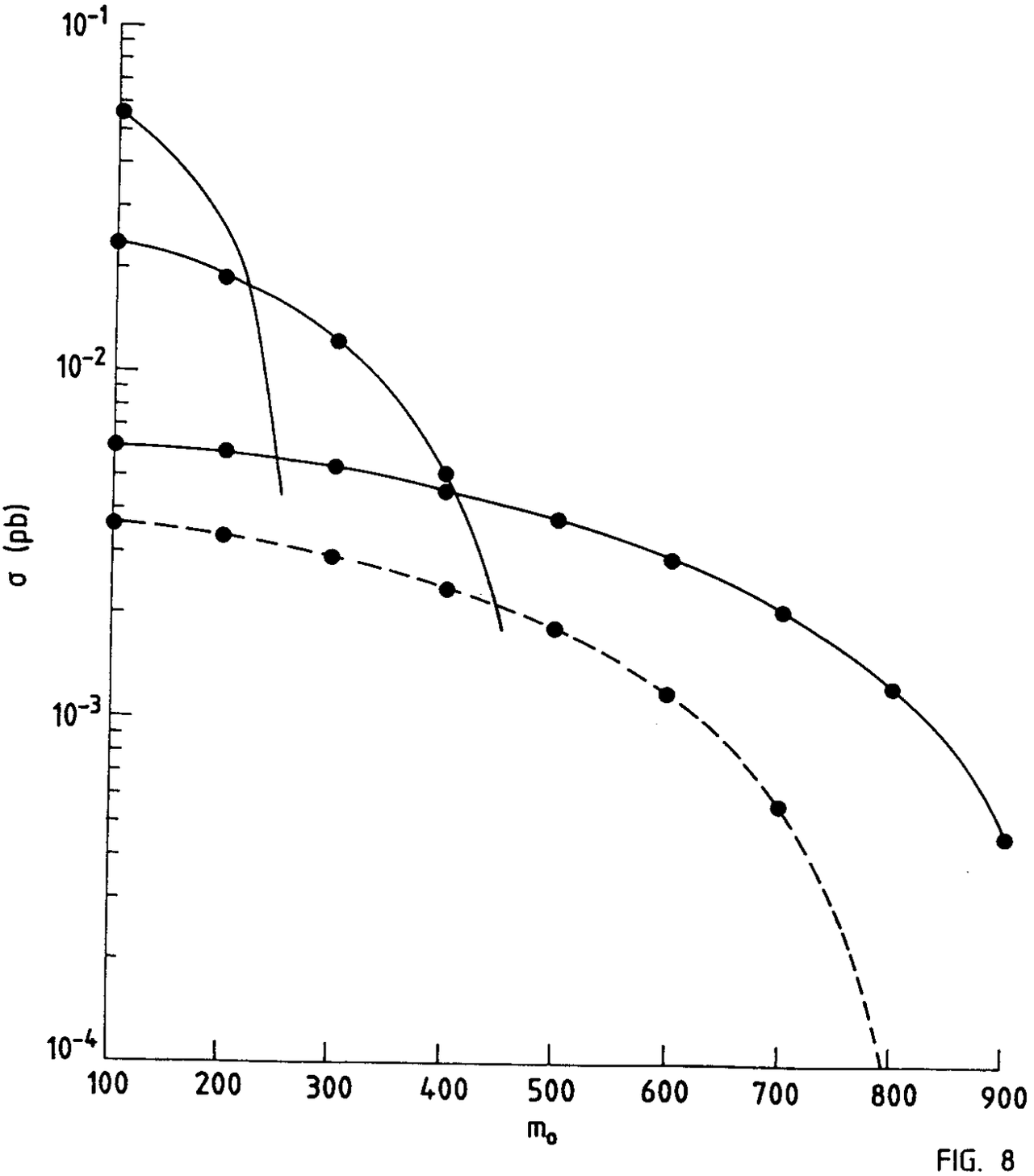

FIG. 8

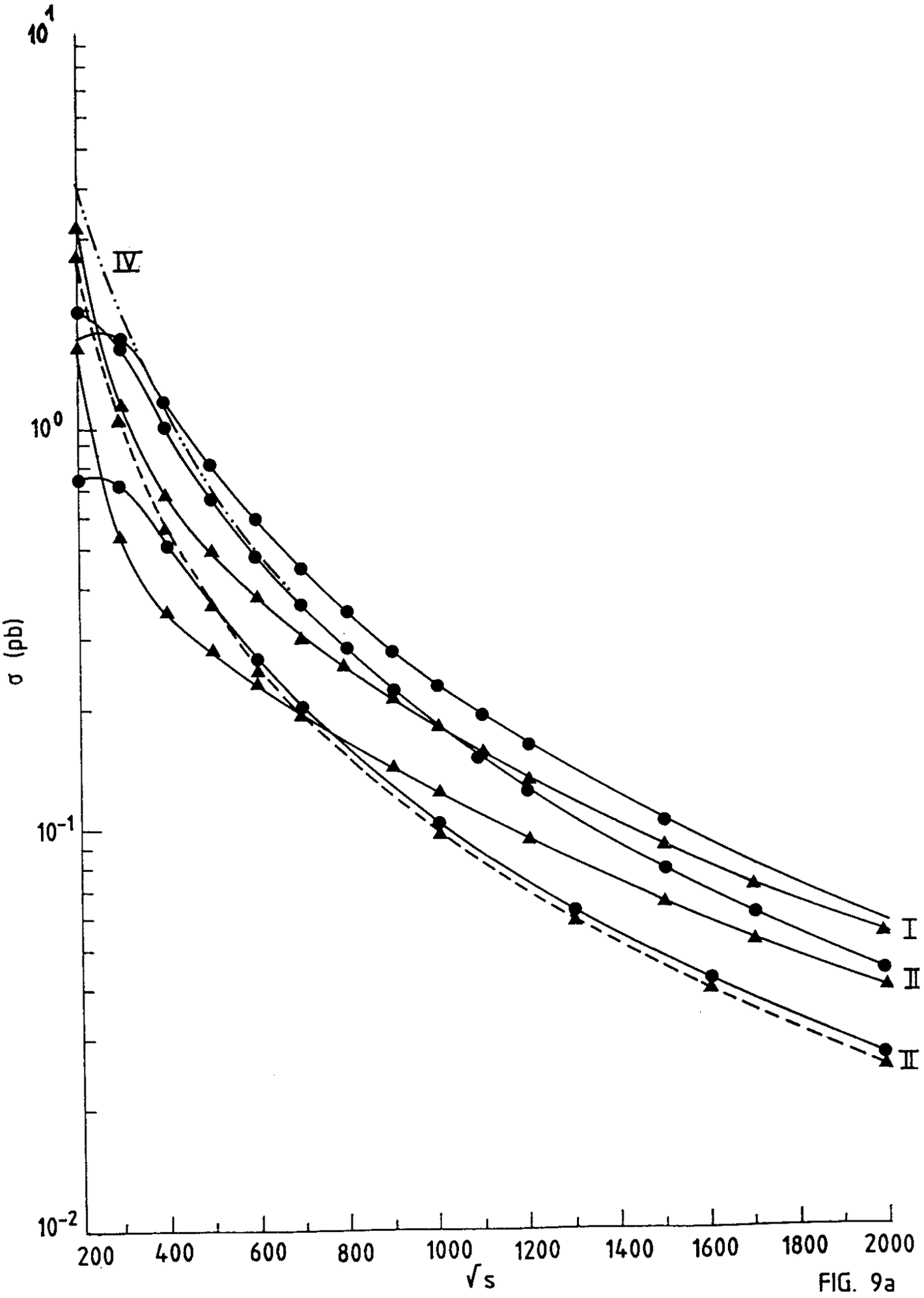
10^1
10^0
10^{-1}
10^{-2}
σ (pb)
IV
I
II
II
200
400
600
800
1000
1200
1400
1600
1800
2000
√s

FIG. 9a

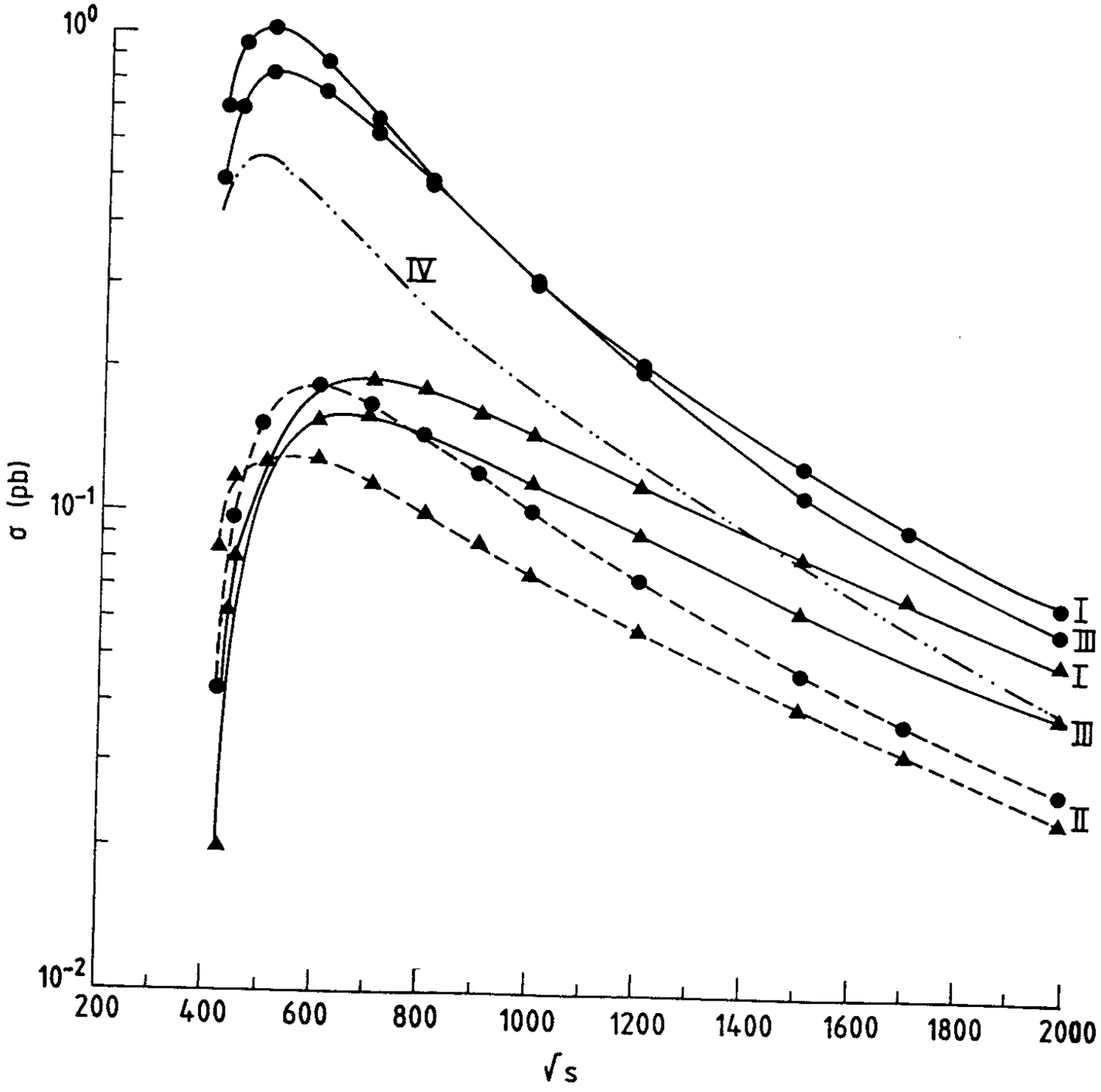
10^0
10^{-1}
10^{-2}
σ (pb)
200
400
600
800
1000
1200
1400
1600
1800
2000
√s
IV
I
III
I
III
II

FIG. 9b

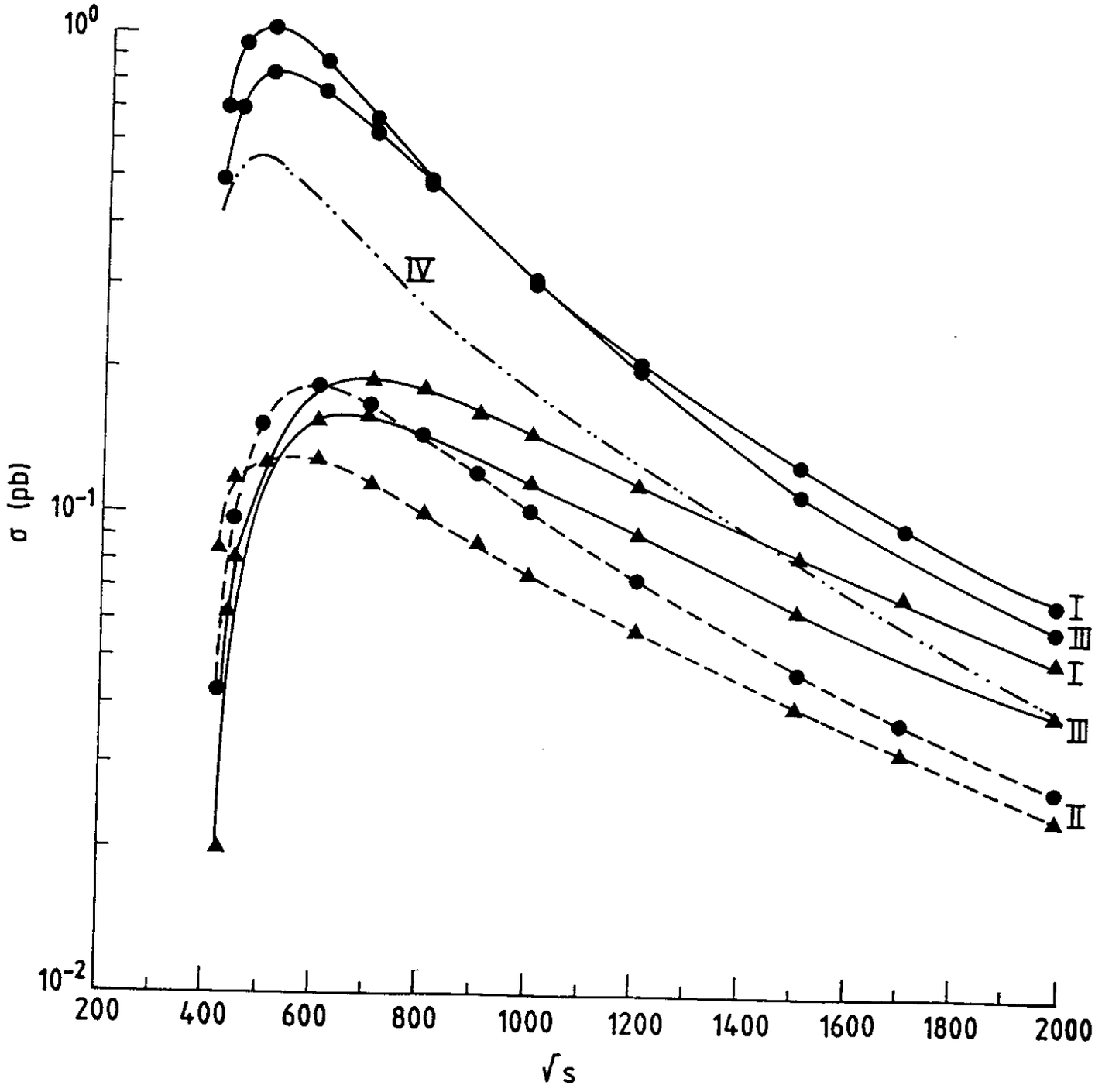
10^0
10^{-1}
10^{-2}
σ (pb)
200
400
600
800
1000
1200
1400
1600
1800
2000
√s
IV
I
III
I
III
II

FIG. 9b

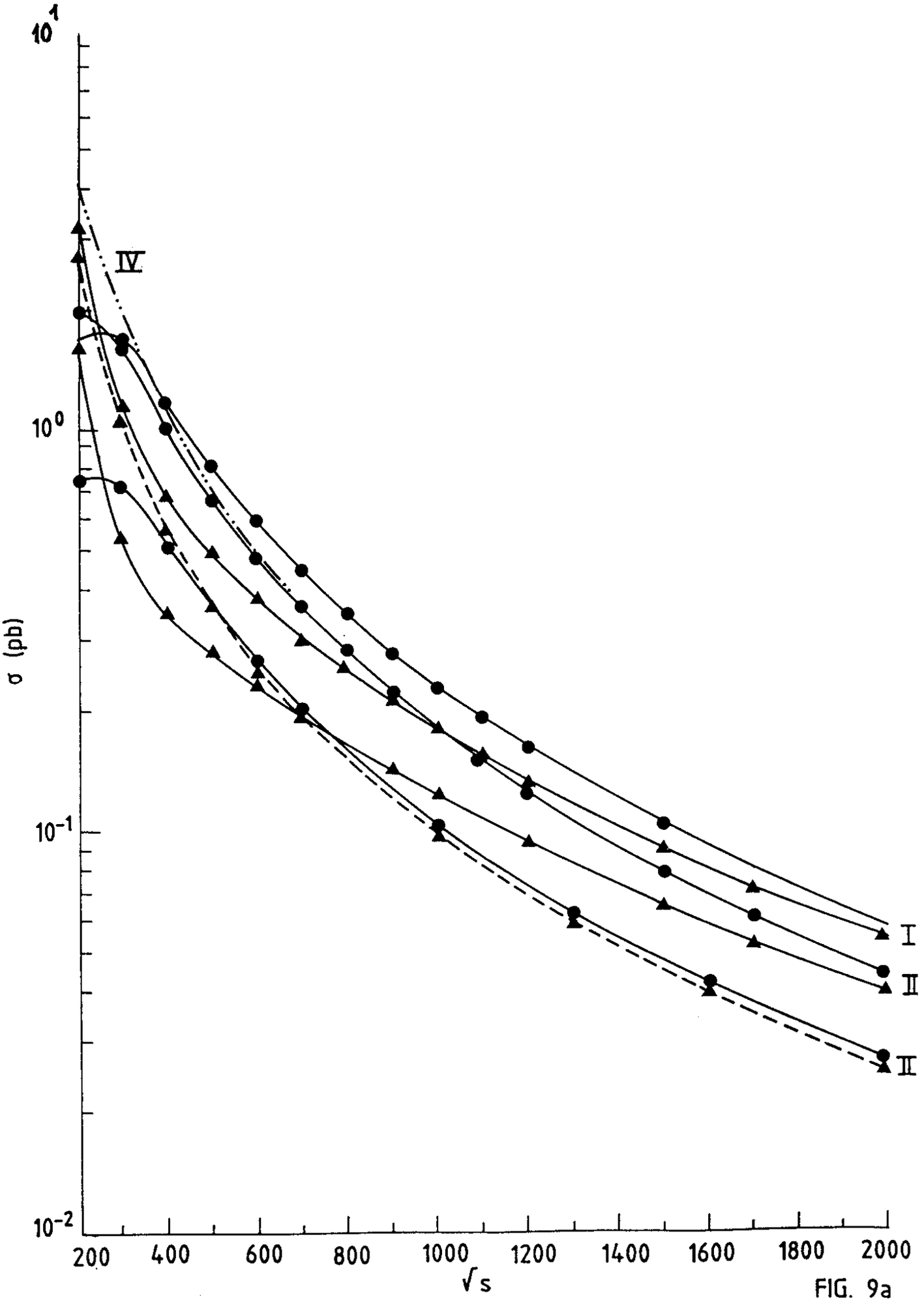
10^1
10^0
10^{-1}
10^{-2}
σ (pb)
IV
I
II
III
200
400
600
800
1000
1200
1400
1600
1800
2000
√s

FIG. 9a

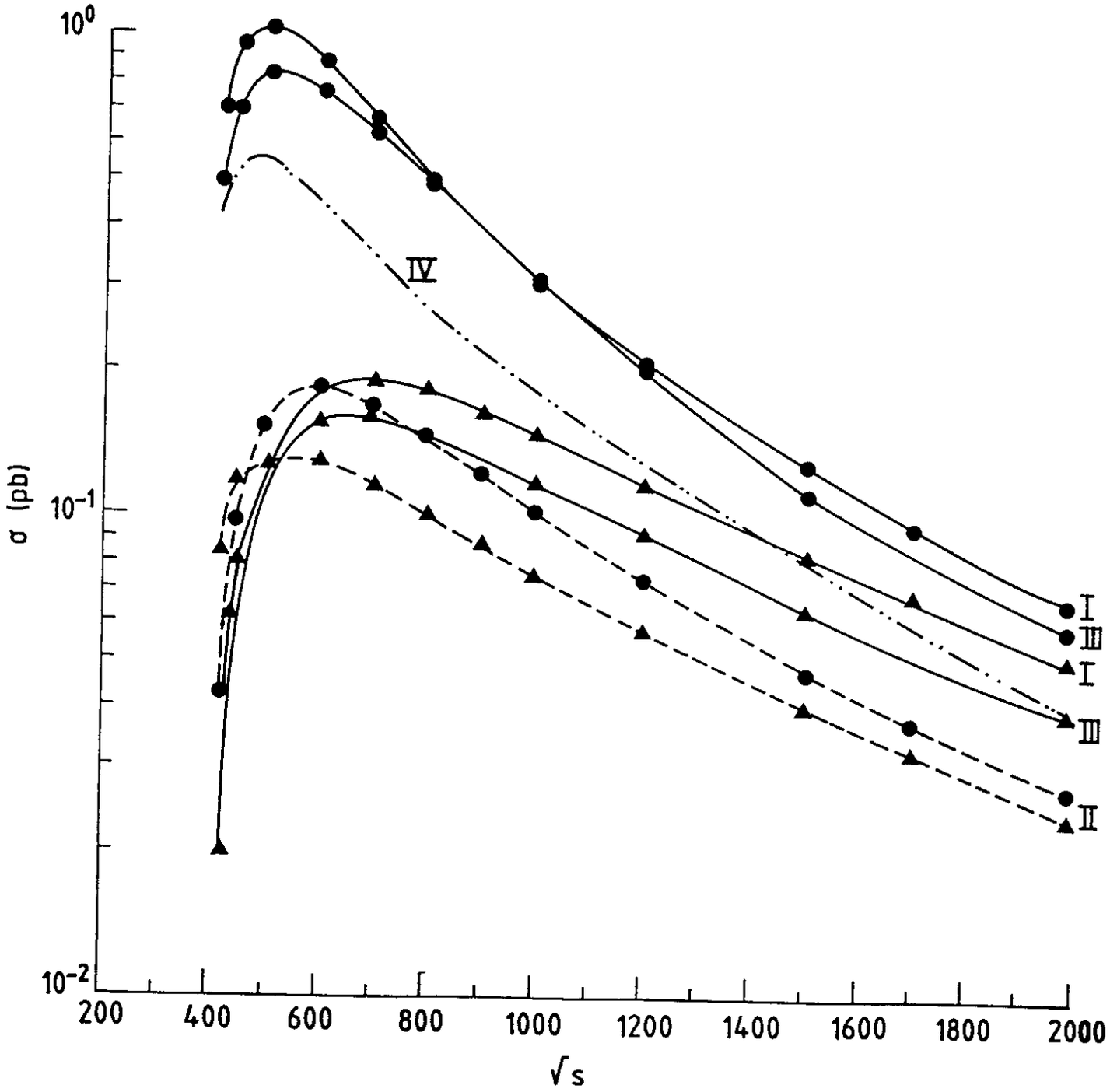
10^0
10^{-1}
10^{-2}
σ (pb)
200
400
600
800
1000
1200
1400
1600
1800
2000
√s
IV
I
III
I
III
II
II

FIG. 9b

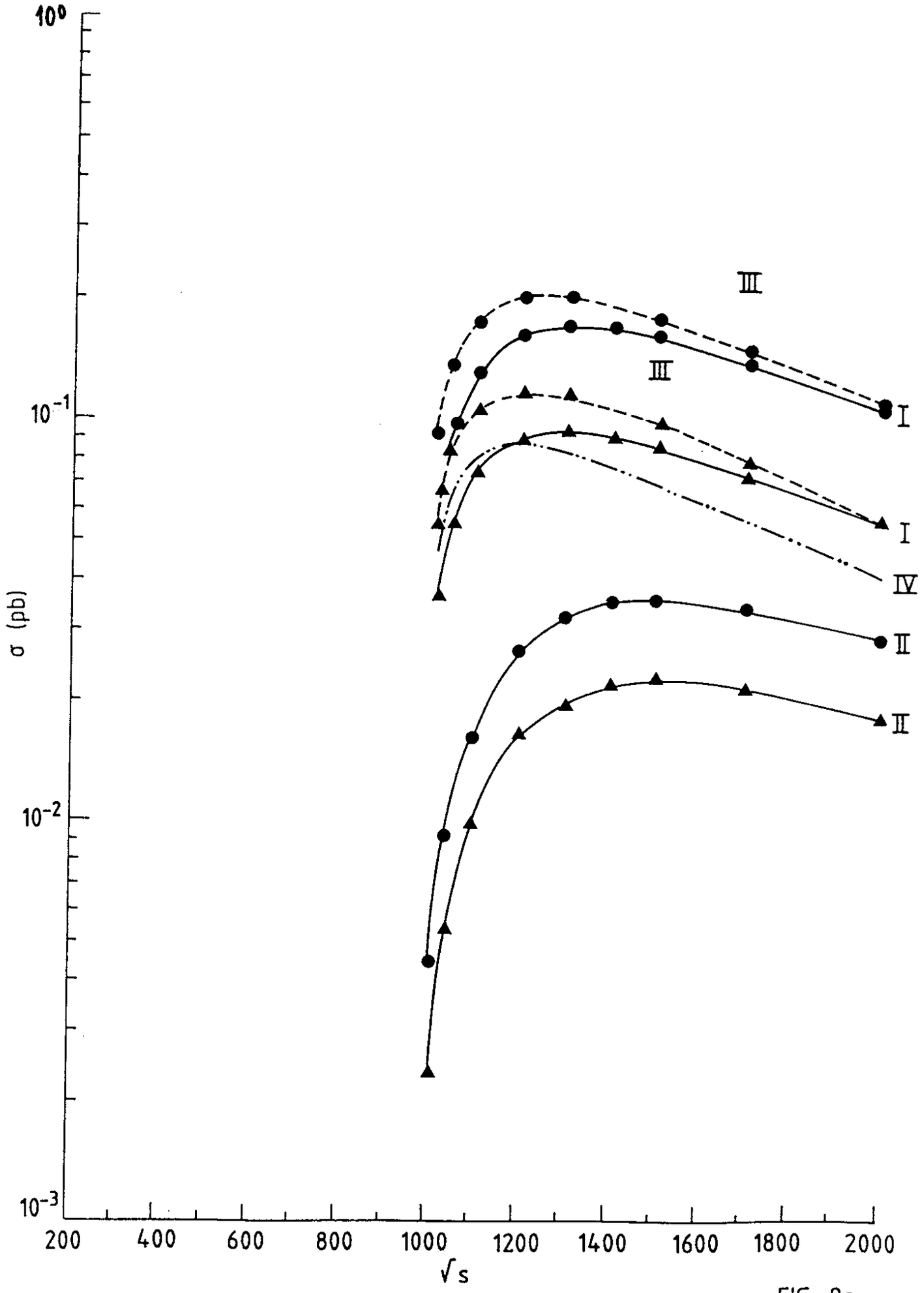
10⁰
10⁻¹
10⁻²
10⁻³
σ (pb)
200
400
600
800
1000
1200
1400
1600
1800
2000
√s
III
III
I
I
IV
II
II

FIG. 9c

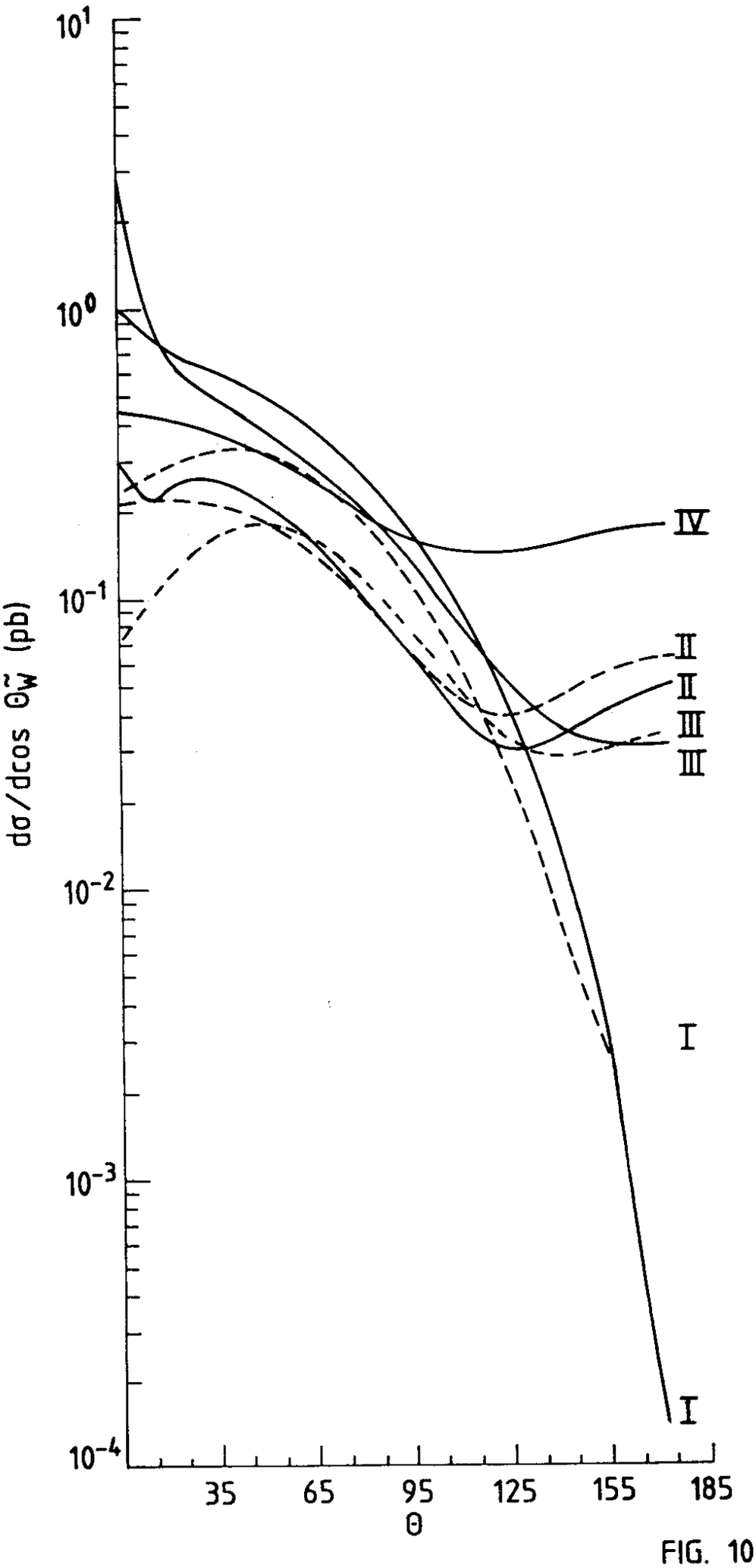
10^1
10^0
10^{-1}
10^{-2}
10^{-3}
10^{-4}
$d\sigma/d\cos\Theta_W^{\sim}$ (pb)
35
65
95
125
155
185
Θ
I
II
III
IV

FIG. 10

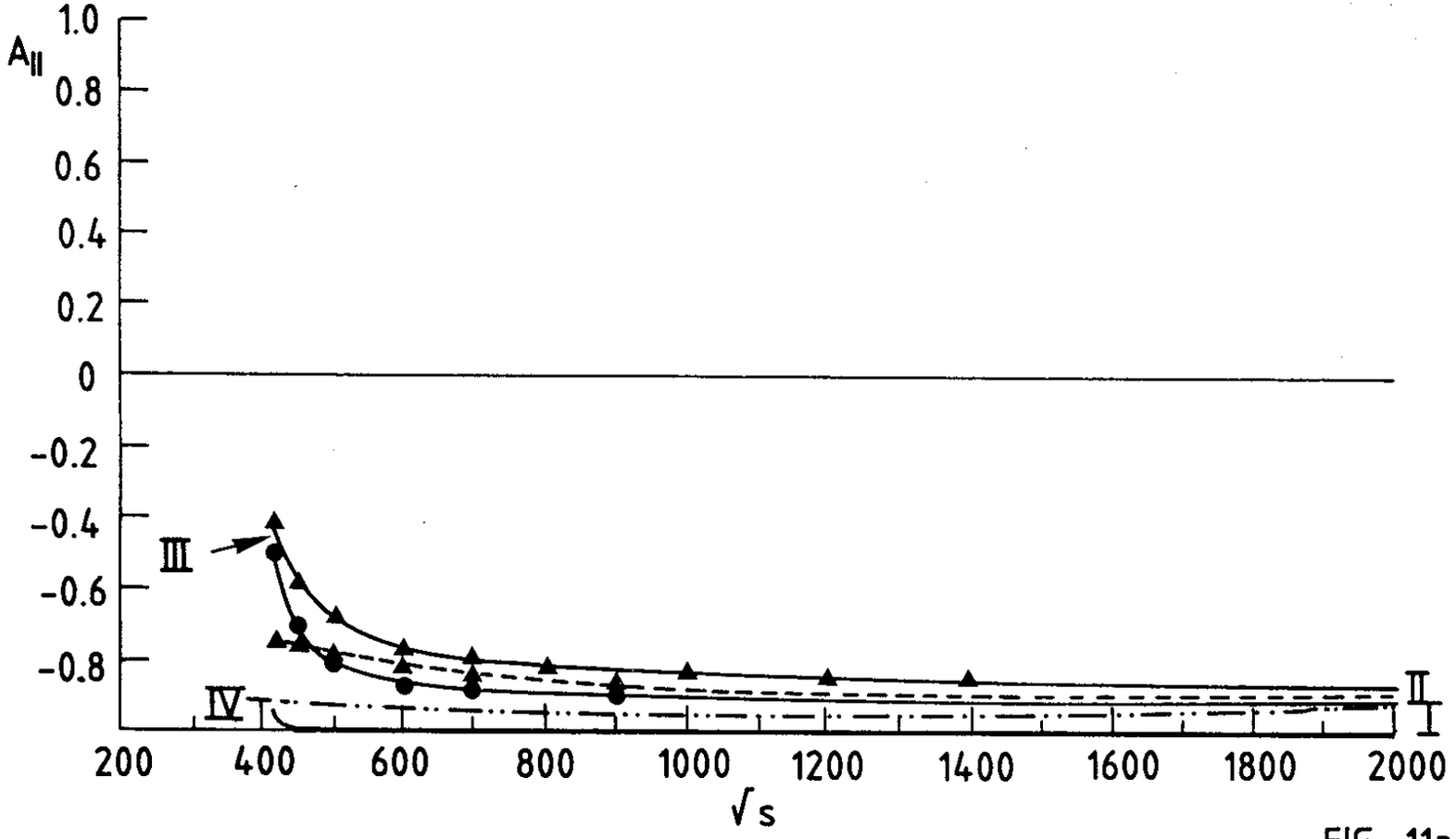
A_{II}
1.0
0.8
0.6
0.4
0.2
0
-0.2
-0.4
-0.6
-0.8
III
IV
II
I
200
400
600
800
1000
1200
1400
1600
1800
2000
$\sqrt{s}$

FIG. 11a

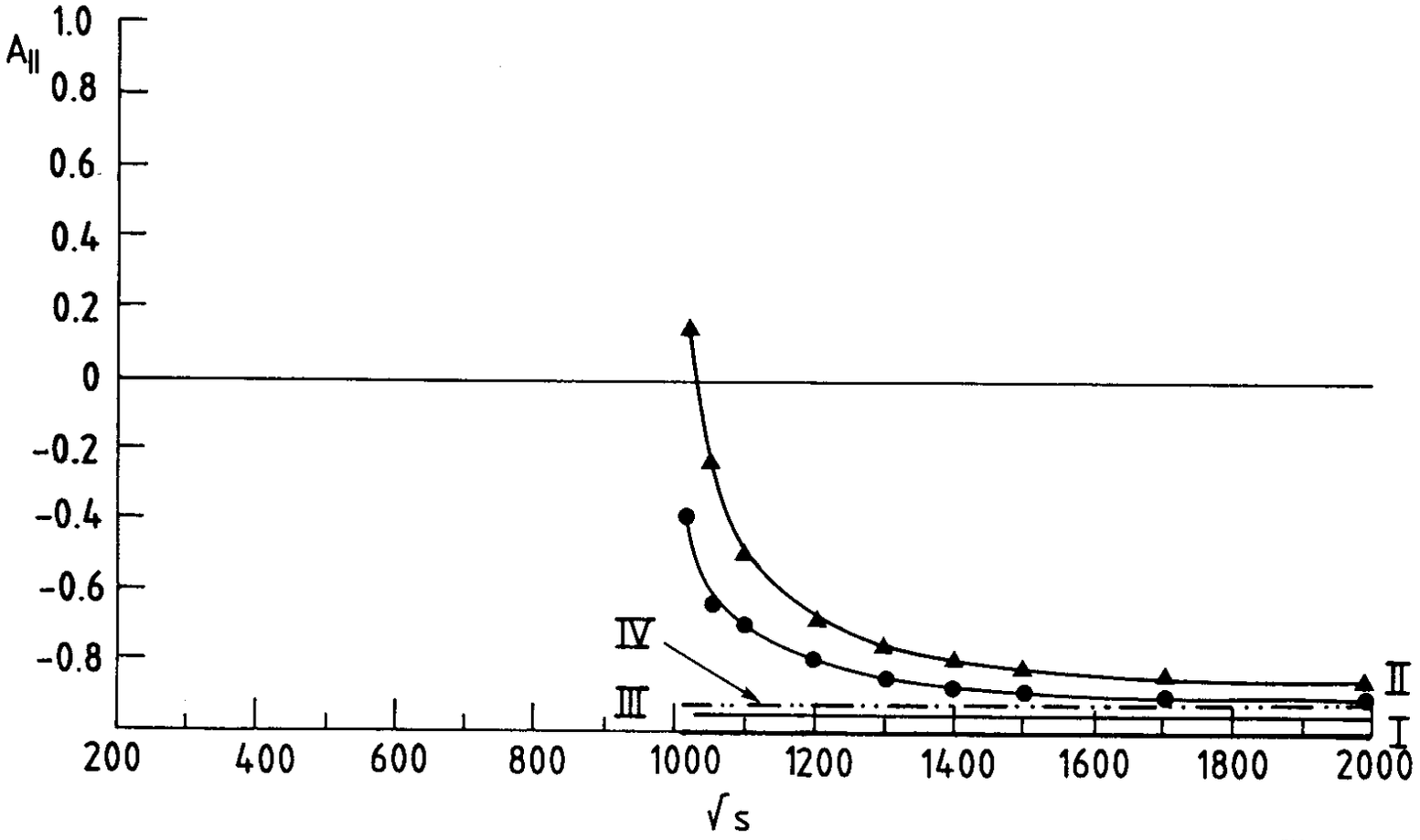
A_{II}
1.0
0.8
0.6
0.4
0.2
0
-0.2
-0.4
-0.6
-0.8
200
400
600
800
1000
1200
1400
1600
1800
2000
$\sqrt{s}$
IV
III
II
I

FIG. 11b

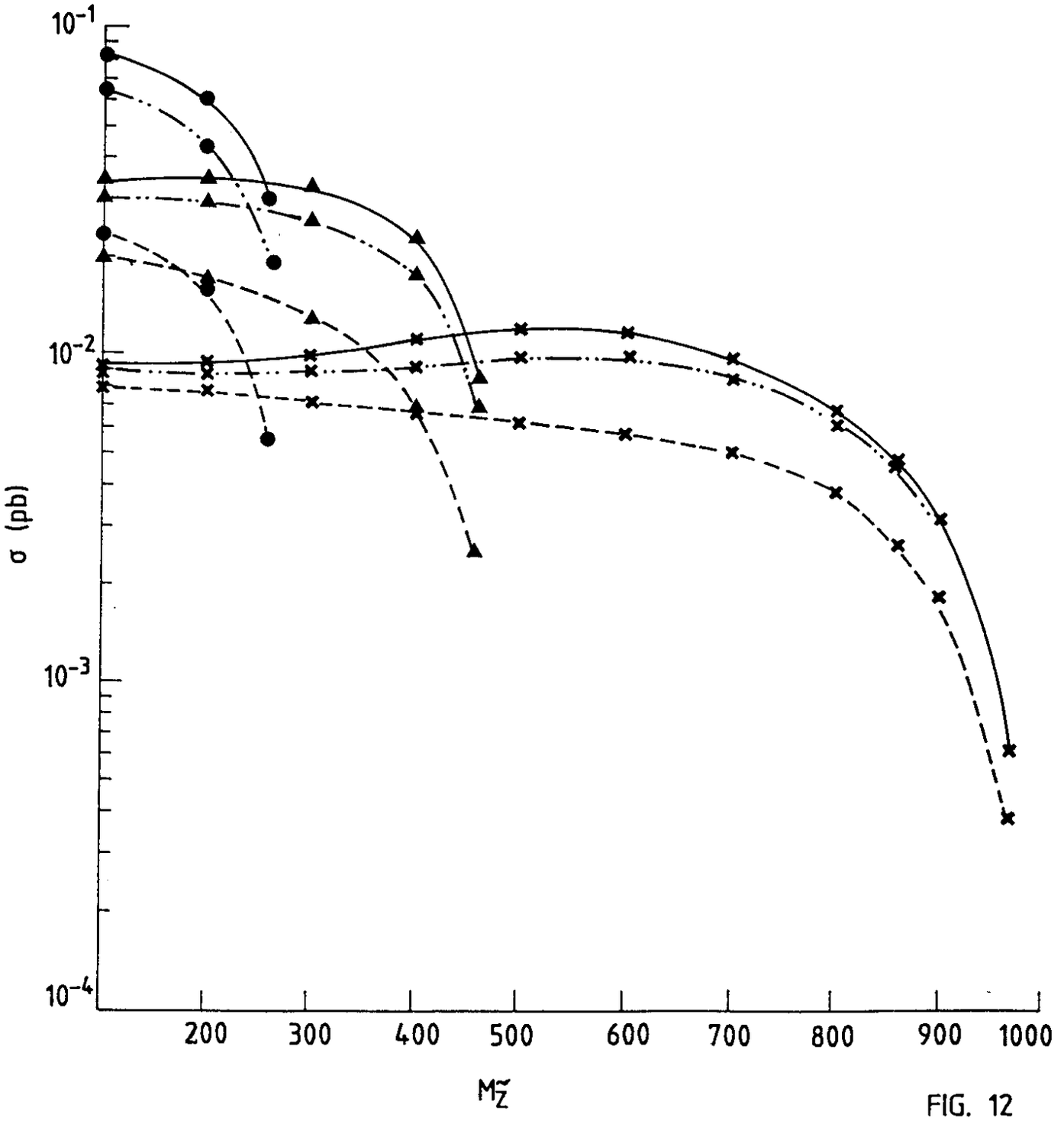
10^{-1}
10^{-2}
10^{-3}
10^{-4}
σ (pb)
200
300
400
500
600
700
800
900
1000
$M_{\tilde{Z}}$

FIG. 12

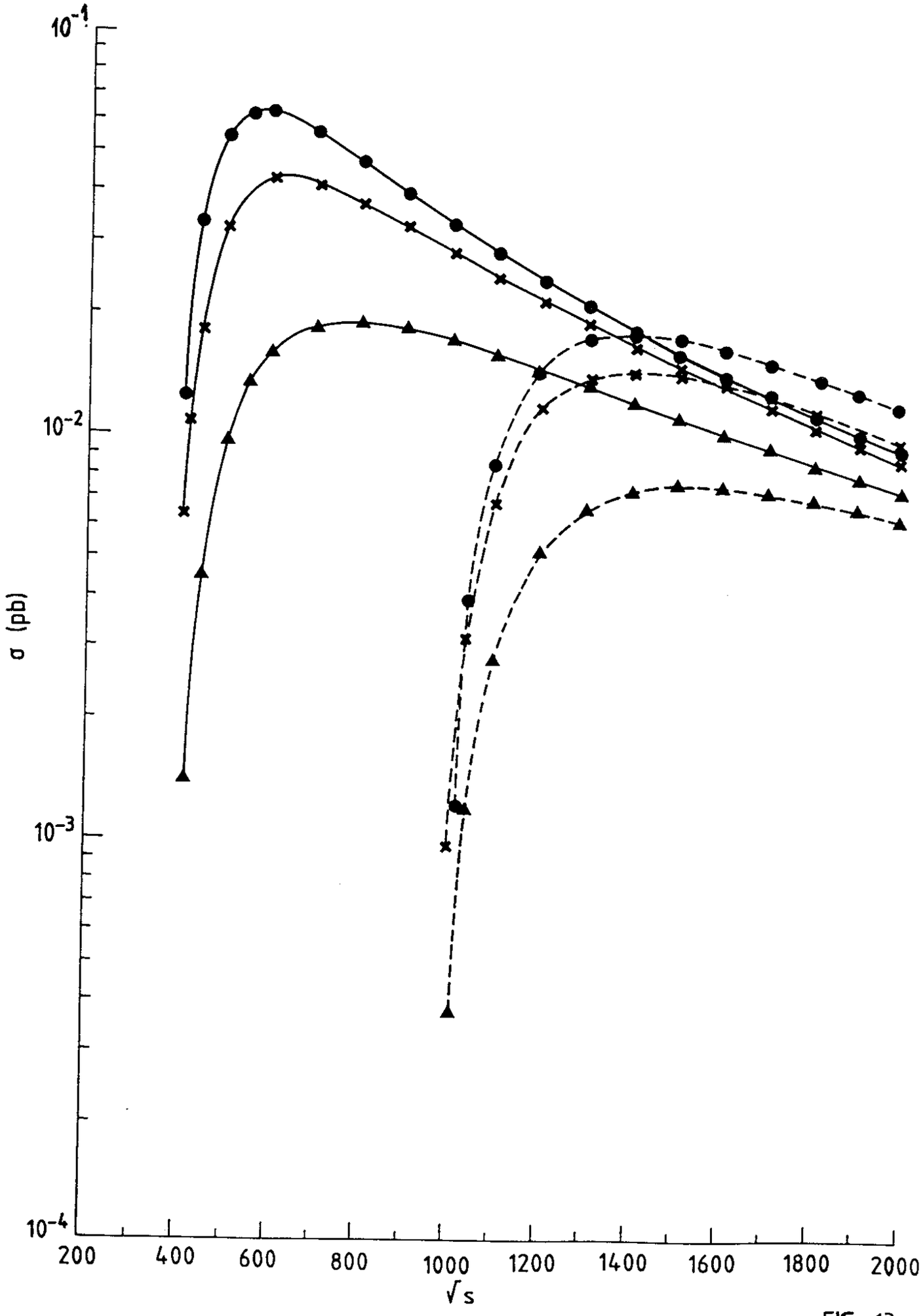
10^{-1}
10^{-2}
10^{-3}
10^{-4}
σ (pb)
200
400
600
800
1000
1200
1400
1600
1800
2000
√s

FIG. 13

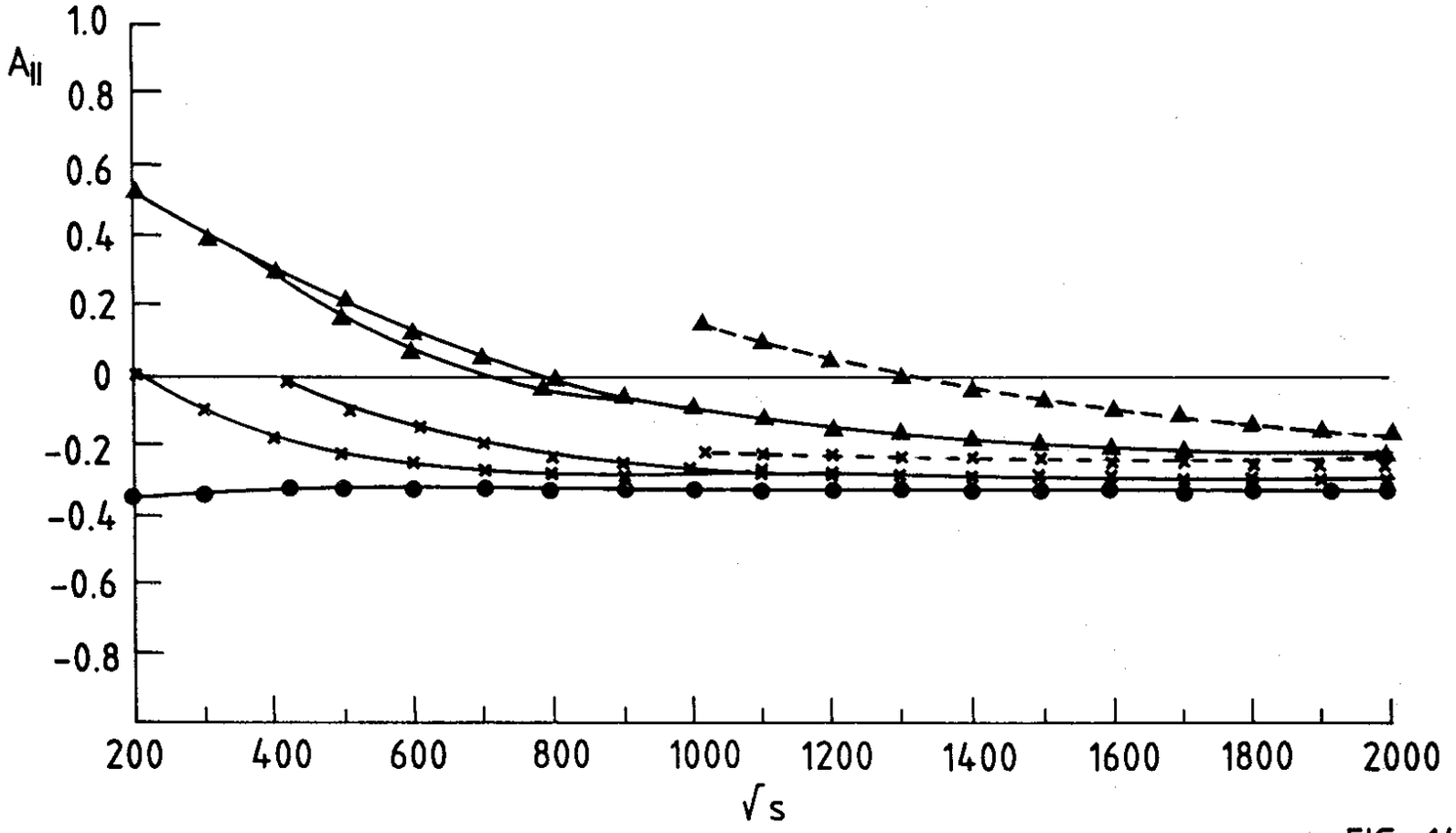
A_{II}
1.0
0.8
0.6
0.4
0.2
0
-0.2
-0.4
-0.6
-0.8
200
400
600
800
1000
1200
1400
1600
1800
2000
$\sqrt{s}$

FIG. 14

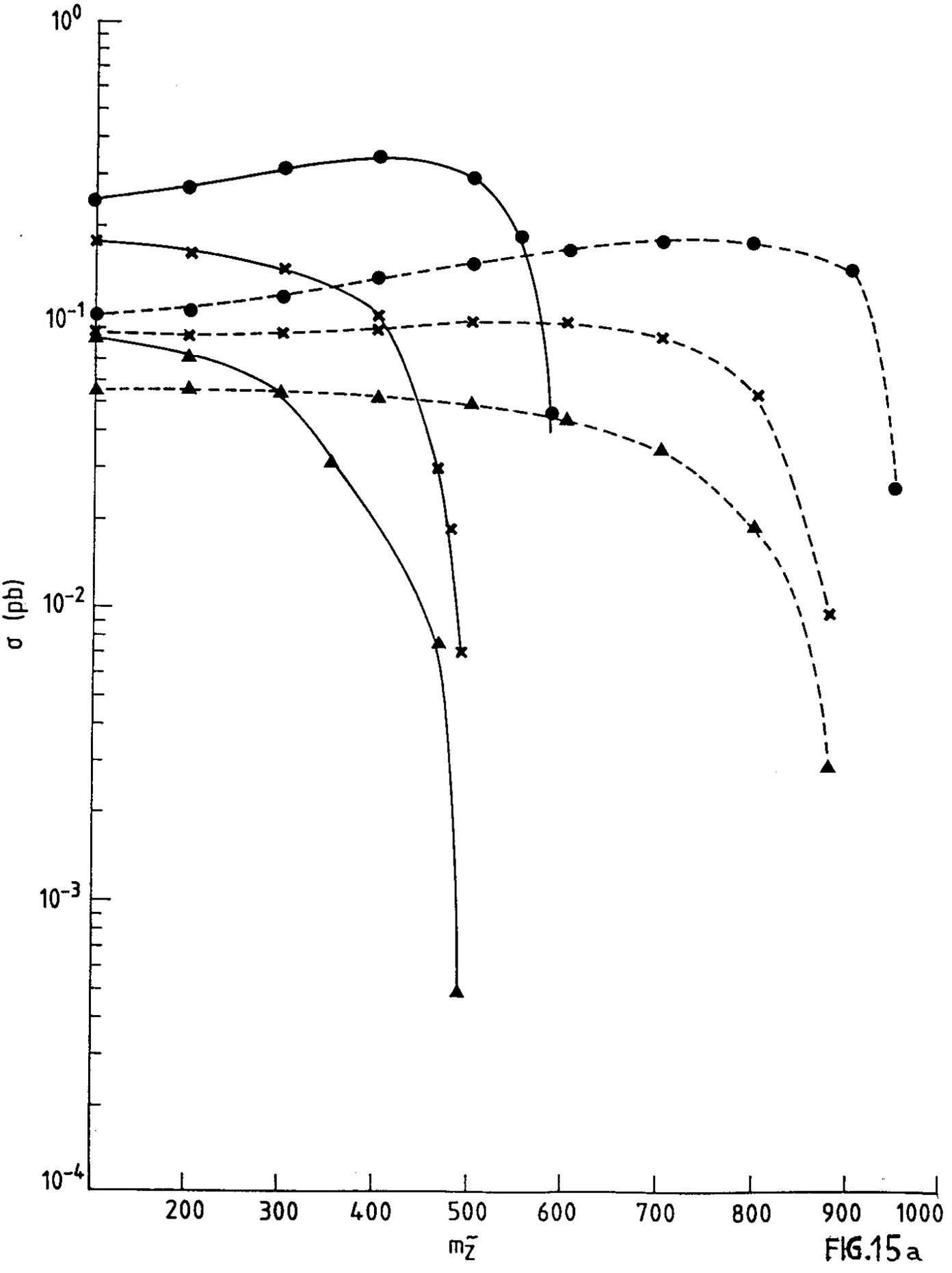
10^0
10^{-1}
10^{-2}
10^{-3}
10^{-4}
σ (pb)
200
300
400
500
600
700
800
900
1000
$m_{\tilde{Z}}$

FIG.15a

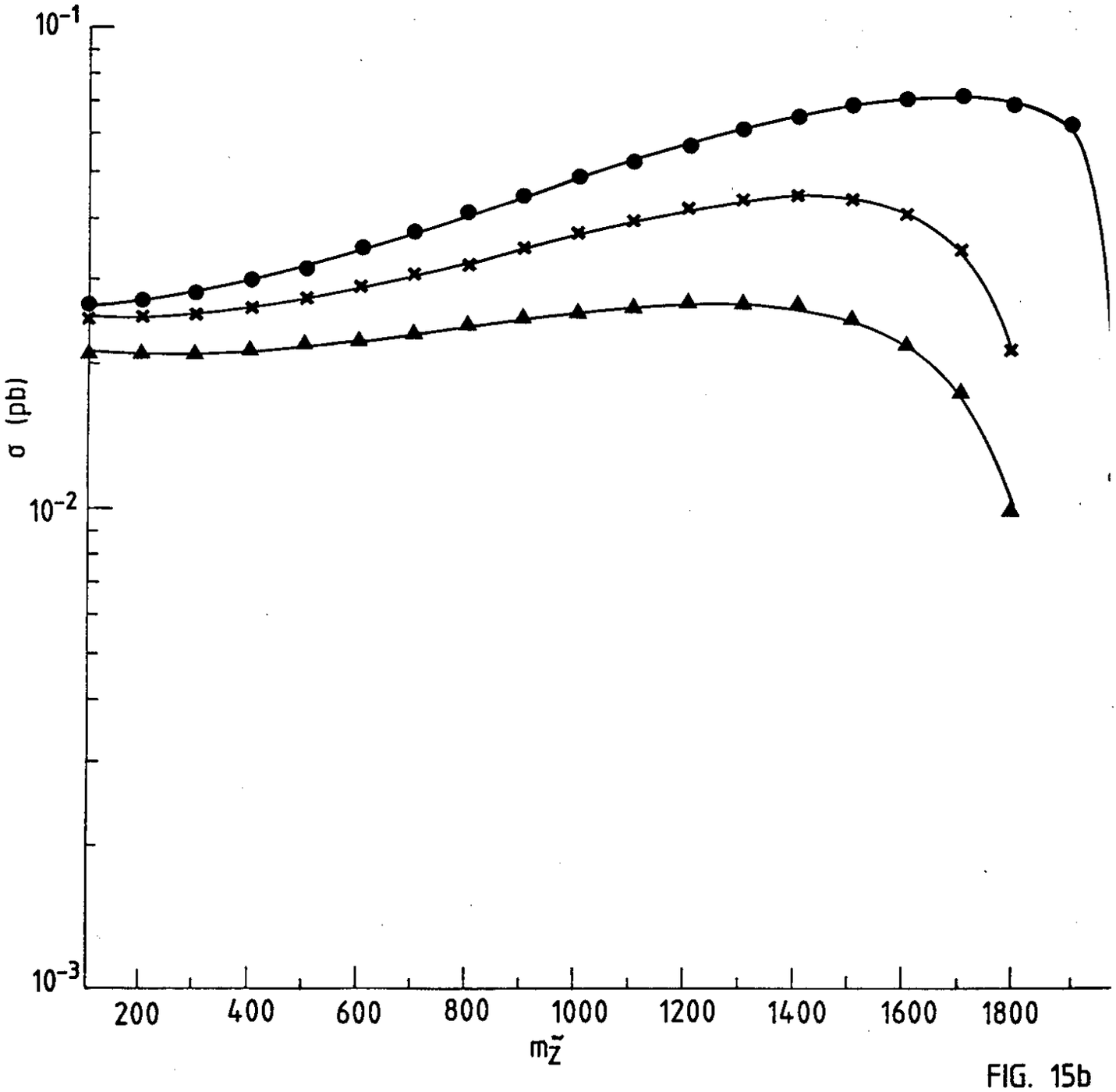
10^{-1}
10^{-2}
10^{-3}
σ (pb)
200
400
600
800
1000
1200
1400
1600
1800
$m_{\tilde{Z}}$

FIG. 15b

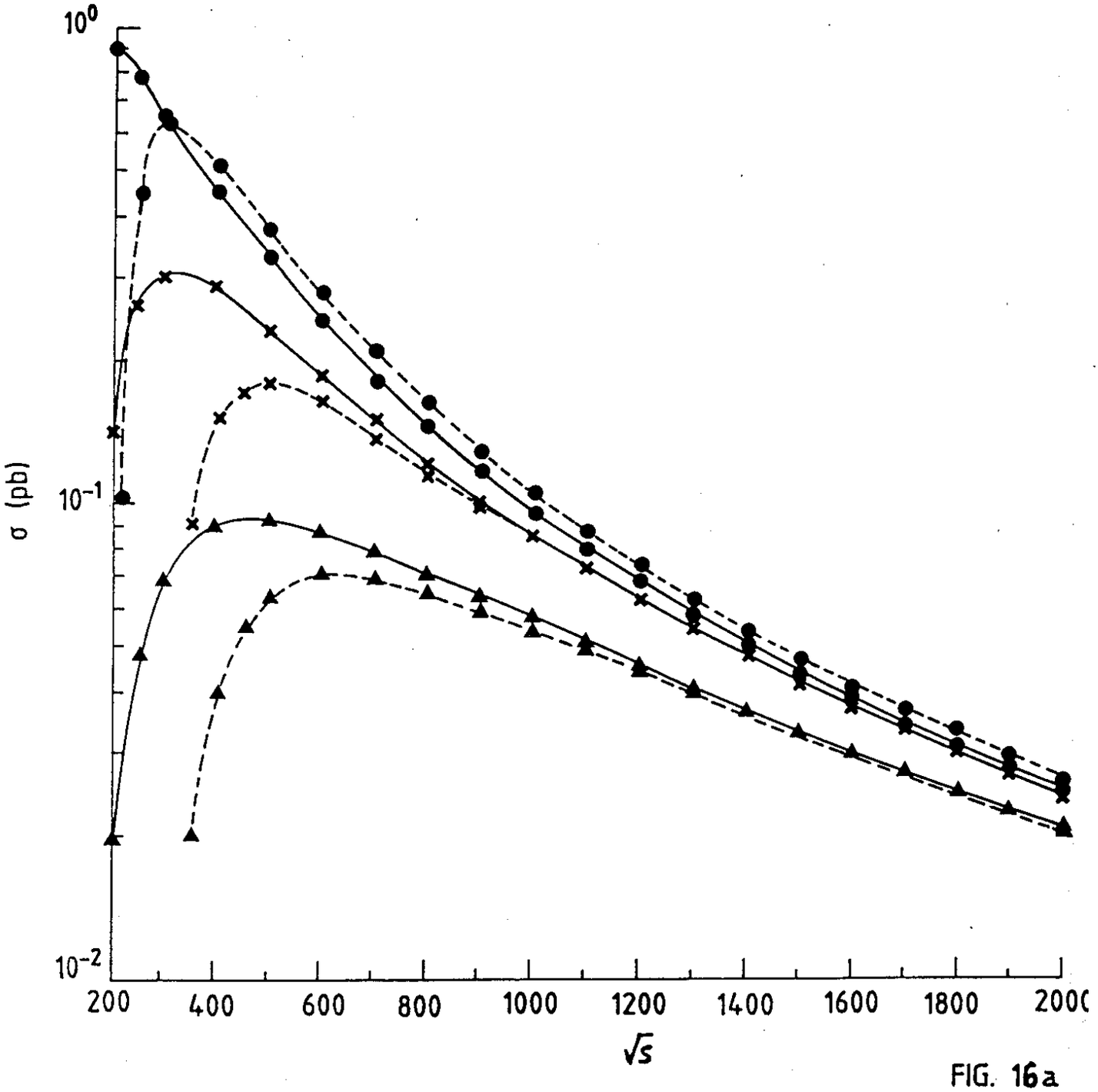
10^0
10^{-1}
10^{-2}
σ (pb)
200
400
600
800
1000
1200
1400
1600
1800
2000
$\sqrt{s}$

FIG. 16a

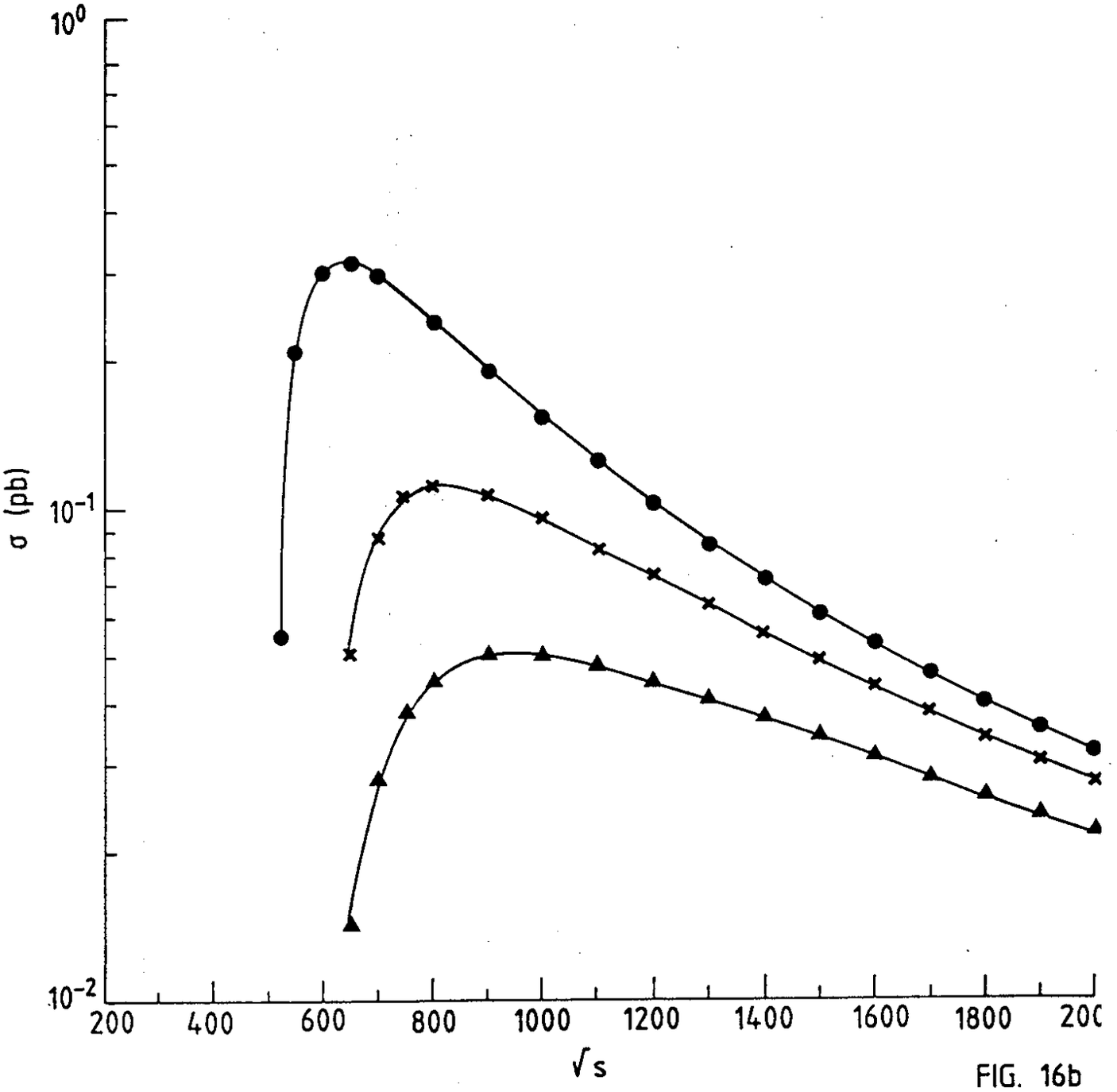

FIG. 16b

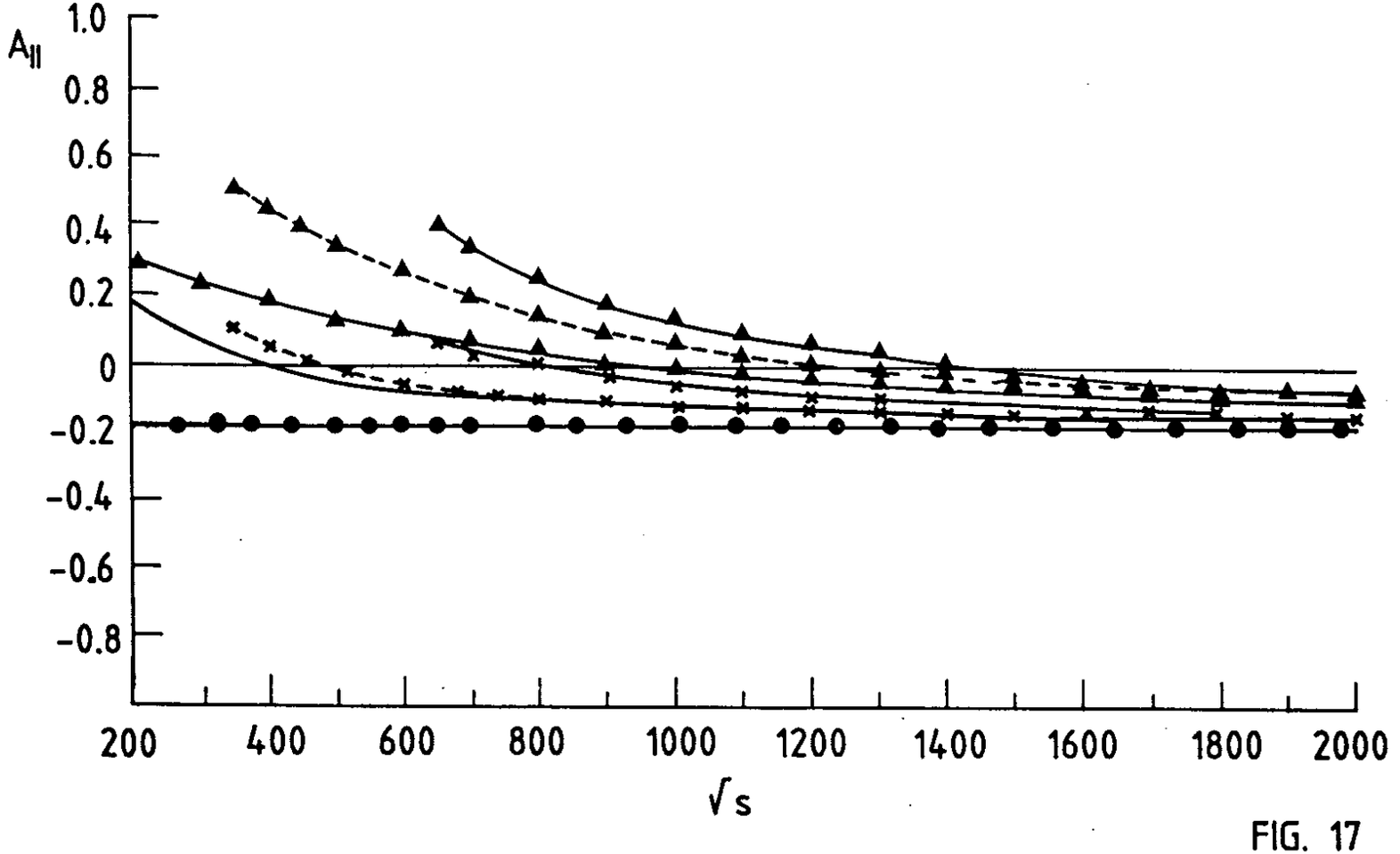
A_{II}
1.0
0.8
0.6
0.4
0.2
0
-0.2
-0.4
-0.6
-0.8
200
400
600
800
1000
1200
1400
1600
1800
2000
$\sqrt{s}$

FIG. 17

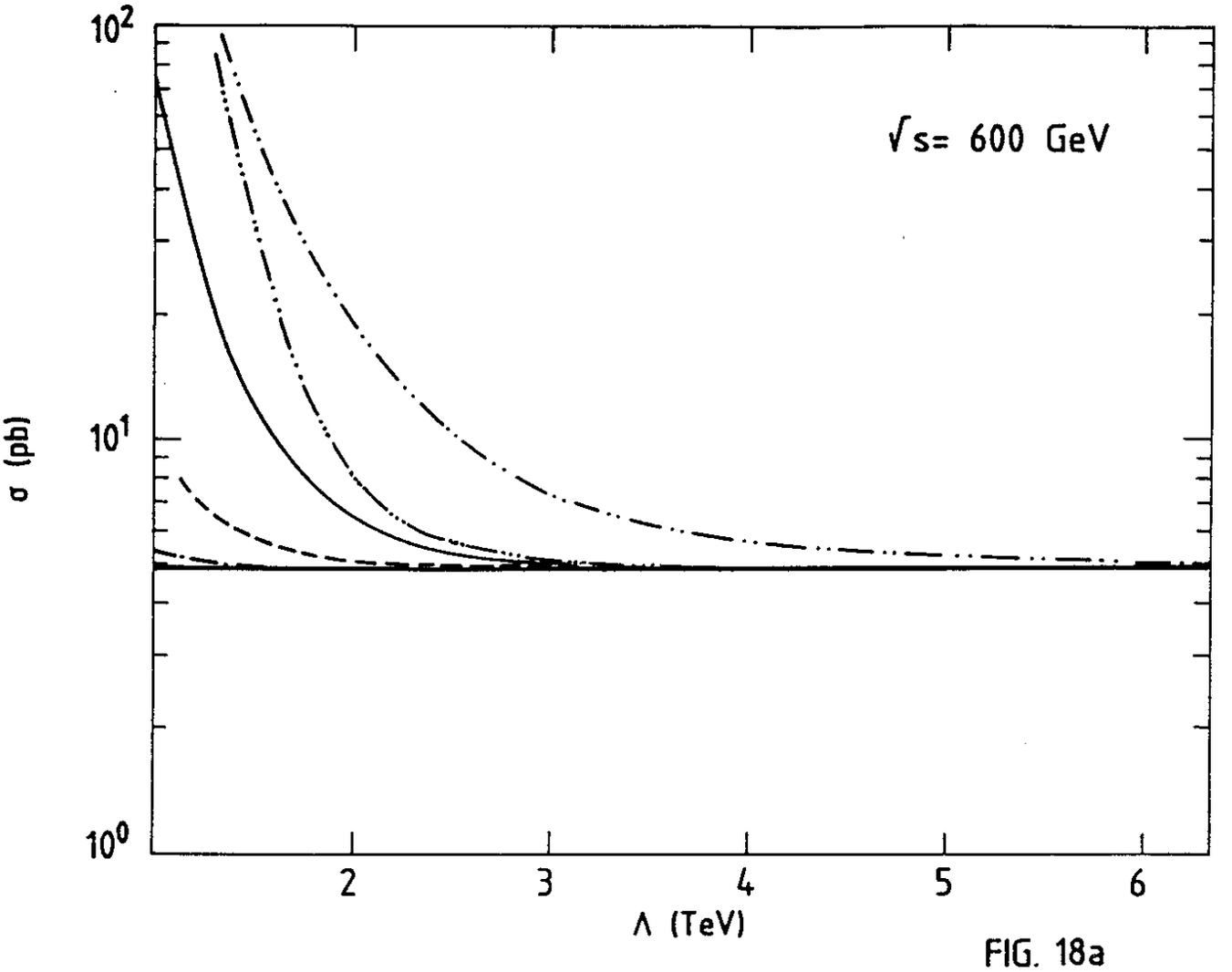

FIG. 18a

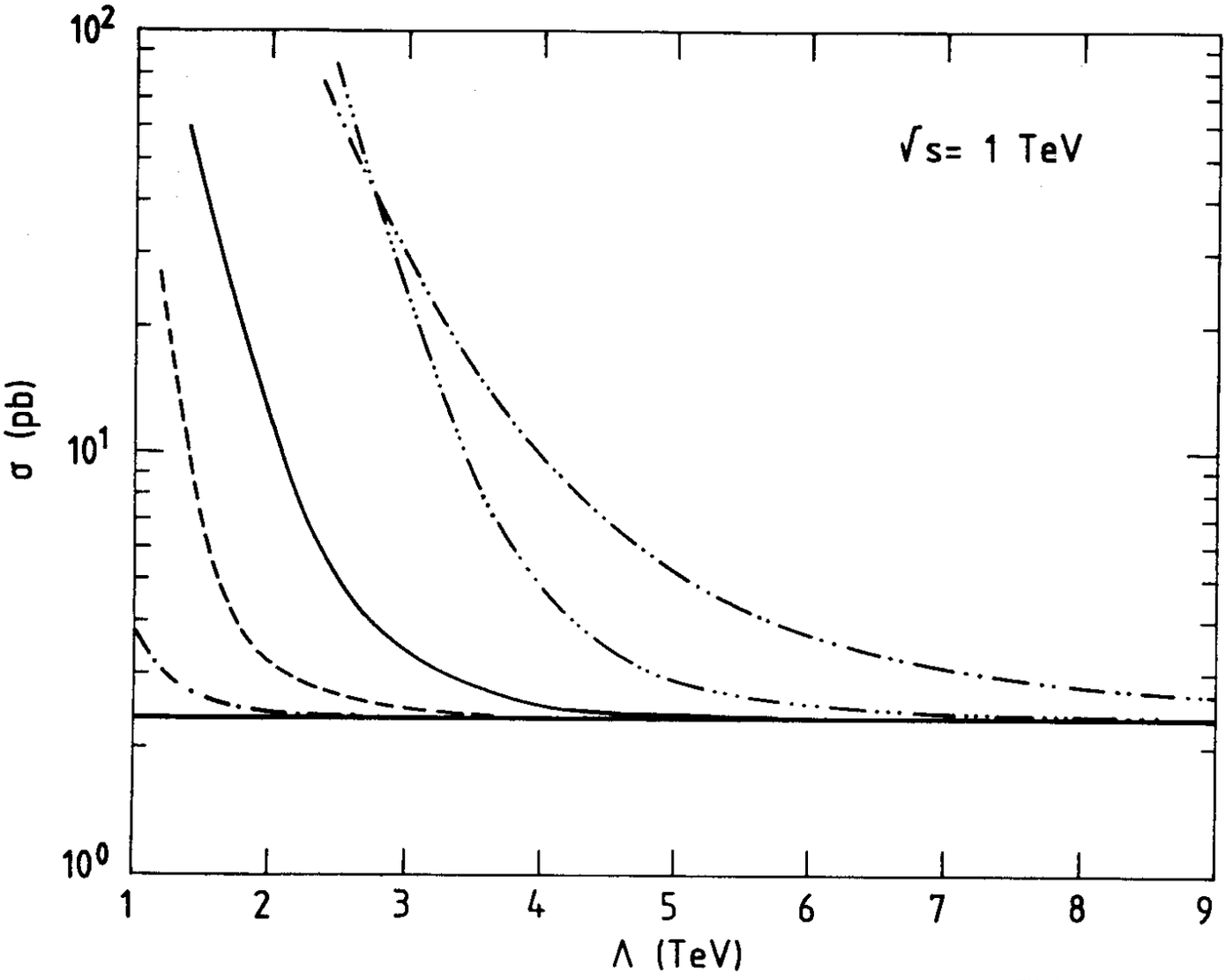

FIG. 18b

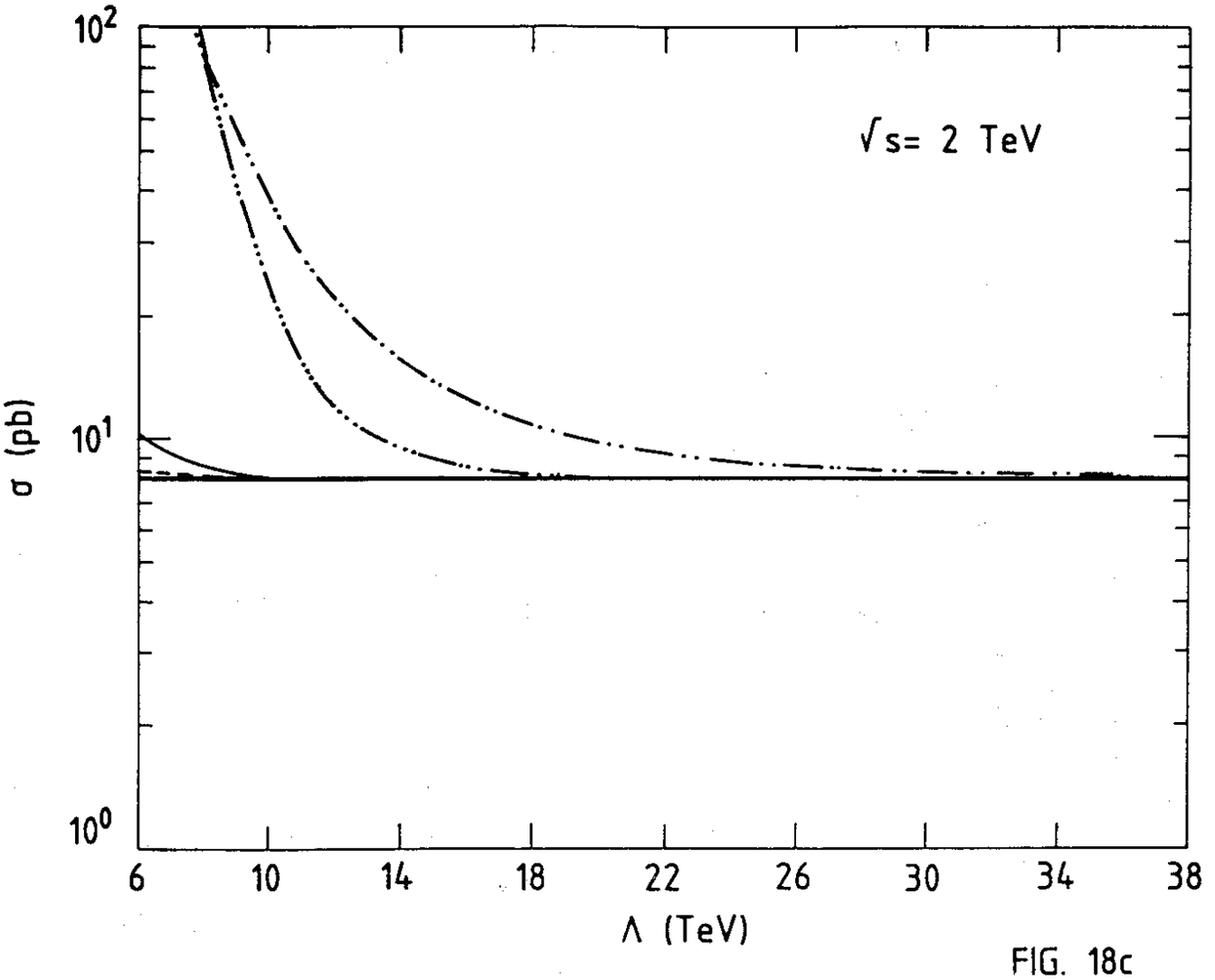

FIG. 18c

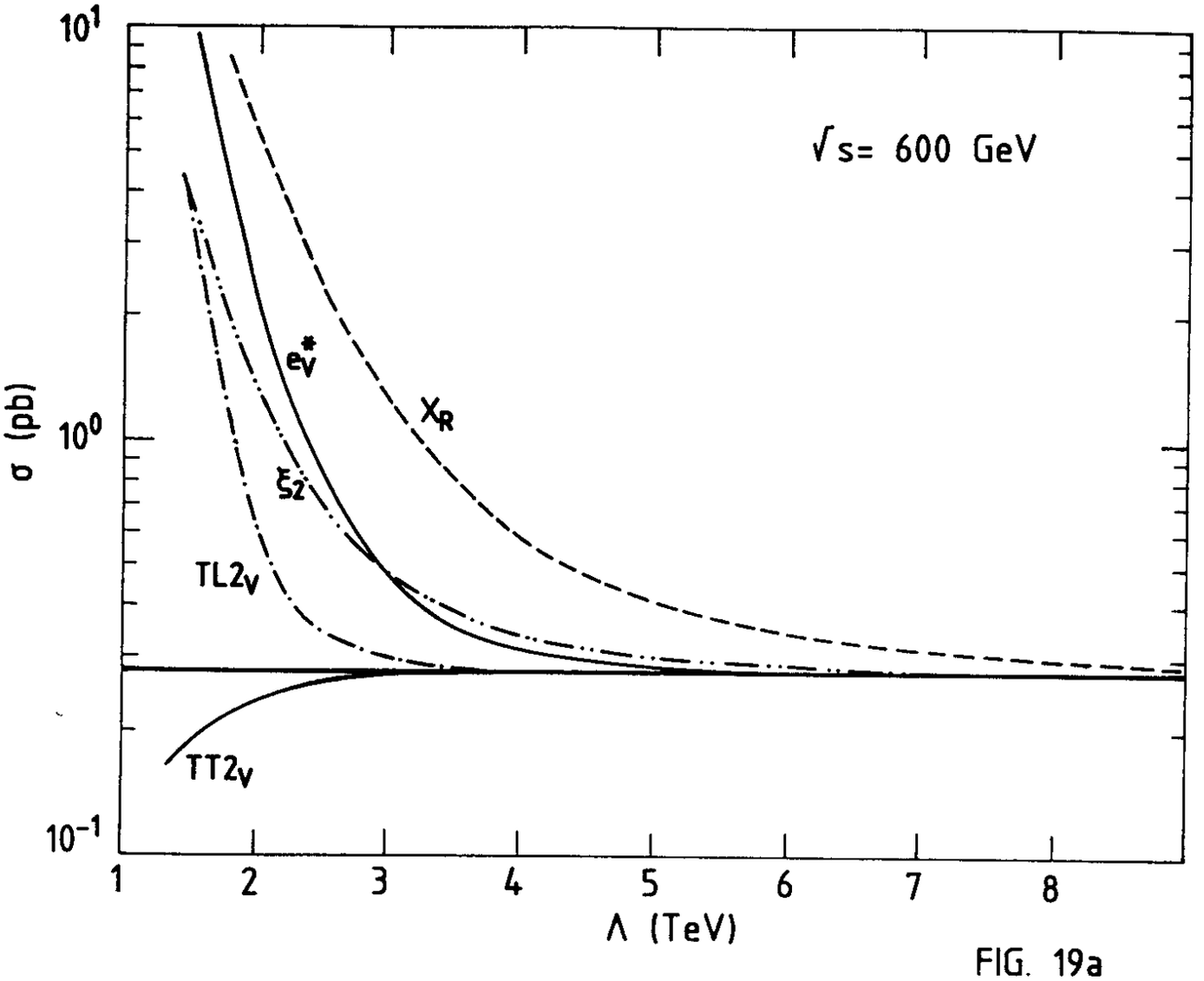

FIG. 19a

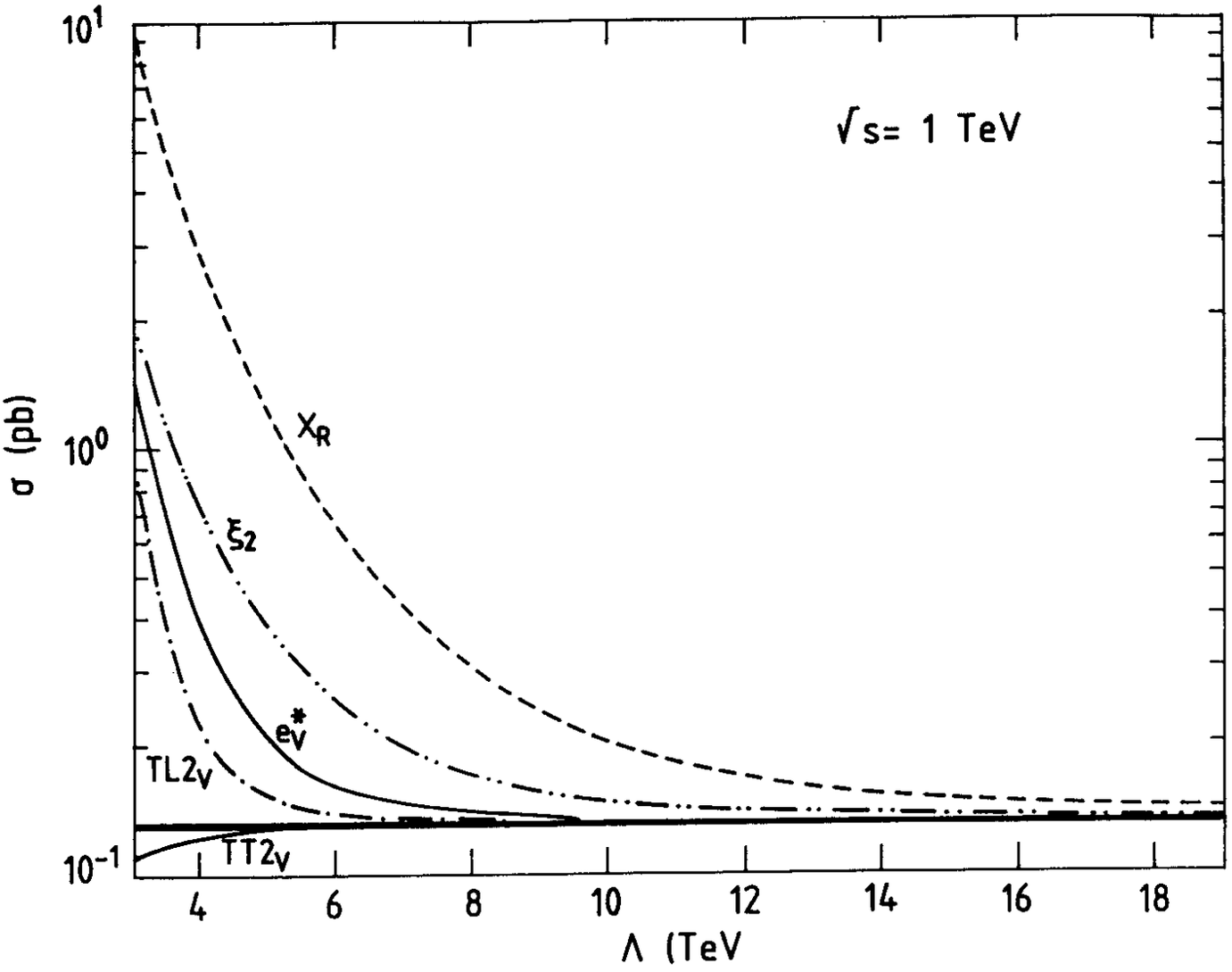

FIG. 19b

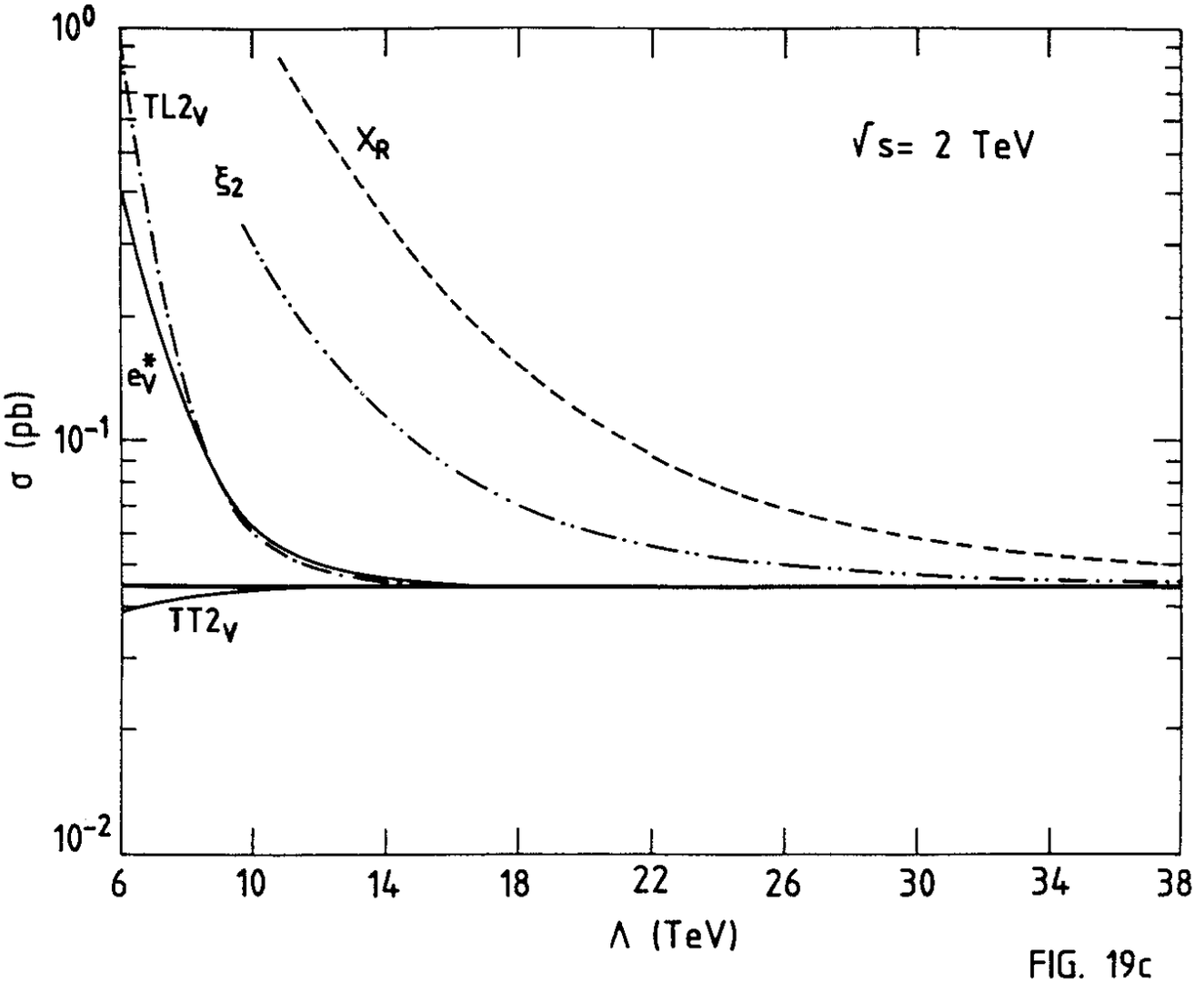
10^0
10^{-1}
10^{-2}
σ (pb)
$TL2_V$
X_R
ξ_2
e_V^*
$TT2_V$
$\sqrt{s}$= 2 TeV
6
10
14
18
22
26
30
34
38
Λ (TeV)

FIG. 19c

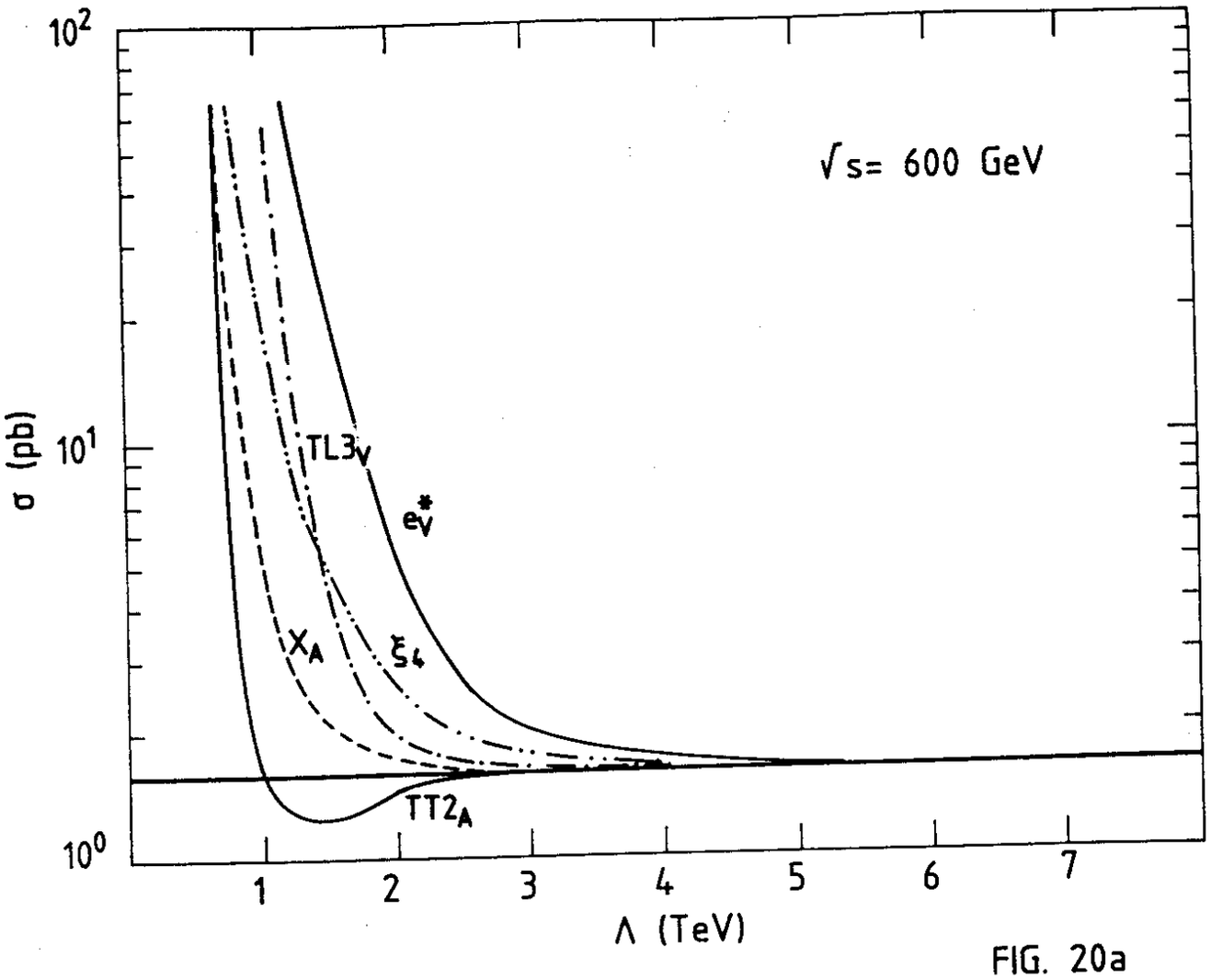

FIG. 20a

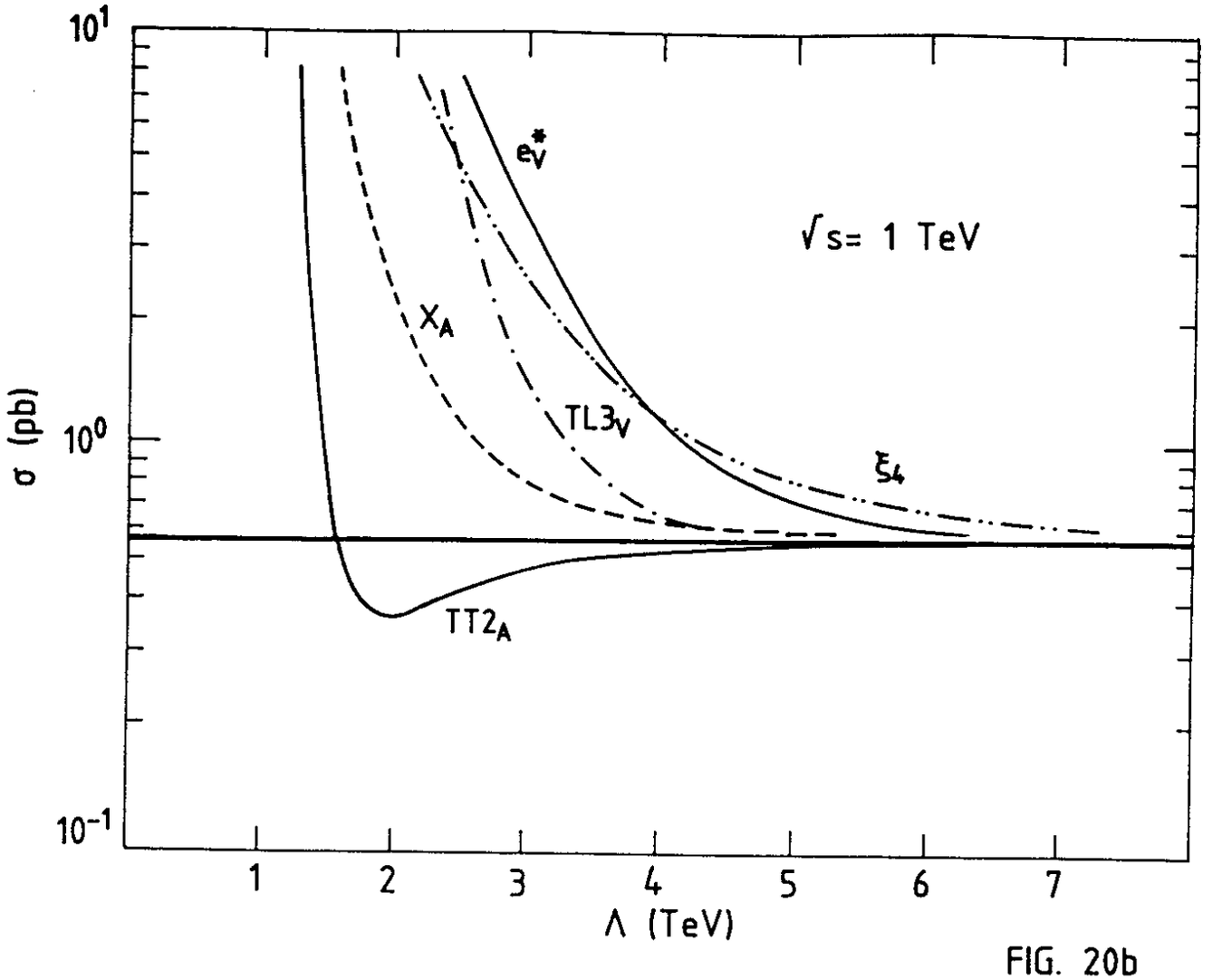

FIG. 20b

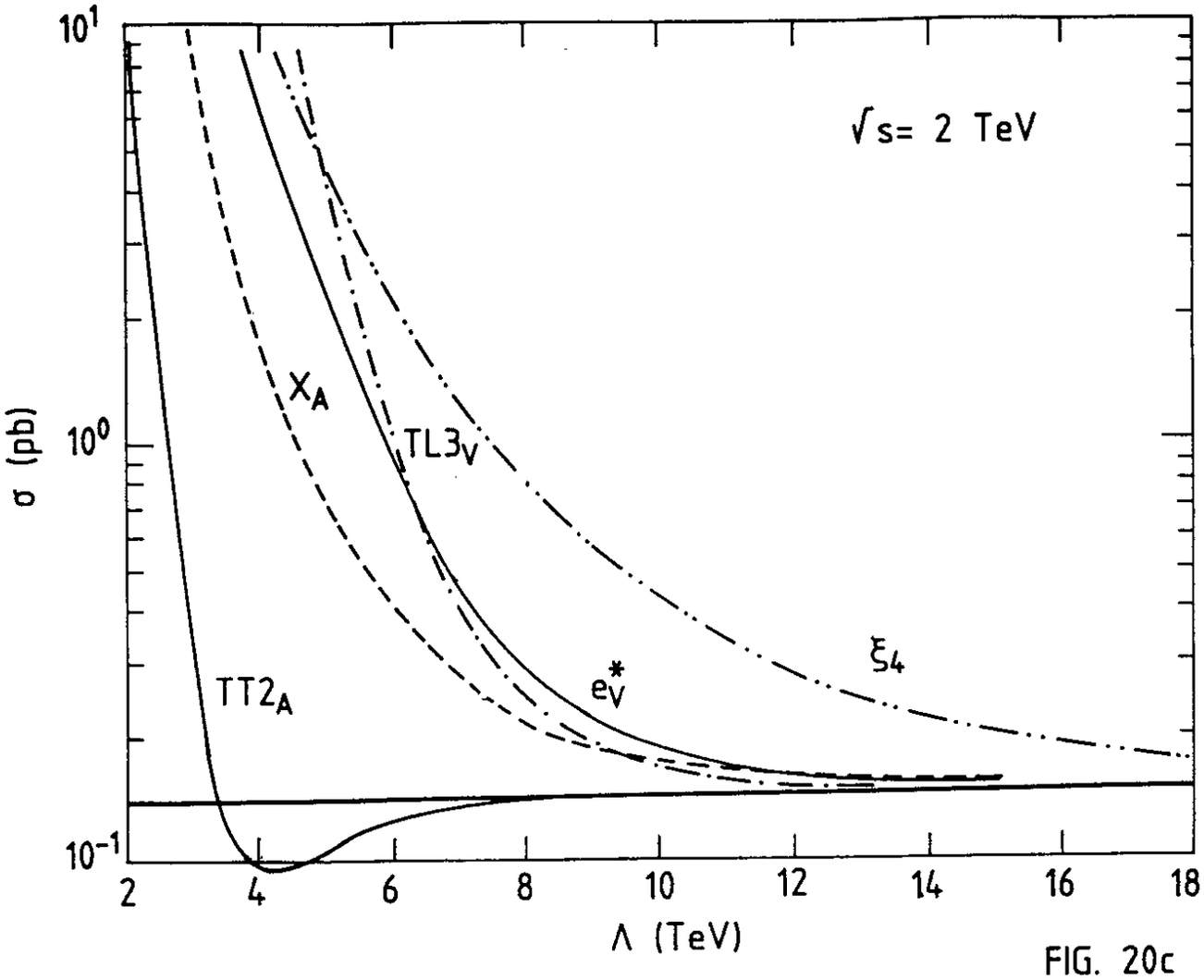
10^1
10^0
10^{-1}
σ (pb)
√s= 2 TeV
X_A
$TL3_V$
$TT2_A$
e_V^*
ξ_4
2
4
6
8
10
12
14
16
18
Λ (TeV)

FIG. 20c

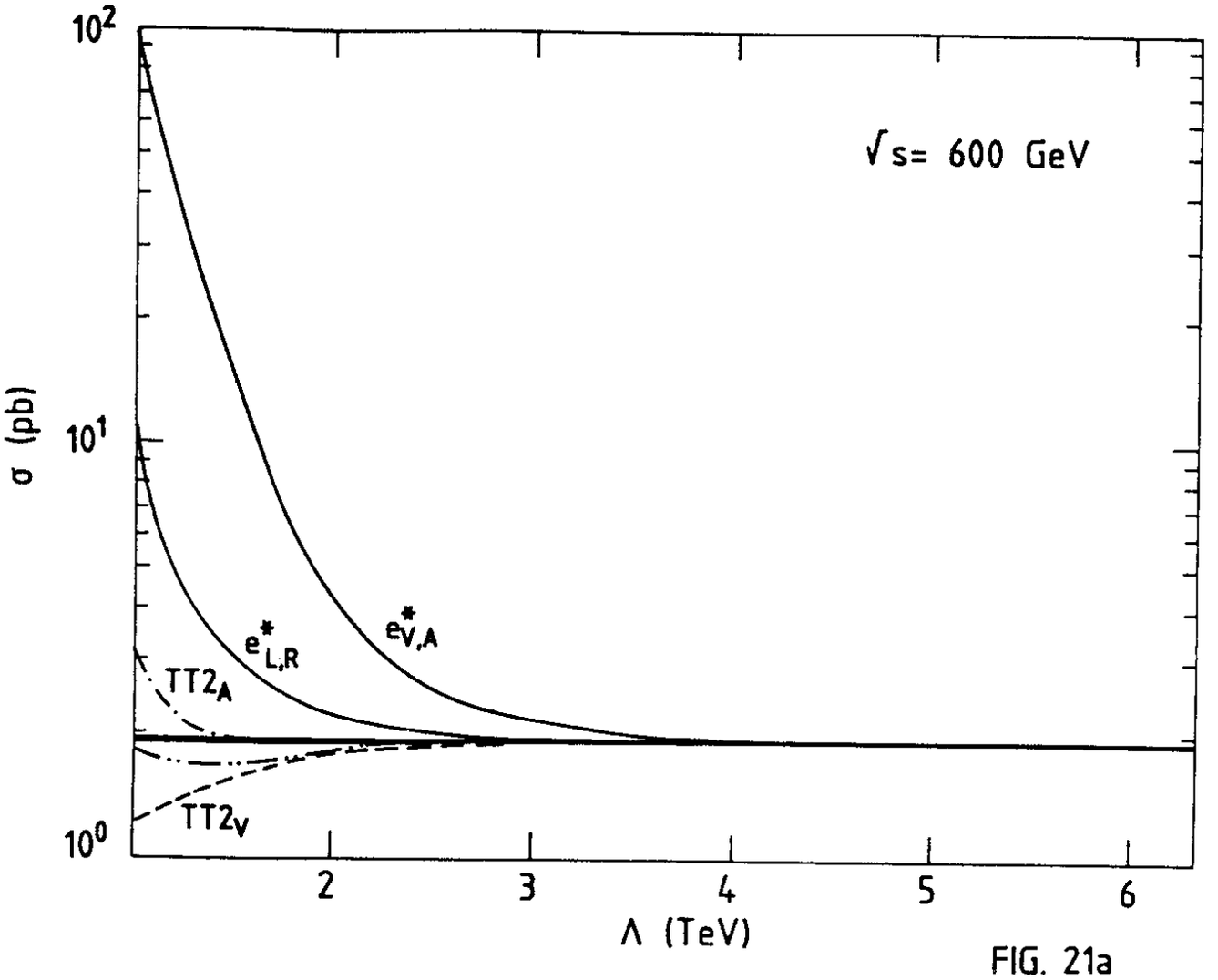

FIG. 21a

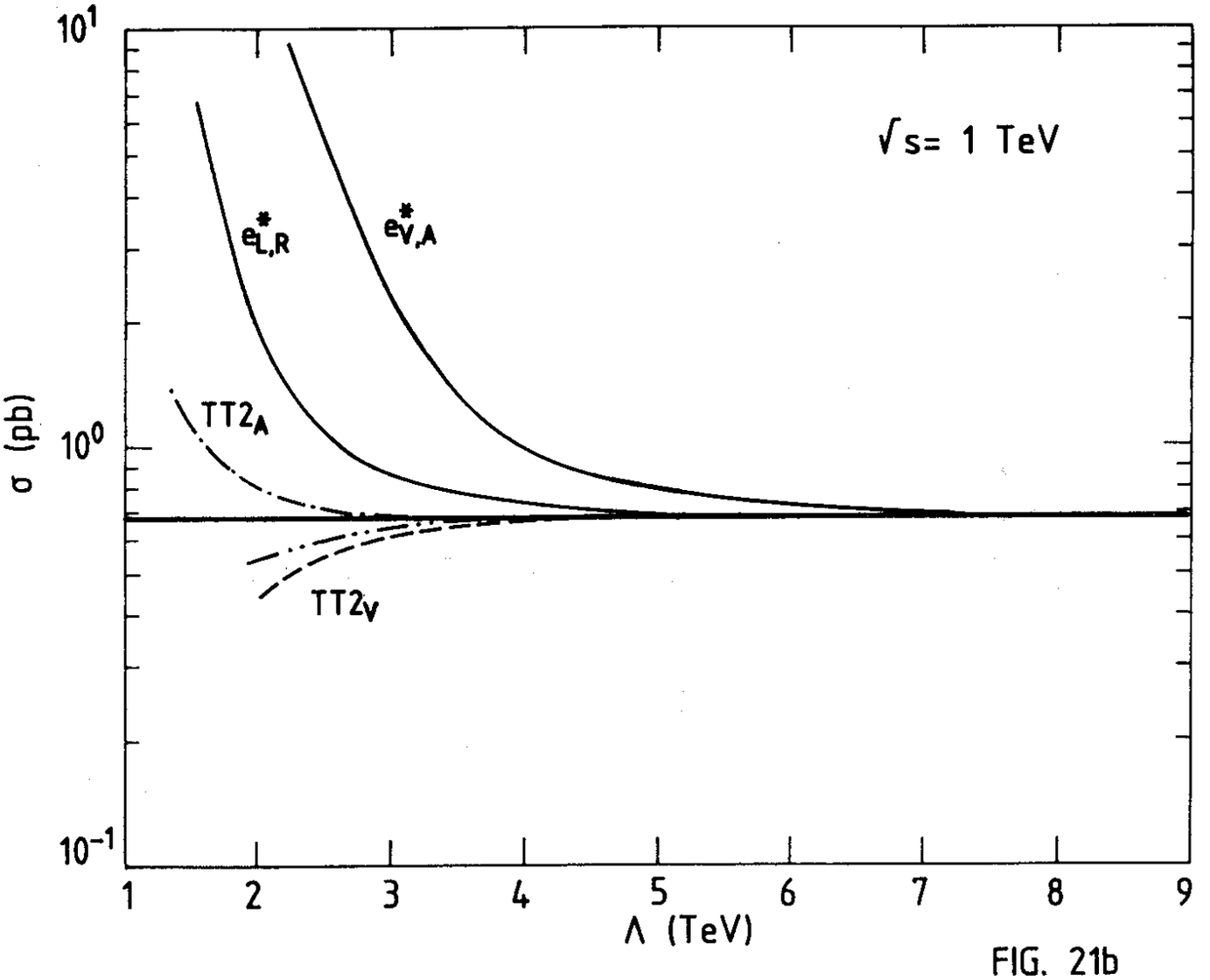

FIG. 21b

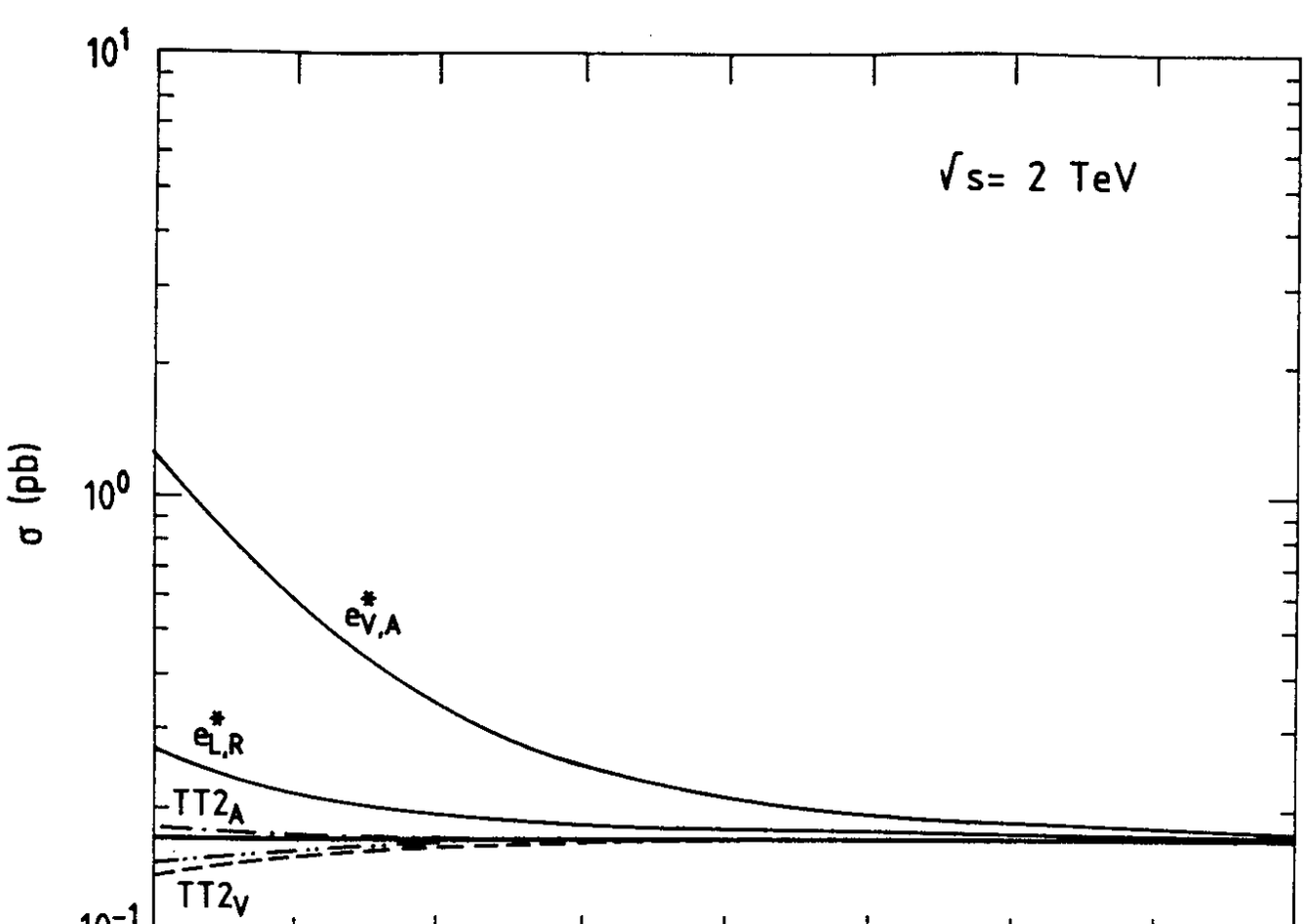

FIG. 21c

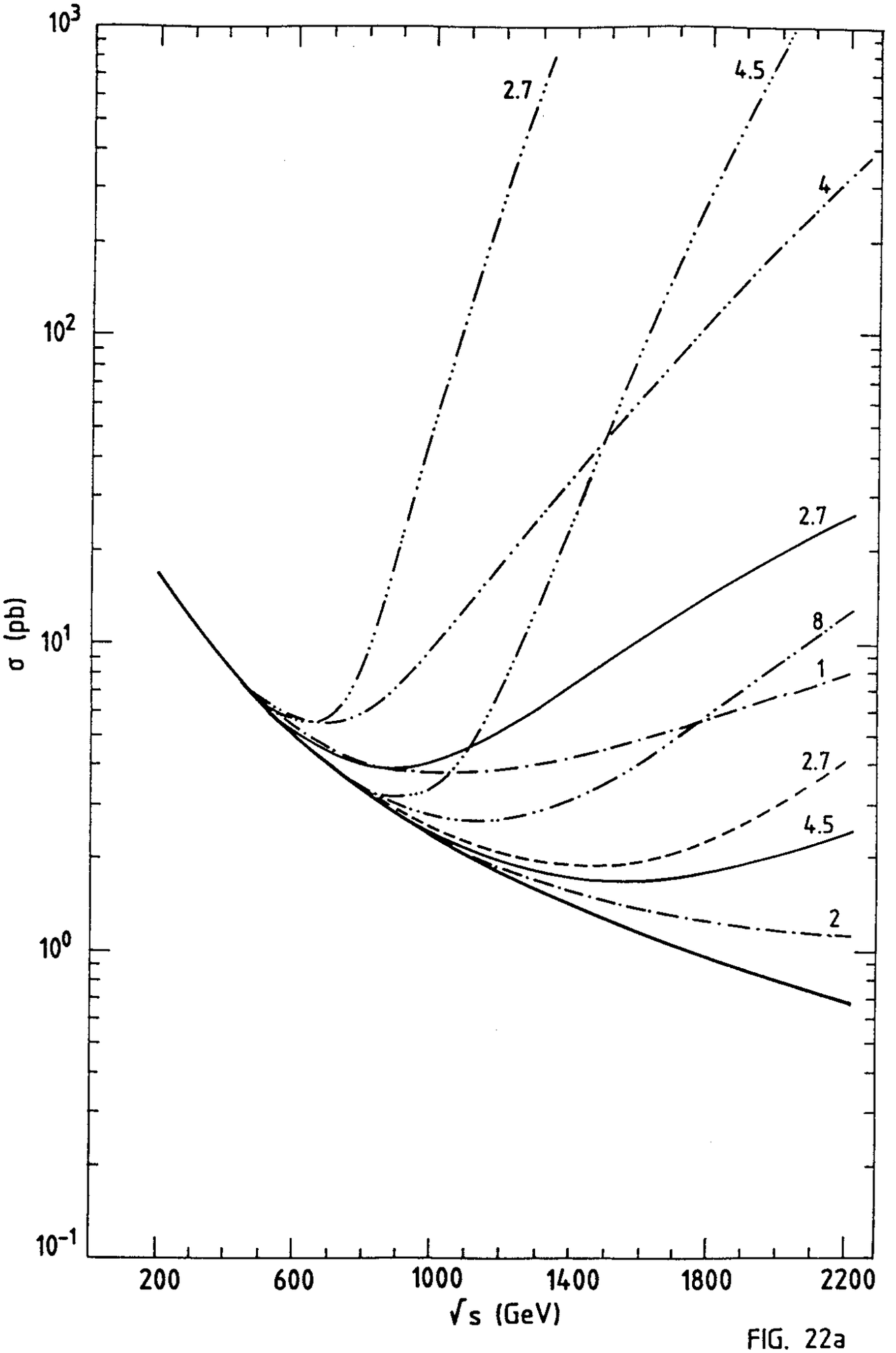
10^3
10^2
10^1
10^0
10^{-1}
σ (pb)
2.7
4.5
4
2.7
8
1
2.7
4.5
2
200
600
1000
1400
1800
2200
√s (GeV)

FIG. 22a

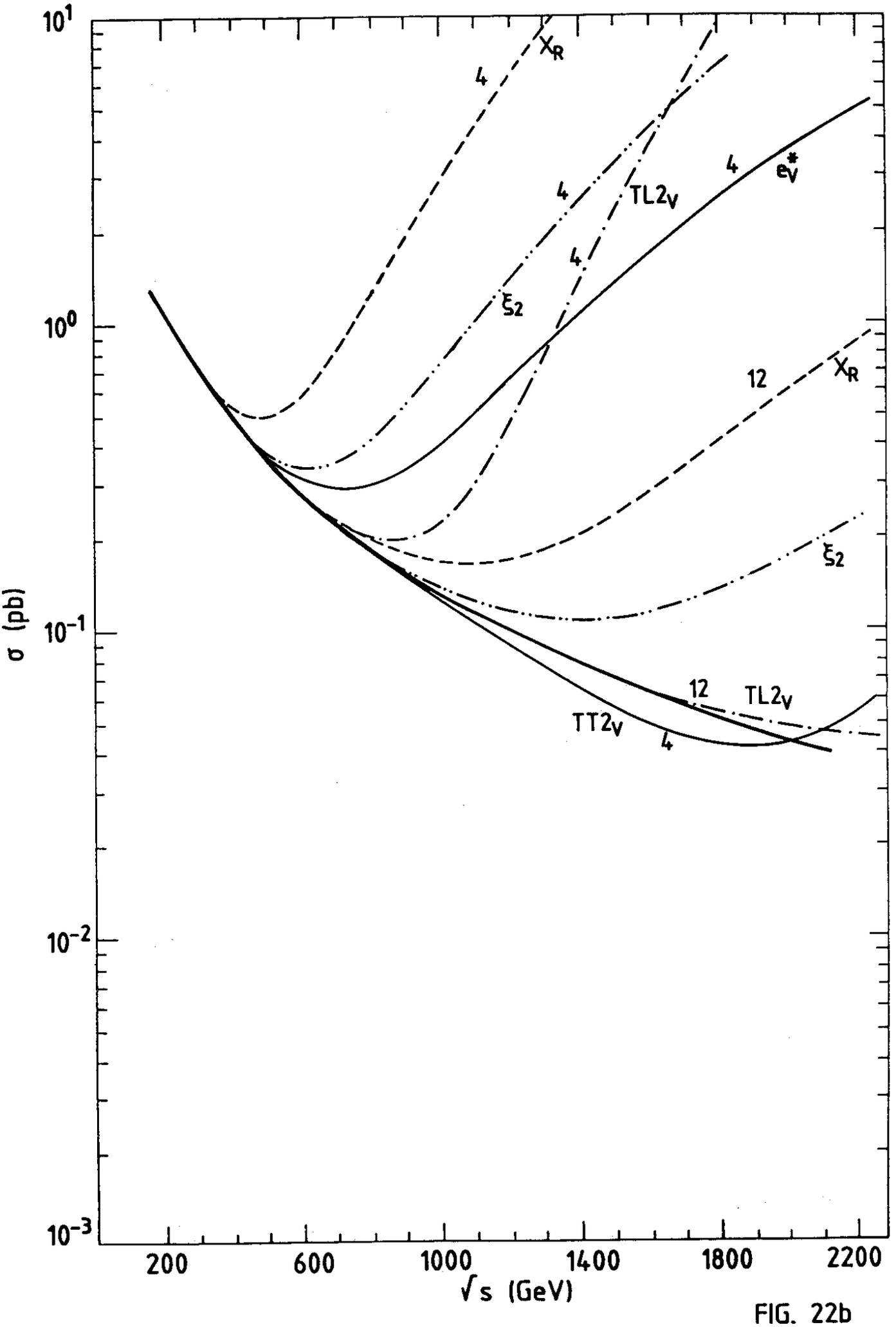
10^1
10^0
10^{-1}
10^{-2}
10^{-3}
σ (pb)
200
600
1000
1400
1800
2200
√s (GeV)
X_R
4
ξ_2
$TL2_\nu$
e^*_ν
12
$TT2_\nu$

FIG. 22b

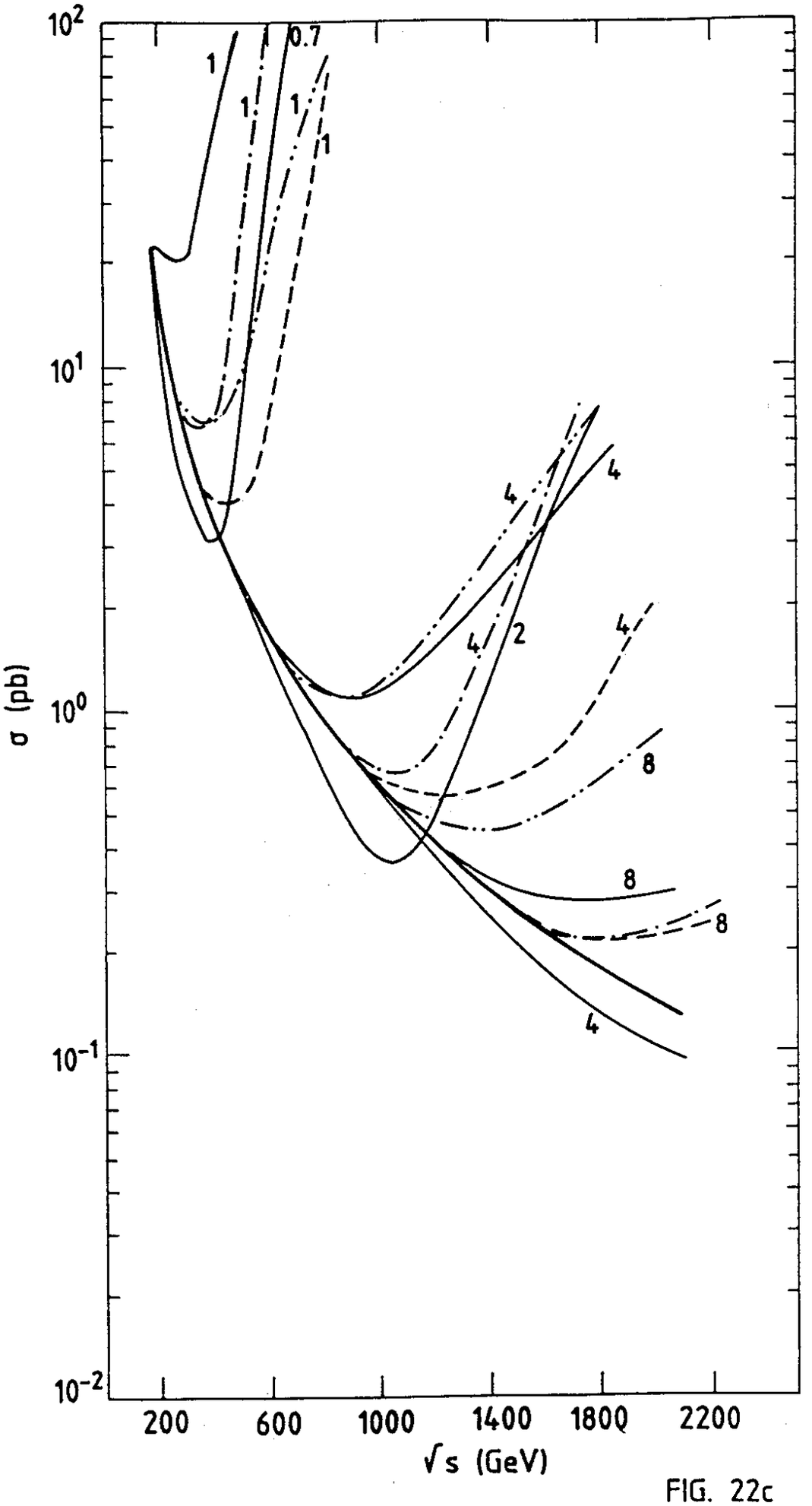
10^2
10^1
10^0
10^{-1}
10^{-2}
σ (pb)
200
600
1000
1400
1800
2200
√s (GeV)
0.7
1
1
1
1
4
4
4
2
4
8
8
8
4

FIG. 22c

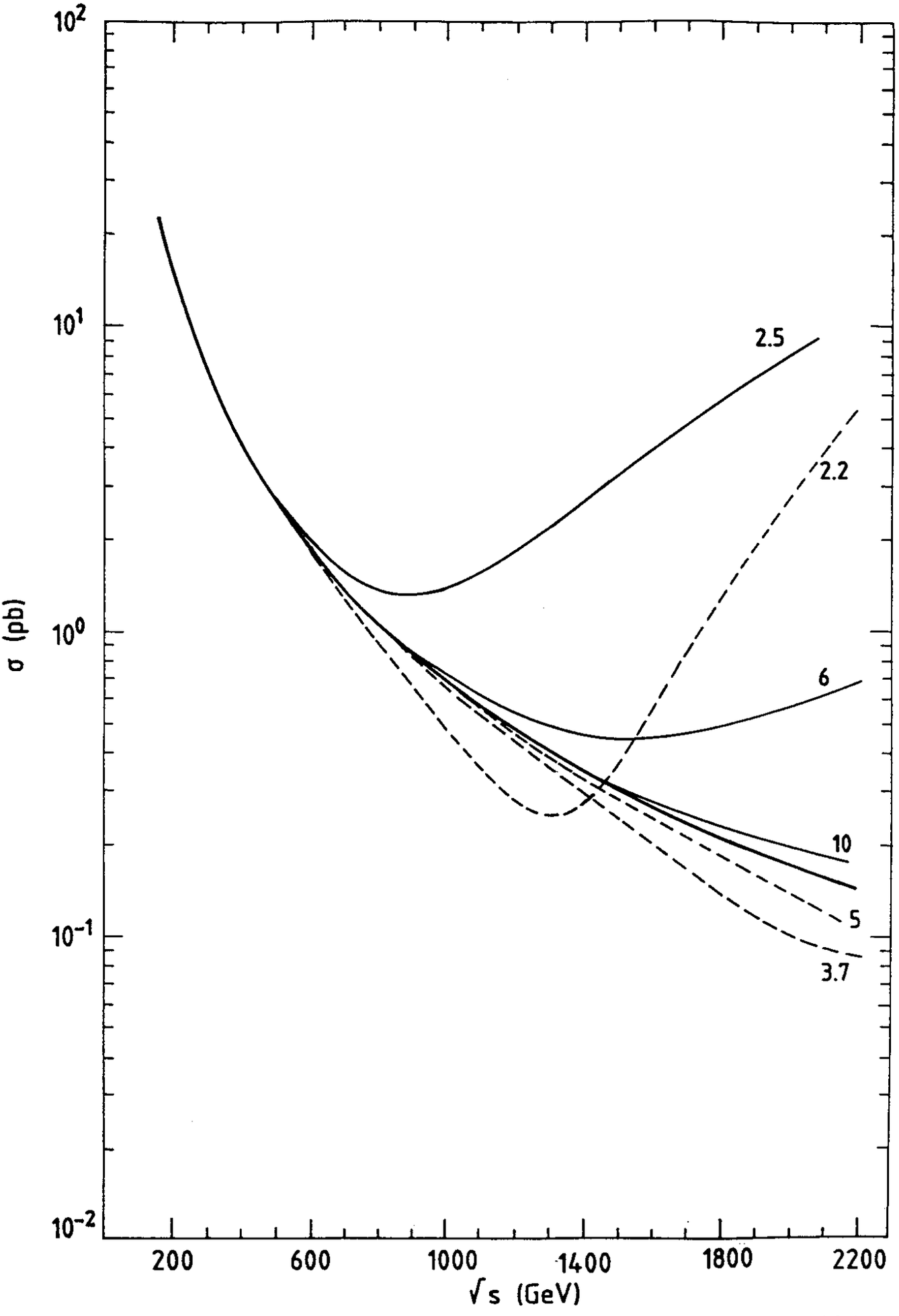
10^2
10^1
10^0
10^{-1}
10^{-2}
σ (pb)
2.5
2.2
6
10
5
3.7
200
600
1000
1400
1800
2200
√s (GeV)

FIG. 22d

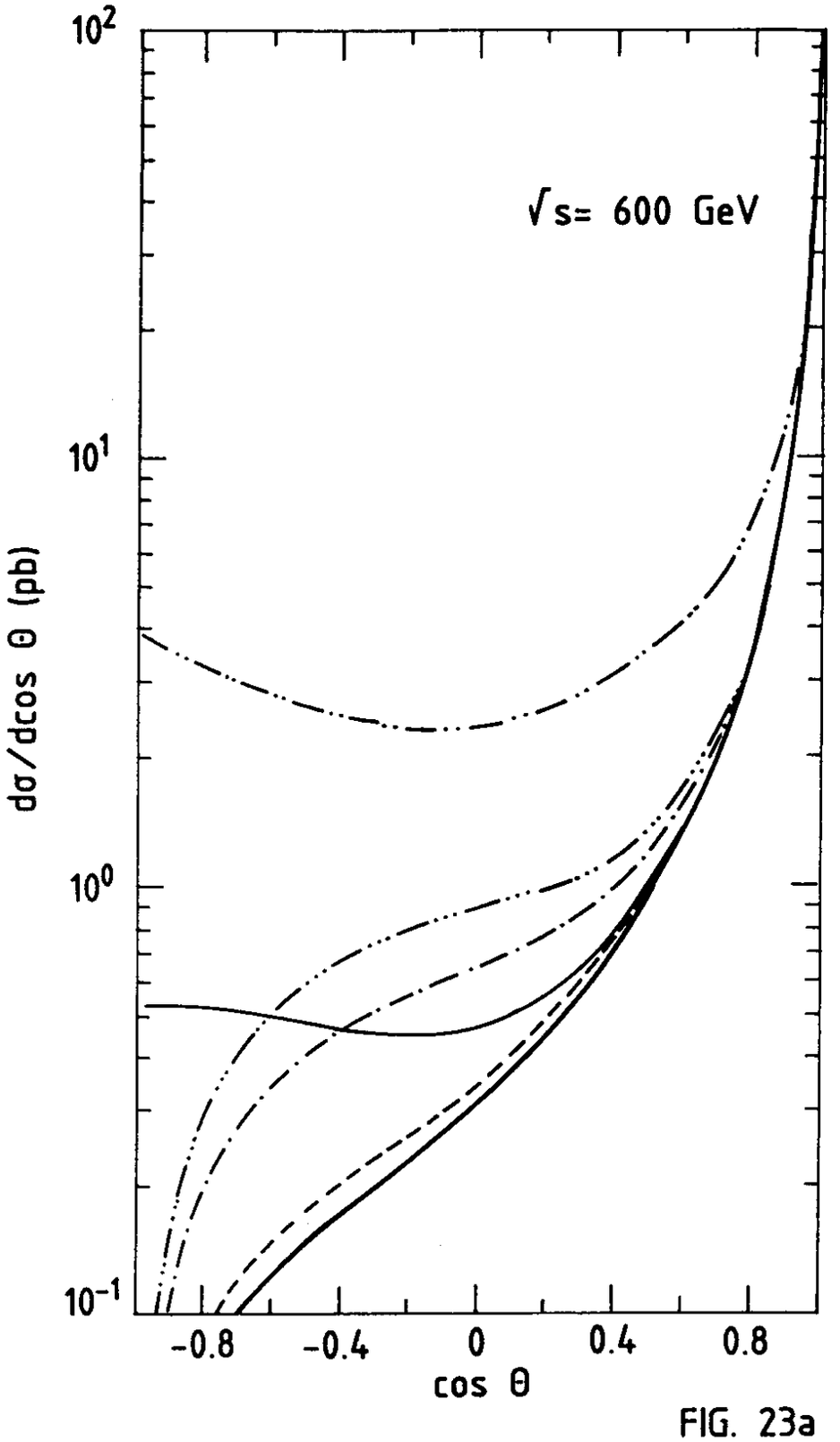

FIG. 23a

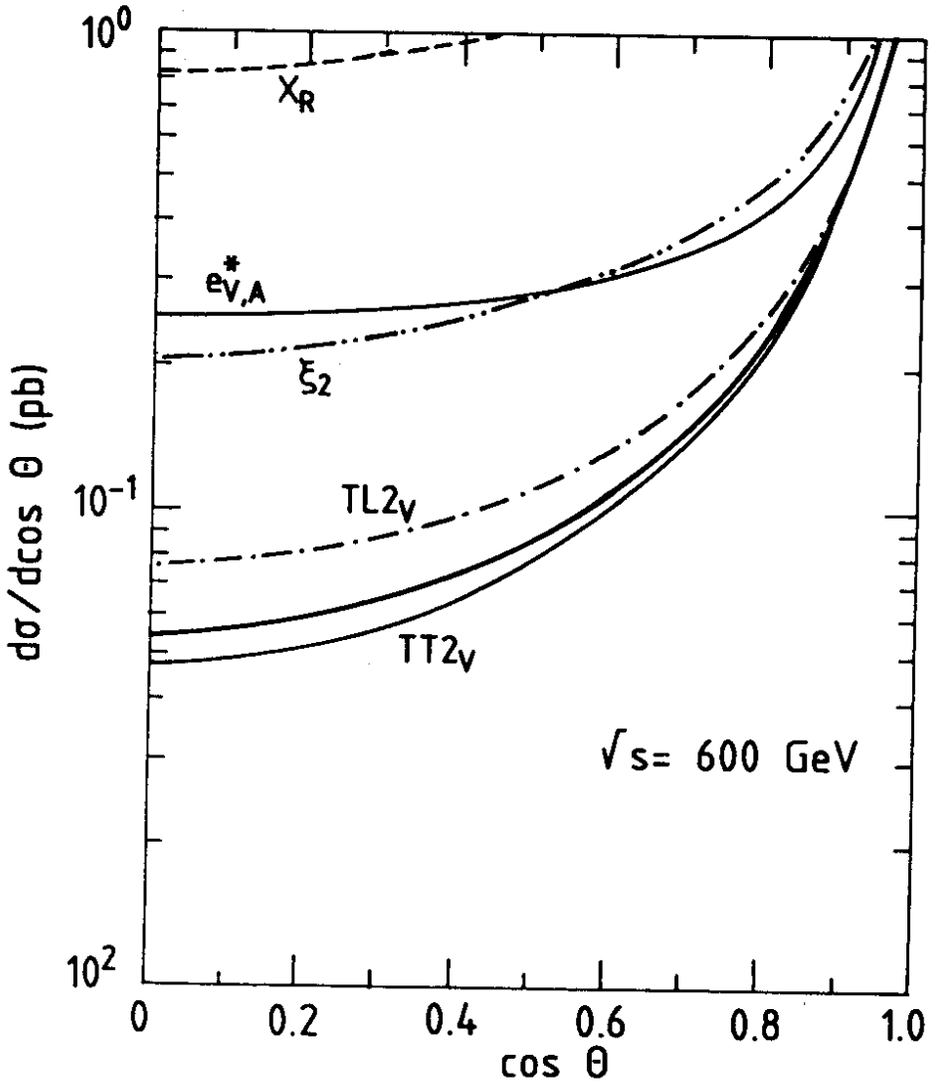
10^0
10^{-1}
10^2
X_R
$e^*_{V,A}$
ξ_2
$TL2_V$
$TT2_V$
$\sqrt{s}$= 600 GeV
$d\sigma/d\cos\theta$ (pb)
0
0.2
0.4
0.6
0.8
1.0
cos θ

FIG. 23b

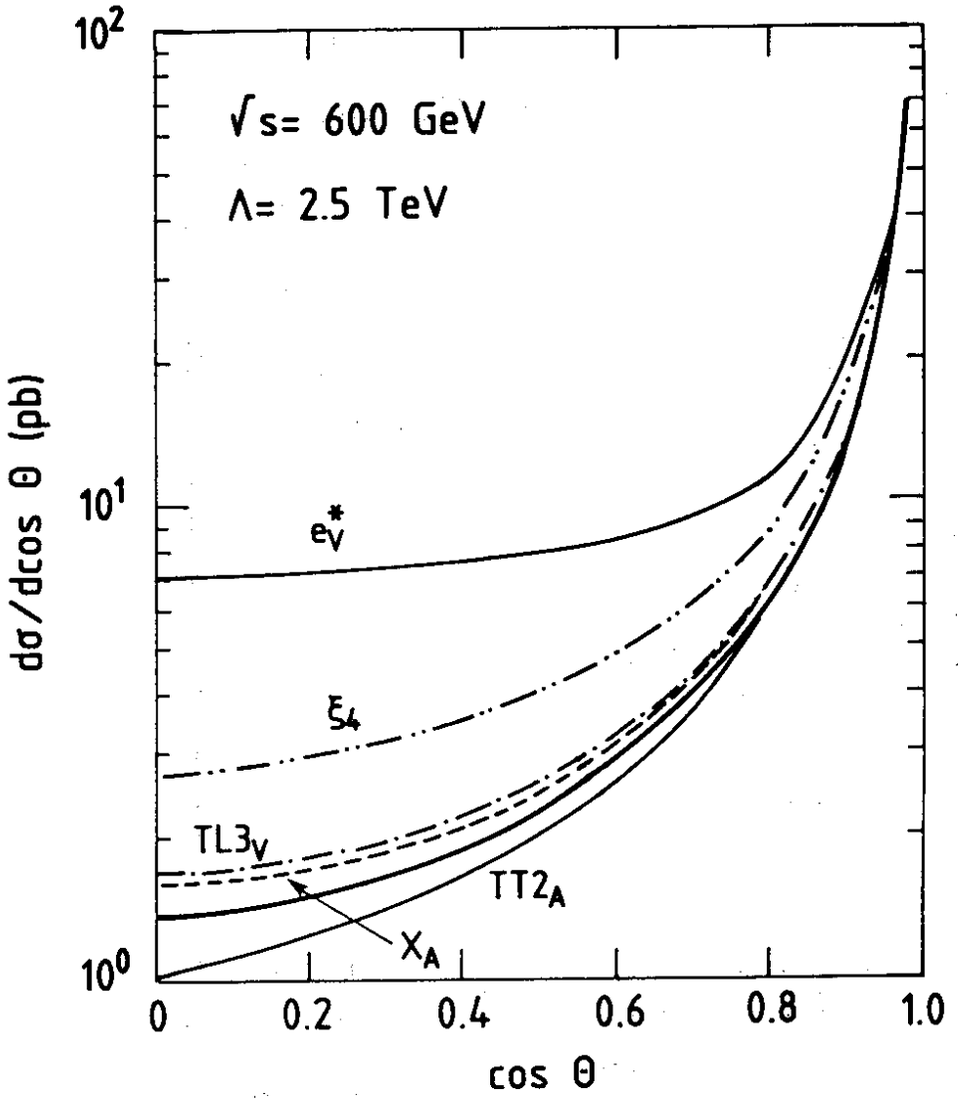
10^2
10^1
10^0
$\sqrt{s}$= 600 GeV
Λ= 2.5 TeV
e_V^*
ξ_4
$TL3_V$
$TT2_A$
X_A
0
0.2
0.4
0.6
0.8
1.0
cos θ
dσ/dcos θ (pb)

FIG. 23c

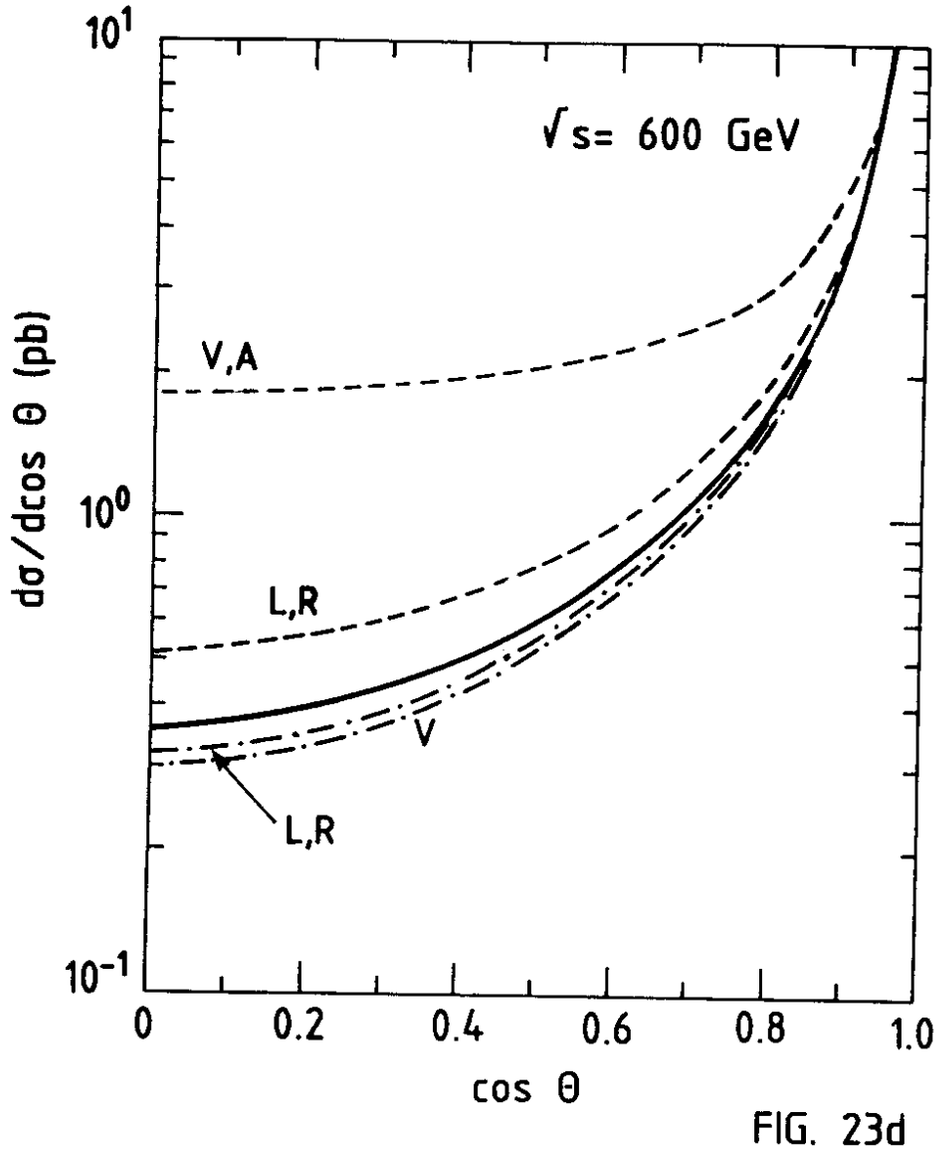
10^1
10^0
10^{-1}
$\sqrt{s}$= 600 GeV
V,A
L,R
V
L,R
dσ/dcos θ (pb)
0
0.2
0.4
0.6
0.8
1.0
cos θ

FIG. 23d

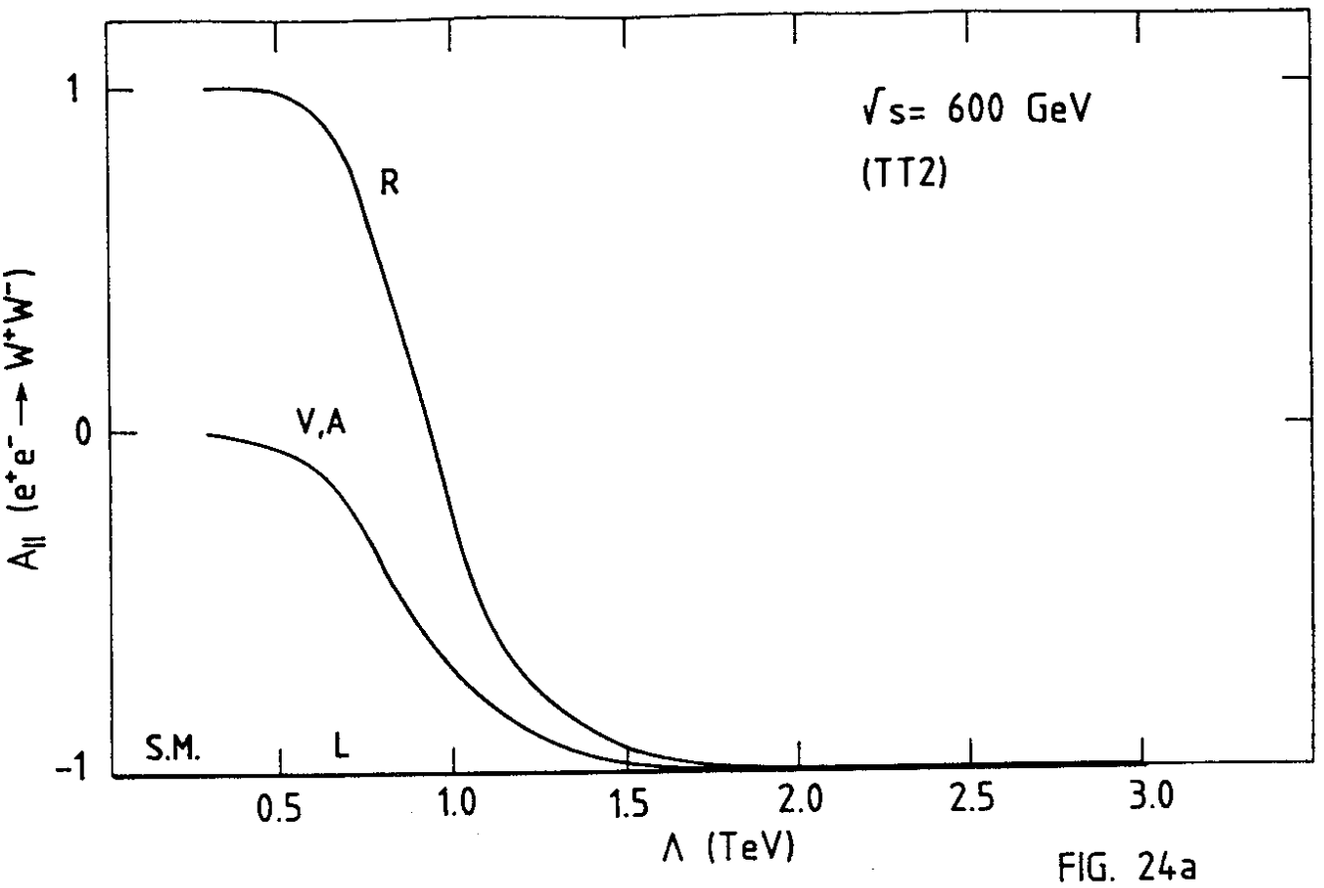

FIG. 24a

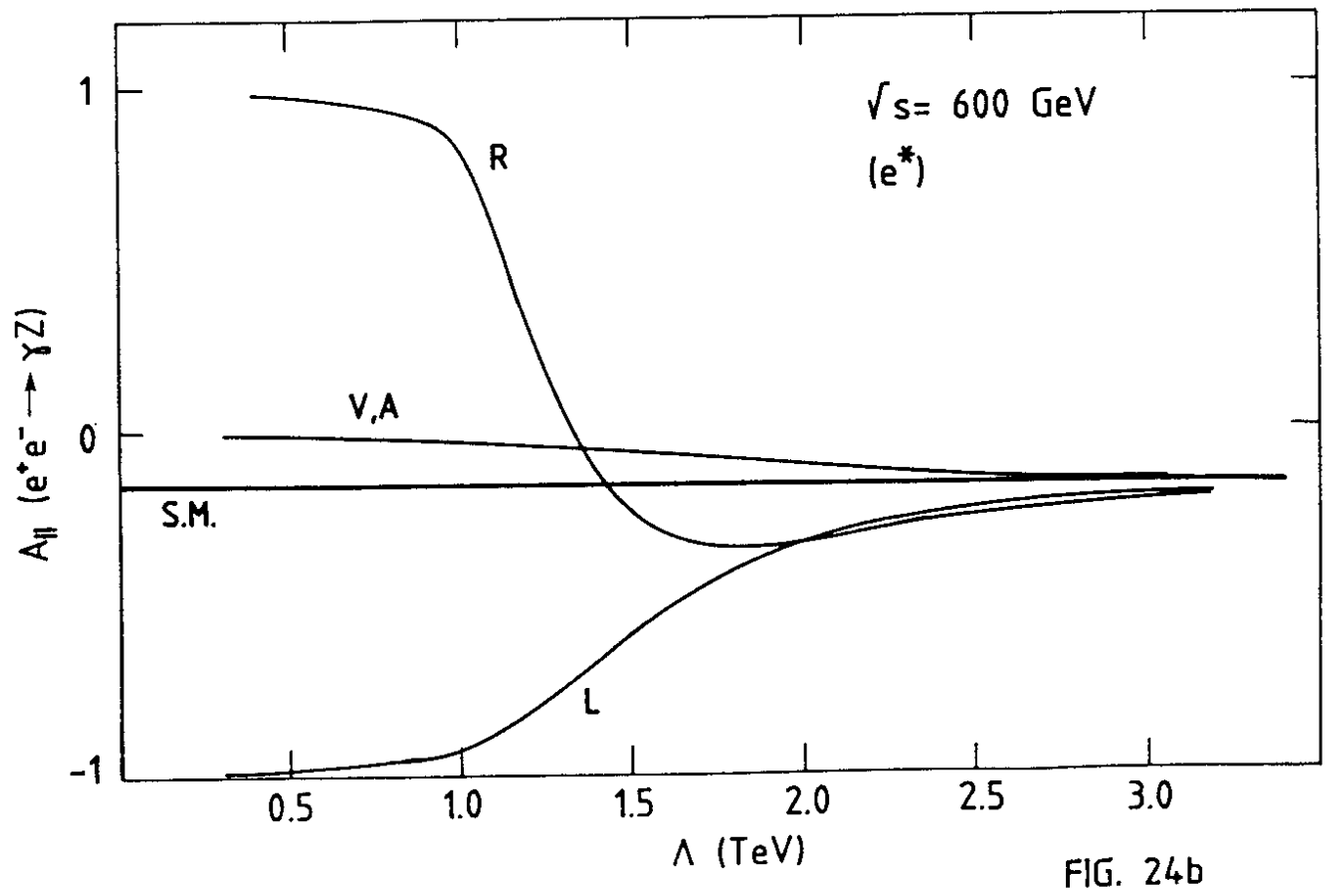

FIG. 24b